

# Modulated Pattern Formation: Stabilization, Complex-Order, and Symmetry

A Thesis  
Presented to  
The Academic Faculty

by

Jeffrey L. Rogers

In Partial Fulfillment  
of the Requirements for the Degree of  
Doctor of Philosophy in Physics

Georgia Institute of Technology  
April 2001

# Modulated Pattern Formation: Stabilization, Complex-Order, and Symmetry

Approved:

\_\_\_\_\_  
Dr. Michael Schatz, Chairman

\_\_\_\_\_  
Dr. Kurt Wiesenfeld

\_\_\_\_\_  
Dr. Ron Fox

\_\_\_\_\_  
Dr. Roman Grigoriev

\_\_\_\_\_  
Dr. Arnold Mandell

Date Approved April 9, 2001

# LIST OF SYMBOLS

Symbol	Description
$g$	gravitational acceleration ( $\frac{cm}{s^2}$ )
$T_1$	Temperature of the upper convection cell surface
$T_2$	Temperature of the lower convection cell surface
$\Delta T$	Temperature difference across the fluid layer ( $= T_2 - T_1$ )
$\bar{T}$	Mean plane fluid layer temperature [ $= (T_1 + T_2)/2$ ]
$P$	Pressure (bar)
$d$	Fluid layer depth (cm)
$\nu$	Kinematic viscosity
$\kappa$	Thermal diffusivity
$\alpha$	Thermal expansion coefficient
$Pr$	Prandtl number ( $= \nu/kappa$ )
$R$	Rayleigh number ( $= \alpha g \Delta T d^3 / \nu \kappa$ )
$\delta'$	Displacement amplitude (cm)
$\epsilon$	Dimensionless acceleration ( $= a/g$ )
$\delta Fr$	Dimensionless displacement amplitude ( $= \epsilon/\omega^2$ )
$\delta$ (App. A & B)	Abbreviation for $\delta Fr$ in dissertation
$\omega'$	Shaking frequency (Hz)
$\omega$	Dimensionless shaking frequency

Symbol	Description
$\tau_\nu$	Vertical thermal diffusion time - characteristic time scale
$q$	Dimensionless wave number
$q^H$	Dimensionless harmonic wave number
$q^S$	Dimensionless subharmonic wave number
$\wp$	Magnitude of power
$\wp^H$	Magnitude of over band of harmonic wave numbers
$\wp^S$	Magnitude of over band of subharmonic wave numbers
$\delta F r_{2c}$	Dimensionless displacement amplitude at the bicritical point
$R_{2c}$	Raleigh number at bicritical point
$\epsilon_2$	Reduced Rayleigh number in App. B [= $(R - R_{2c})/R_{2c}$ ]

# TABLE OF CONTENTS

LIST OF SYMBOLS	iii
LIST OF TABLES	viii
LIST OF FIGURES	ix
Acknowledgements	xxiii
<b>1 Introduction</b>	<b>1</b>
1.1 Spatially Extended Systems . . . . .	3
1.1.1 Rayleigh-Bénard Convection . . . . .	5
1.1.2 Taylor-Couette Flow . . . . .	8
1.1.3 Faraday Surface Waves . . . . .	10
1.2 Effects of Time Dependent Modulation . . . . .	13
1.3 Outline . . . . .	13
<b>2 Parametric Modulation</b>	<b>16</b>
2.1 Mechanical Analogy . . . . .	19
2.2 Modulated Hydrodynamics . . . . .	24
2.2.1 Rotation Modulated Taylor-Couette Flow . . . . .	27
2.2.2 Thermally Modulated Rayleigh-Bénard Convection . . . . .	29
2.2.3 Acceleration Modulated Rayleigh-Bénard Convection . . . . .	32

<b>3</b>	<b>Laboratory</b>	<b>39</b>
3.1	Convection Cell . . . . .	41
3.2	Vertical Oscillations . . . . .	45
3.3	Imaging Convection . . . . .	50
3.4	Computer Control . . . . .	54
	3.4.1 Temperature . . . . .	54
	3.4.2 Pressure . . . . .	60
3.5	Analysis . . . . .	62
3.6	Numerics . . . . .	69
	3.6.1 Conduction Marginal Stability . . . . .	69
	3.6.2 Pattern Simulations . . . . .	73
<b>4</b>	<b>Onset of Convection</b>	<b>75</b>
4.1	Onset Predictions . . . . .	77
4.2	Onset Measurements . . . . .	78
4.3	Harmonic Onset . . . . .	85
	4.3.1 Temporal Dependence . . . . .	85
	4.3.2 Harmonic Onset Patterns . . . . .	85
4.4	Subharmonic Onset . . . . .	89
	4.4.1 Temporal Dependence . . . . .	89
	4.4.2 Subharmonic Onset Patterns . . . . .	92
4.5	Discussion . . . . .	93
<b>5</b>	<b>Observations</b>	<b>95</b>
5.1	Observed Patterns . . . . .	97

5.1.1	Harmonic Patterns . . . . .	97
5.1.2	Subharmonic Patterns . . . . .	104
5.2	Direct Harmonic-Subharmonic Transition . . . . .	106
5.2.1	Transition Between Pure Harmonic and Coexistence Patterns	108
5.2.2	Transition Between Pure Subharmonics and Coexistence Patterns	113
5.3	Pattern Rotation . . . . .	117
5.4	Superlattices . . . . .	119
5.4.1	Observations Near Bicriticality . . . . .	121
5.4.2	Observations Away From Bicriticality . . . . .	125
5.4.3	Resonant Tetrads . . . . .	132
5.4.4	Other Frequencies . . . . .	137
5.5	Discussion . . . . .	140
<b>A</b>	<b>First Reprint</b>	<b>147</b>
<b>B</b>	<b>Second Reprint</b>	<b>158</b>
	<b>Vita</b>	<b>181</b>

# LIST OF TABLES

1	Table of inner ( $\Omega_1$ ) and outer ( $\Omega_2$ ) cylinder rotations considered by Carmi & Tustaniwskyj [1]. . . . .	28
---	---	----

# LIST OF FIGURES

1	Bifurcation diagram for classical Rayleigh-Bénard convection at onset in a non-Boussinesq fluid in terms of pattern amplitude $A$ as the stress parameter $R$ is varied. For increasing $R$ onset occurs at $R_c$ . Solid lines are stable solutions and dashed lines are unstable solutions. This diagram is appropriate for hexagons with downflowing centers (light). For the upflowing centers (dark) the hexagon bifurcation diagram would be reflected about $A = 0$ . . . . .	7
2	Twelve-fold symmetric quasicrystalline pattern in Faraday surface waves, reported by Gollub & Langer [2]. . . . .	11
3	A pendulum with a vertically oscillating base. . . . .	19
4	Phase space plots for an oscillator (a) without dissipation and (b) with dissipation. . . . .	21
5	Stability plots in terms of the nondimensional acceleration ( $\epsilon$ ) versus the oscillation frequency $\omega$ for (a) a hanging pendulum and (b) an inverted pendulum. . . . .	23

6	Sketch of stripes in a fluid layer driven out of equilibrium by both an imposed temperature difference and parametric oscillations. Temperature difference is defined in terms of the uniform top plate temperature $T_1$ and uniform bottom plate temperature $T_2$ ( $T_2 > T_1$ ) by $\Delta T = T_2 - T_1$ . Periodic oscillations are defined by a dimensionless acceleration $\epsilon$ and a dimensionless angular frequency $\omega$ through the driving $\epsilon \cos \omega t$ . The fluid layer depth is given by $d$ . Shaded lines represent stripes that would be observed when viewing a parallel roll state by a shadowgraph from above. . . . .	33
7	Overview of the experimental configuration. . . . .	40
8	Schematic of the compressed gas convection cell. . . . .	42
9	Aluminum mirror that acts as the bottom surface of the convection cell (see SIDE view). . . . .	43
10	Dimensions of the pressure vessel top retaining plate. Upper surface of the sapphire crystal is slanted and must be aligned to seat into the top plate. . . . .	44
11	Sketch of the first mechanical shaking device. . . . .	46
12	First shaker mounting bracket connecting the convection cell to the driving rod. View from the side (a) and from above (b). . . . .	47
13	Sketch of the second mechanical shaking device. This shaker has improved dynamical range over the first configuration and employs a rectangular slide on the driving rod to eliminate driving rod rotations and reduce lateral vibrations. . . . .	48

14	Second shaker mounting bracket connecting the driving rod to the rectangular slide and the swivel bearing used. . . . .	49
15	Alignment table for the square air-bearing which is attached to the alignment plate by angle brackets and suspended by springs. The springs act as vibration damping. . . . .	51
16	Schematic of the shadowgraph configuration. The collimator lens has a focal length $f$ . The camera lens is focused on the imaging plane, a distance $\Delta z$ further from camera than the focal plane. Shades in the presented experimental images could be reversed by changing the imaging plane to a distance $-\Delta z$ ; closer to the camera than the focal plane. . . . .	53
17	Overview of the temperature control system which controls both $\Delta T$ and $\bar{T}$ using linear PID algorithms. . . . .	55
18	Circuit used in computer control of the bottom plate temperature. It accepts input from two computer channels (DAC0 and DAC1), scales the applied voltage to a fine and a coarse scale resulting in much higher resolution than would be achievable with a single channel. Maximum output voltage is 10 V with a resolution of 0.00239 mV. . . . .	57

19	Circuit diagram for the programmable circuit used in controlling the water bath temperature. The boxed numbers are the pin placements for associated connections. Input voltage is supplied by the 5 Volt reference chip. Circuit output voltage ranges from 150 mV to 300 mV depending on the gain present from the operational amplifier. Gain is computer controlled by digitally programming values into two variable resistors providing resolution of 0.5859 mV over the voltage range. . . . .	59
20	Schematic of the CO <sub>2</sub> supply and pressure control system. Pressurized 99.99 % pure CO <sub>2</sub> is supplied by a tank at 830 PSI. Cell pressure is measured by a SensorTec sensor and fine pressure control is provided by regulating heat supplied to a downstream gas ballast. . . . .	61
21	Computer generated patterns $u(x, y) = \cos qx$ (a) and $u(x, y) = \cos 2.9qy$ (b) are summed to produce a pattern (c) composed of wave numbers typical of experimental images. All these patterns are 480 by 480 pixels with a circular mask applied to (c) to simulate the experimental lateral boundaries. . . . .	64
22	Power spectrum for the computer generated pattern in Fig. 21(c). (a) Two-dimensional spatial power spectrum can be represented in terms of (b) the radial power [ $\rho(q)$ ] and angular power populations (c & d). Angular power is computed over wave number bands. . . . .	66
23	Results from a marginal stability analysis of the Boussinesq equations [Eqs. (13)] linearized about the conduction state for $Pr = 0.93$ and $\omega = 50$ (a & b) as well as $\omega = 100$ (c & d). . . . .	76

24	Parallel stripes observed near onset ( $Pr = 0.943$ , $R = 1760$ ) in the absence on shaking ( $\omega = 0$ ). . . . .	79
25	Comparison of conduction stability predictions with laboratory observations made at $\omega = 98.0$ for (a) $R_c$ and (b) $q_c$ . Harmonic measurements are denoted by $\square$ while $\triangle$ marks measurements at subharmonic onset. . . . .	80
26	Images from an automated experimental run to determine stability boundaries and the corresponding $\wp(q)$ for each image. Parameters are $\omega = 99.4$ for all points and (a) $\delta Fr = 4.06 \times 10^{-4}$ & $R = 4280$ , (b) $\delta Fr = 3.99 \times 10^{-4}$ & $R = 4260$ , (c) $\delta Fr = 4.91 \times 10^{-4}$ & $R = 4260$ , and (d) $\delta Fr = 4.29 \times 10^{-4}$ & $R = 4220$ . . . . .	81
27	Temporal dependence of Fourier modes ( <i>simulation</i> ) in the fluid layer mid plane during simulations of (a) purely harmonic convection and (b) purely subharmonic convection. . . . .	84
28	Shadowgraph ( <i>experiment</i> ) displaying harmonic temporal resonance, periodicity at $\tau$ . At $t = 0$ (a) the stripe state is well defined. For odd multiples of $\tau$ (b & d) the stripe state becomes broader, while at even multiples of $\tau$ the original state repeats (c). Each 128 by 128 pixel frame is over the same spatial location separated in time by $\tau/2$ . . . .	86
29	Harmonic onset striped patterns include: (a) parallel stripes ( $\delta Fr = 3.34 \times 10^{-4}$ , $\omega = 97.8$ & $R = 3002$ ), (b) targets ( $\delta Fr = 3.29 \times 10^{-4}$ , $\omega = 98.0$ & $R = 2979$ ), (c) stripes with hexagons ( $\delta Fr = 3.71 \times 10^{-4}$ , $\omega = 96.2$ & $R = 4388$ ), and (d) targets with hexagons ( $\delta Fr = 3.76 \times 10^{-4}$ , $\omega = 96.6$ & $R = 4107$ ). . . . .	87

30 Close up of a convex disclination confirming subharmonic temporal dependence. Note, the + signs near the image centers, these are plotted at the same coordinates in both frames. The disclinations center stripe is light at even multiples of  $\tau$  [(a)  $t=0$ ] and dark at odd multiples of  $\tau$  [(b)  $t = 35\tau$ ]. Shown are the same spatial locations of 128 by 128 pixel images with the + signs at the same pixel values. . . . . 90

31 Examples of patterns observed near onset of subharmonic convection. Patch (a) of parallel stripes ( $\delta Fr = 4.02 \times 10^{-4}$ ,  $\omega = 97.9$  &  $R = 4395$ ), (b) parallel stripes with five dislocations ( $\delta Fr = 3.74 \times 10^{-4}$ ,  $\omega = 97.9$  &  $R = 4857$ ), (c) stripes with a giant convex disclination and several dislocations ( $\delta Fr = 3.34 \times 10^{-4}$ ,  $\omega = 97.5$  &  $R = 4811$ ), and (d) onset spiral ( $\delta Fr = 4.12 \times 10^{-4}$ ,  $\omega = 97.9$  &  $R = 4173$ ). . . . . 91

32 Parameter space showing conduction marginal stability curves for harmonic (solid) and subharmonic (dashed) convection as well as experimentally determined regions of behavior. Experimental measurements of the transverse modulated (see text) subharmonic stripes (+) are fitted with a dotted line to help guide the eye. . . . . 98

33 Examples of typical patterns observed moving away from onset stripes: (a) stripes with defects and two wall foci forming ( $\delta Fr = 3.47 \times 10^{-4}$ ,  $\omega = 98.4$ , &  $R = 3820$ ), (b) three foci stripes ( $\delta Fr = 3.36 \times 10^{-4}$ ,  $\omega = 98.4$ , &  $R = 3830$ ), (c) spiral defect chaos ( $\delta Fr = 2.06 \times 10^{-4}$ ,  $\omega = 96.2$ , &  $R = 4290$ ), and (d) far from onset cellular patterns ( $\delta Fr = 2.70 \times 10^{-4}$ ,  $\omega = 100.3$ , &  $R = 7920$ .) . . . . . 99

- 34 Examples of dislocation pairs due to skew-varicose instabilities mediating oscillations between targets and one-arm spirals. Images are separated in time (in seconds) at the same parameters ( $\delta Fr = 1.74 \times 10^{-4}$ ,  $\omega = 98.4$ , &  $R = 2480$ ): (a)  $t = 0$ , (b)  $t = 10$ , (c)  $t = 30$ , (d)  $t = 40$ , (e)  $t = 45$ , & (d)  $t = 60$ . . . . . 102
- 35 Examples of typical patterns observed moving away from onset target: (a) one arm spiral ( $\delta Fr = 1.74 \times 10^{-4}$ ,  $\omega = 98.4$ , &  $R = 2480$ ), (b) multi-arm spiral ( $\delta Fr = 1.95 \times 10^{-4}$ ,  $\omega = 99.4$ , &  $R = 2420$ ), (c) off-center multi-arm spiral ( $\delta Fr = 2.26 \times 10^{-4}$ ,  $\omega = 99.0$ , &  $R = 2940$ ), and (d) spiral defect chaos ( $\delta Fr = 2.30 \times 10^{-4}$ ,  $\omega = 98.5$ , &  $R = 3660$ .) 103
- 36 Examples of typical subharmonic patterns observed away from onset: (a) two foci stripes with defects ( $\delta Fr = 4.17 \times 10^{-4}$ ,  $\omega = 98.1$ , &  $R = 4888$ ), (b) three foci transverse modulated stripes ( $\delta Fr = 4.01 \times 10^{-4}$ ,  $\omega = 98.0$ , &  $R = 6552$ ), radial stripes - onset of subharmonic disorder ( $\delta Fr = 4.83 \times 10^{-4}$ ,  $\omega = 95.0$ , &  $R = 6120$ ), and (d) subharmonic disorder ( $\delta Fr = 4.60 \times 10^{-4}$ ,  $\omega = 95.0$ , &  $R = 7670$ .) . . . . . 105
- 37 Phase plane comparing the experimentally measured coexistence onset to the marginal stability curves for conduction. Boundary between coexistent and purely harmonic flows ( $\diamond$ ) follows the marginal subharmonic ( $\omega/2$ ) curve (dashed line), while the boundary between coexistent and purely subharmonic patterns ( $\circ$ ) tracks the marginal harmonic ( $\omega$ ) curve as far as the boundary can be reliably determined. Filled in triangles are the locations of patterns in Figs. 38 & 42. . . . 107

38 Patterns (*experiments*) on either side of the purely harmonic-coexistence boundary. Pure harmonic stripes (a) with defects ( $\delta Fr = 3.31 \times 10^{-4}$ ,  $\omega = 98.0$ , &  $R = 6280$ ). Coexistence state (b) with 3-foci harmonic stripes and subharmonic stripe patches ( $\delta Fr = 3.54 \times 10^{-4}$ ,  $\omega = 98.0$ , &  $R = 6280$ ). . . . . 108

39 Patterns (*simulations*) on either side pure harmonic-coexistence boundary displaying (a) multiple side-wall singularities ( $\delta Fr = 3.28 \times 10^{-4}$ ,  $\omega = 98.0$ , &  $R = 6600$ ) and (b) the same kind of localized subharmonic patches as observed in the experiments [Fig. 38(b)]. . . . . 109

40 Azimuthally averaged power spectra for six different experimental conditions from the transition between pure harmonic convection and pure subharmonic convection, passing through a region of coexisting harmonic-subharmonic convection. Representative images from each data point are shown in other figures: (a) in Fig. 38(a), (b) in Fig. 38(b), (c) in Fig. 42(a), (d) in Fig. 42(b), (e) in Fig. 42(c), and (f) in Fig. 42(d). . . . . 111

- 41 Spatial spectral analysis of the transition from pure harmonic convection to pure subharmonic convection, passing through a region of coexisting harmonic-subharmonic convection with increasing  $\delta Fr$  at  $R = 6280 \pm 10$ . The azimuthally averaged spectra for both the harmonic and subharmonic modes are characterized by (a) the spectral power in each mode  $\varphi^H$  &  $\varphi^S$ , (b) the mode wave numbers  $q^H$  &  $q^S$ , (c) the widths of the spectral peaks  $\sigma^H$  &  $\sigma^S$ , and (d) the wavenumber ratio  $\frac{q^H}{q^S}$ . Throughout,  $\circ$  indicates harmonic pattern component and  $\triangle$  the subharmonic pattern component. Filled in symbols correspond to patterns shown in Figs. 38 & 42. . . . . 112
- 42 Patterns (*experiments*) on either side of the harmonic-coexistence marginal stability curve ( $Pr = 0.930, \omega = 98.0$ ) for  $R = 4982$  [ $\delta Fr = 3.80 \times 10^{-4}$  (a) &  $\delta Fr = 3.69 \times 10^{-4}$ (b)] and  $R = 6275$  [ $\delta Fr = 3.93 \times 10^{-4}$ (c) &  $\delta Fr = 3.77 \times 10^{-4}$  (d)]. . . . . 114
- 43 Patterns (*simulations*) on either side pure subharmonic-coexistence boundary displaying (a) transverse modulated subharmonic stripes & cross-rolls ( $\delta Fr = 4.373 \times 10^{-4}, \omega = 98, \& R = 6800$ ) and (b) a similar state broken into domains ( $\delta Fr = 3.957 \times 10^{-4}, \omega = 98, \& R = 6800$ ). 115
- 44 Rotating subharmonic stripes (*experiments*) with a long wave length distortion. Stripes in (a) rotate clockwise ( $\delta Fr = 3.99 \times 10^{-4}, \omega = 97.7, \& R = 5195$ ), while the stripes in (b) rotate counter-clockwise ( $\delta Fr = 3.98 \times 10^{-4}, \omega = 98.0, \& R = 5317$ ). . . . . 119

45	Square superlattices observed in experiments (a) and in numerical simulations (b); both at $Pr = 0.930$ . In (a) $\delta Fr = 3.88 \times 10^{-4}$ , $\omega = 95.3$ , & $R = 7028$ , while in (b) $\delta Fr = 3.75 \times 10^{-4}$ , $\omega = 98$ , & $R = 4750$ . . .	120
46	Patterns observed passing from conduction by slowly increasing $R$ at $\delta Fr \lesssim \delta Fr_{2c}$ . Corresponding parameters are: (a) $\delta Fr = 3.89 \times 10^{-4}$ , $\omega = 95.0$ , & $R = 4780$ , (b) $\delta Fr = 3.88 \times 10^{-4}$ , $\omega = 95.1$ , & $R = 4910$ , (c) $\delta Fr = 3.88 \times 10^{-4}$ , $\omega = 95.0$ , & $R = 5390$ , and (d) $\delta Fr = 3.73 \times 10^{-4}$ , $\omega = 96.7$ , & $R = 6270$ . . . . .	122
47	Phase planes mapped (a) experimentally and by (b) Boussinesq numerics. The dotted region in (a) is the parameter range shown in (b). Experimentally determined square superlattice (■) and mixed harmonic cellular symmetry patterns (●) boundaries are shown in (a). Locations of square superlattices (□) and stripe superlattices (△) in Boussinesq numerics are shown in (b). Square superlattice boundaries from non-Boussinesq experiments are compared (a) with boundaries found in Boussinesq numerics at $R \approx 6300$ . . . . .	125
48	Numerical solutions find stripe superlattices ( $\delta Fr = 3.732 \times 10^{-4}$ , $\omega = 98$ , & $R = 4794$ ) near the bicritical point. . . . .	126
49	Coexistence patterns close to bicriticality display hexagons in the harmonic component due to non-Boussinesq effects in both (a) experiments ( $\delta Fr = 3.64 \times 10^{-4}$ , $\omega = 98.1$ , & $R = 4983$ ) and (b) numerics ( $\delta Fr = 3.75 \times 10^{-4}$ , $\omega = 98$ , & $R = 4750$ ) . . . . .	127
50	Temperature field (grayscale) and planar velocity field (arrows) in a square superlattice mid plane at $\omega = 98$ observed in simulations. . . .	130

51	Temperature field (grayscale) and vertical velocity field (arrows) component corresponding to the planar field shown in Fig. 50. . . . .	131
52	Power spectra for (a) the square superlattice in Fig. 45(a) ( <i>experiment</i> ) and (b) the stripe superlattice shown in Fig. 48 ( <i>simulation</i> ). . . . .	133
53	The temporal variation of linear eigenvectors multiplied with adjusted amplitude factors $A = 0.0382$ , $B = 0.0108$ (see text) at $\delta Fr = 3.732 \times 10^{-4}$ , $R = 4790$ for the harmonic (upper curve) and subharmonic (lower curve) modes, respectively. Comparison is made with the numerical amplitudes of the Fourier modes at $\mathbf{q}_1^H$ (+) and $\mathbf{q}_1^S$ ( $\diamond$ ), respectively, for the square superlattice mid plane temperature field $T(\mathbf{x}, t)$ in units of $\Delta T$ . . . . .	135
54	Superlattices ( <i>numerical</i> ) in the vicinity of the bicritical points at other $\omega$ values: (a) $\omega = 50$ and (b) $\omega = 300$ . . . . .	137
55	Superlattice ( <i>experiment</i> ) at $\omega = 50$ (a) and its power spectrum (b). . . . .	139
56	Patterns ( <i>experiment</i> ) at $Pr = 0.928$ , $R = 5180$ , $\omega = 50.4$ of (a) purely harmonic spiral defect chaos ( $\delta Fr = 8.08 \times 10^{-4}$ ) and (b) purely subharmonic stripes with transverse modulation ( $\delta Fr = 9.27 \times 10^{-4}$ ). . . . .	140

- 57 Convection patterns visualized using shadowgraphy and characterized by four dimensionless quantities: Prandtl number  $Pr = \frac{\nu}{\kappa} = 0.93$ , driving frequency  $\omega = \frac{d^2}{\kappa} 2\pi f = 98$ , displacement amplitude  $\delta = \frac{\kappa^2}{gd^4} \delta'$  and Rayleigh number  $R = \frac{\alpha g d^3 \Delta T}{\nu \kappa}$ , with the kinematic viscosity  $\nu$ , thermal diffusivity  $\kappa$ , thermal expansion coefficient  $\alpha$ , forcing frequency  $f$  (Hz), amplitude  $\delta'$  (cm) and gravitational acceleration  $g = 980 (\frac{cm}{s^2})$ . (a) H spiral defect chaos ( $\delta = 1.76 \times 10^{-4}$ ,  $R = 3198$ ). (b) coexisting H rolls and hexagons ( $\delta = 3.74 \times 10^{-4}$ ,  $R = 4216$ ). (c) S rolls near onset ( $\delta = 4.26 \times 10^{-4}$ ,  $R = 3958$ ). (d) S rolls ( $\delta = 4.05 \times 10^{-4}$ ,  $R = 4990$ ). (e) H rolls with localized domains of S rolls ( $\delta = 3.76 \times 10^{-4}$ ,  $R = 4962$ ). (f) S rolls containing grain boundaries overlaying a weak pattern of H rolls and cells ( $\delta = 3.64 \times 10^{-4}$ ,  $R = 5424$ ). . . . . 149
- 58 Phase diagram and comparison of linear stability predictions to experiments at  $\omega = 98$ . The phase diagram (a) contains regions of conduction, convection with H ( $\omega$ ) and S ( $\omega/2$ ) modulations as well as coexisting H-S patterns. Marginal stability curves computed for the conduction state subjected to H (solid line) and S (dashed) perturbations agree with the measured values of  $R_c$  (a) and  $g_c$  (b) at the onset of H ( $\square$ ) and S ( $\triangle$ ) convection. The measured transition to coexisting patterns from pure H ( $\diamond$ ) and S ( $\circ$ ) states is compared to the marginal stability predictions for *conduction*. The maximum displacement ( $\delta = 5 \times 10^{-4}$ ) corresponds to an acceleration of  $\sim 5g$ . . . . . 151

59	<p>H (<math>\square</math>) and S (<math>\triangle</math>) patterns rotate in opposite directions. (a) At <math>\delta = 3.47 \times 10^{-4}</math> the motion of a single H roll (dashed line) is followed in time at intervals of <math>11.3 \tau_v</math>. (b) At <math>\delta = 4.53 \times 10^{-4}</math> the motion of a S disclination (bright white region) is followed in time at intervals of <math>15.0 \tau_v</math>. (c) The dimensionless rotation rate versus <math>\delta</math> for <math>R = 3920</math> and <math>\omega = 98</math>. . . . .</p>	153
60	<p>Coexisting H and S patterns (a) (<math>\delta = 3.62 \times 10^{-4}</math>, <math>\omega = 108</math> and <math>R = 5515</math>) may be decomposed by filtering in the wavenumber domain (b) to yield both H (c) and S (d) components; in this case, both components equal power to the wavenumber spectrum (b) and exhibit mode-locking of the wave numbers (<math>\frac{q_S}{q_H} = \frac{5.02}{1.67} = 3.01</math>). (e) The relative power contributed by H (<math>\square</math>) and S (<math>\triangle</math>) components to wavenumber spectra changes abruptly as a function of <math>\delta</math> for constant <math>\omega = 98</math> and <math>R = 5320</math>. Vertical lines mark the measured coexistence boundaries. . . . .</p>	155
61	<p>Experimental square superlattice (SQS) at <math>\delta = 3.58 \times 10^{-4}</math> and <math>\epsilon_2 = 0.650</math>. These states display complex periodic spatial structure (a) and power spectra (b) typically dominated by twelve peaks with <math> \mathbf{q}_i^H  \approx 0.95 q_{2c}^H</math> and <math> \mathbf{q}_i^S  \approx 0.86 q_{2c}^S</math> for these parameter values. . . . .</p>	162

62	Phase-plane showing the SQS stability boundaries as well as the codimension-two point at the intersection of the H (solid) and S (dashed) linear stability curves. Experimentally observed SQS boundary ( $\square$ ) is reproduced in numerical solutions ( $\blacksquare$ ) at $\epsilon_2 \approx 0.4$ . Experimental patterns in the $\circ$ bounded region display square, rhombic and hexagonal symmetry in the H sublattice. Numerical results indicate SQS are the result of a supercritical primary bifurcation at the bicritical point ( $\blacksquare$ inset). Simulations also find roll superlattices ( $\blacktriangle$ inset), over a narrow parameter range, which bifurcate supercritically from H rolls. . . . .	164
63	Superlattices observed in numerics near the bicritical point: (a) SQS at $\delta = \delta_{2c}$ and $\epsilon_2 = 0.053$ , (b) roll superlattice at $\delta = 3.732 \times 10^{-4}$ and $\epsilon_2 = 0.053$ . . . . .	165
64	The temporal variation of linear eigenvectors multiplied with adjusted amplitude factors $A = 0.0382$ , $B = 0.0108$ (see text) at $\delta = 3.732 \times 10^{-4}$ , $\epsilon_2 = 0.053$ for the H (upper curve) and S (lower curve) modes, respectively. Comparison is made with the numerical amplitudes of the Fourier modes at $\mathbf{q}_1^H$ (+) and $\mathbf{q}_1^S$ ( $\diamond$ ), respectively, for the SQS midplane temperature field $T(\mathbf{x}, t)$ in units of $\Delta T$ . . . . .	166

# Acknowledgements

A large number of individuals have contributed to the research described in this dissertation and it is my pleasure to acknowledge their assistance. Sometimes selecting an interesting project is one of the most difficult research tasks and in this case Michael Schatz was responsible for designing the original experimental device. Additionally, as a collaborator Michael supplied an endless stream of experimental suggestions and refinements as well as remained involved in the day-to-day workings in the laboratory. In his role as an advisor I am grateful to him for assistance in interpreting results, consistent financial support as well as his exceptionally careful review of manuscripts and suggestions for the refinement of those papers. Jon Bougie and Jack Swift contributed linear stability calculations and discussions to the initial results. Guenter Ahlers was kind enough to supply the computer codes to calculate the properties of the working fluid ( $\text{CO}_2$  gas) and invite me to UCSB to speak. During that brief visit I had the opportunity to meet Werner Pesch. Upon returning to Germany, Werner and his student Oliver Brausch became involved in the project by performing a large number of difficult numerical simulations which augmented the experimental findings. The collaboration with Werner and Oliver was a very fruitful one and I would like to thank them both for all their hard work and constant discussions. Andrew Lee at University of Texas – Austin helped in the construction of the second mechanical shaking device by supplying the plans for a device he built to isolate lateral vibrations in a Faraday wave apparatus. The guys in the shop (Sam,

Butch and Norman) carefully manufactured numerous experimental parts and were always willing to help out in whatever I was trying to build. I am indebted to many of the graduate students at Georgia Tech for their conversations and suggestions. Also to the members of my review committee, each of whom spent a significant amount of time discussing the experimental results. However, I am most thankful to my wife (Jessica) for her support and love. Without Jessica none of this would be possible.

# CHAPTER 1

## Introduction

A central approach in dynamical systems investigations is to vary a stress parameter and examine the influence of nonlinearity on the different levels of complexity displayed by the system. Traditionally, these investigations have focused on examples in the limits of a few or infinitely many degrees of freedom. Systems in the limit of a few degrees of freedom are spatially discrete and low dimensional, while those in the opposite limit are continuous and spatially extended. Many of the dynamical systems concepts (including chaos) have been formalized in the few degrees of freedom limit where phase space structures provide a convenient means of dynamics description.

An example of a system with a few degrees of freedom is an array of three Josephson Junctions. A single Junction is produced by separating two superconductors by a layer of weakly insulating material, the thickness of the layer depends on the material used. When a relatively small bias current  $I$  is applied across a Junction, electrons in Cooper pairs will pass (tunnel) through the weak insulator without any resistance, so there is no voltage across the Junction. Increasing  $I$ , there is an abrupt transition after which the current is not strictly superconducting. The emerging voltage oscillates at up to terahertz frequencies. Applying Kirchhoff's laws, a single Junction may be mapped onto the ordinary differential equation of a damped pendulum under

constant torque. Due to its physical properties, each Josephson Junction will possess its own intrinsic oscillation frequency. In the example, the array of Josephson Junctions may be described by three coupled pendulums, each with its own characteristic frequency. As  $I$  (the stress parameter in this case) across the coupled Junctions is varied, the voltage may display a range of behaviors from zero signal to quasiperiodic oscillations. One of the more substantial contributions of dynamical systems has been the appreciation of the levels of complexity possible in the limit of only a few degrees of freedom. Chaos, for example, only requires three degrees of freedom to be an accessible state.

Spatially extended systems, not surprisingly, are also capable of a large range of behaviors as a stress parameter is varied. One of the most extensively studied and well understood examples is a fluid layer of horizontal extent with an upper bounding surface at a temperature  $T_1$  and a lower bounding surface at a higher temperature  $T_2$  ( $T_2 > T_1$ ). At relatively small temperature difference  $\Delta T = T_2 - T_1$ , heat is simply conducted across the layer and there is no fluid motion. As  $\Delta T$  is increased fluid motion occurs at a well defined threshold, resulting in spatial variations (patterns) with some regular periodicity. With increasing driving ( $\Delta T$ ) the fluid motion becomes more complex, eventually aperiodic.

Prior to the developments of dynamical systems the transition to turbulence was understood to be due to a large number of discrete transitions, each of which introduced a different frequency into the fluid velocity field. This picture of the transition to turbulence proposed by Landau [3] results generically in complex flow and a relatively high dimensional quasiperiodic attractor. By contrast, the transition to turbulence originally proposed by Ruelle & Takens [4] indicates turbulence generically

occurs after only four Hopf bifurcations. Ruelle, Takens, & Newhouse clarified the earlier ideas about the onset of aperiodic behavior by showing (1978) that after three Hopf bifurcations a strange attractor was likely, although three period quasiperiodic behavior could also exist. This dynamical systems description predicts turbulence is an aperiodic behavior associated with a strange attractor. Experimental evidence questioning the Landau picture was first reported by Ahlers [5] in 1974 and supported by the numerical work of McLaughlin & Martin [6]. Both of these investigations examined heat flow in a fluid layer as an imposed  $\Delta T$  was varied and showed that aperiodic behavior was not the result of a large number of discrete transitions. Subsequently, several investigators studied the onset of aperiodic behavior in a variety of fluids with an imposed temperature difference, as well as in other fluid experiments. These experimental results in various systems supported different routes to aperiodic behavior that all shared the characteristic that only a few bifurcations were required for aperiodic behavior to arise. In this limit of infinitely many degrees of freedom, dynamical systems investigations have shown that aperiodic behavior is in some sense not as complicated as previously thought.

## 1.1 Spatially Extended Systems

Behavior of spatially extended systems as they are driven away from equilibrium remains an active area of research across a large number of disciplines [7]. Understanding of the mechanisms for the transition from uniform states to patterns of a single wave number are relatively well developed in a large number of examples. Theoretical descriptions of the nonequilibrium systems are typically based on microscopic

considerations which result in equations of motion that are continuous in space and time. The complexity of these partial differential equations typically elude analytical treatment and require sophisticated techniques to solve numerically. To determine the transition from a uniform state to a pattern, the appropriate equations of motion are linearized about the uniform state. Stability of the uniform state is studied by considering a set of discrete wave numbers. When the largest real eigenvalue for a given value of the stress parameter over all wave numbers is negative the uniform state is stable. A positive largest eigenvalue indicates the uniform state is unstable to the corresponding wave number. The border between a stable and unstable uniform state corresponds to a zero largest real eigenvalue, marginal stability. Typically, a single wave number  $q_c$  will be marginally stable at a critical value of the stress parameter.

Pattern structure near onset can be investigated by applying perturbation methods to produce model equations for the pattern amplitudes. These amplitude equations may be derived from first principles or written by inspection, but are exact only in the limit of onset [7]. The general form of an amplitude equation is

$$\partial_t A_i = \epsilon A_i + \sum_j g_{ij}(A_i A_j + c.c.) + \sum_{j,k} g_{ijk}(A_i A_j A_k + c.c.) + \dots + \partial_x^2 A_i, \quad (1)$$

where  $A$ 's are complex and  $g$ 's are properly chosen constants. Though still generally partial differential equations, amplitude equations are much simpler than the original equations of motion. Symmetries present in the system are reflected by the structure of the terms in the amplitude equations and play a major role in selecting the planforms present at onset.

### 1.1.1 Rayleigh-Bénard Convection

A fluid layer with an imposed temperature difference is a canonical example of a spatially extended system. In equilibrium the fluid layer will be in a macroscopically uniform state; homogeneous and isotropic. One way to drive the fluid out of equilibrium is to bring it into contact with a heat reservoir, say by heating the bottom surface while keeping the top surface at constant temperature  $T_1$  (Rayleigh-Bénard convection). For sufficiently small  $\Delta T$  the laterally uniform state persists as a linear gradient is established in the vertical temperature field. With increasing  $\Delta T$  an unstable situation arises as it becomes energetically favorable for a hotter (thus lighter) volume element near the bottom to change positions with a cooler (heavier) element near the top despite viscous damping. This buoyancy driven instability leads to the emergence of fluid flows as the mechanism for enhanced heat transport and results in patterns in the fluid fields: temperature, velocity, and pressure. Near the onset of fluid motion flows form regular periodic structures whose spatial structure is determined by system symmetries.

A Rayleigh-Bénard convection system (of infinite horizontal extent) may be described by only two dimensionless quantities: Rayleigh number  $R$  and Prandtl number  $Pr$ . These quantities are defined in terms of the dimensional properties of fluid: kinematic viscosity  $\nu$ , thermal diffusivity  $\kappa$ , thermal expansion coefficient  $\alpha$ ,  $\Delta T$ , vertical fluid depth  $d$ , and gravitational acceleration  $g$ , by

$$R = \frac{g\alpha d^3 \Delta T}{\nu\kappa} \quad \text{and} \quad Pr = \frac{\nu}{\kappa}. \quad (2)$$

Conceptually,  $R$  may be thought of as a nondimensional  $\Delta T$ , properly normalized by the fluid physical properties and depth of the layer. For a fluid of infinite lateral

extent, regardless of the working substance, convection occurs for  $R > 1708$ . The characteristic system length scale is  $d$ , while the vertical diffusion time  $t_\nu = d^2/\kappa$  and vertical viscous relaxation time  $t_\eta = d^2/\nu$  serve as characteristic temporal scales. In these terms the Prandtl number may be understood as the ratio of the two temporal scales ( $Pr = t_\nu/t_\eta$ ).

In the original experimental work reported by Bénard [8, 9] a dish of fluid was heated from below producing a pattern of regular hexagons near onset. These observations were later (1916) explained by Lord Rayleigh [10] in terms of the buoyancy driven instability described in the previous paragraph. Due to their contributions buoyancy driven instability in a fluid layer with an imposed temperature difference and no free surfaces became known as Rayleigh-Bénard convection. Subsequently (1958), the hexagons Bénard observed were explained by Pearson [11] to be due to a surface tension instability that preceded the buoyancy instability considered by Rayleigh. Studies of the former instability are now known as surface tension driven Bénard convection (or Bénard-Marangoni convection).

Onset planforms selected by patterns depend on the degree to which inversion symmetry is present. Inversion symmetry requires field equations to be invariant under inversion of the field variables ( $A \rightarrow -A$ ) [7]. In Rayleigh-Bénard convection an example of inversion symmetry is the property that a pattern (for example, stripe state velocity field) becomes inverted after a spatial reflection about the fluid layer mid plane. This so-called Boussinesq symmetry requires any equation description [for example, Eq. (1)] be invariant under the reflection of the field variables. The degree to which Boussinesq symmetry is present determines the significance of terms with even power exponents in the amplitude equations. In a perfectly Boussinesq fluid the

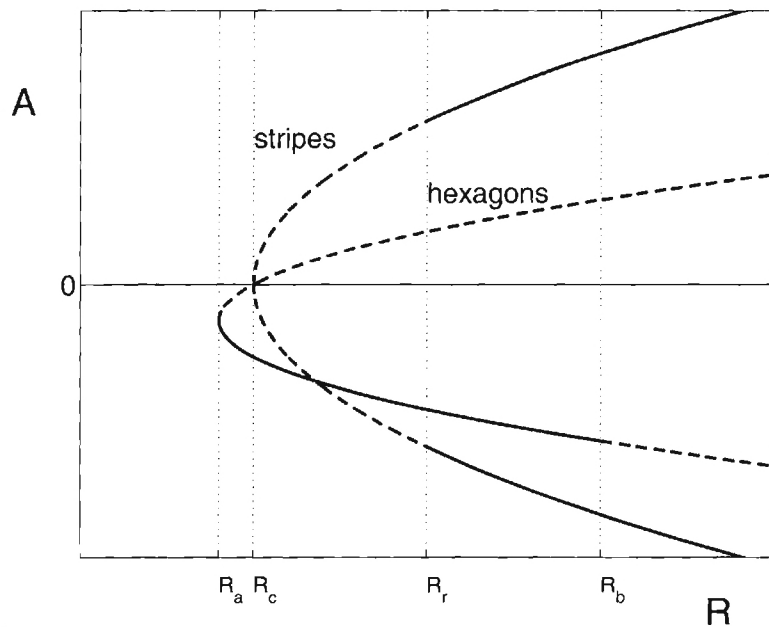


Figure 1: Bifurcation diagram for classical Rayleigh-Bénard convection at onset in a non-Boussinesq fluid in terms of pattern amplitude  $A$  as the stress parameter  $R$  is varied. For increasing  $R$  onset occurs at  $R_c$ . Solid lines are stable solutions and dashed lines are unstable solutions. This diagram is appropriate for hexagons with downflowing centers (light). For the upflowing centers (dark) the hexagon bifurcation diagram would be reflected about  $A = 0$ .

quadratic coefficient [ $g_{ij}$  in Eq. (1)] would be zero. As this approximate symmetry is increasingly violated the magnitude of the quadratic coefficient grows. In Rayleigh-Bénard convection where there is no free surface Boussinesq symmetry is exact in the limit where the fluid density varies linearly with temperature and all the other fluid properties are not temperature dependent, thereby independent of vertical position. When the Boussinesq symmetry is present the leading order nonlinear term is cubic [Eq. (1)] and parallel stripes (single wave), which have no preferred orientation, are observed at onset. The amplitude of these stripes increases continuously from zero at onset. In the absence of Boussinesq symmetry regular hexagons (superposition of three waves each separated by  $60^\circ$ ) are found at onset (Fig. 1). The leading order nonlinear term is then quadratic which allows two modes to resonate (interact) with a third according to a *resonant triad* condition. This wave number resonance stimulates three modes at the critical wave number  $q_c$  separated by  $60^\circ$  in the wave number domain. At onset the hexagon amplitude appears discontinuously as shown in Fig. 1. Moving away from onset the hexagons and stripes become simultaneously stable  $R_r < R < R_b$  and eventually  $R > R_b$  hexagons lose stability to parallel stripes provided the side wall influence is minimal. The parameter range over which hexagons are observable increases as the Boussinesq symmetry is increasingly violated. In this way linear terms dictate the critical point (stress parameter & wave number) while nonlinear terms select the pattern structure near onset.

### 1.1.2 Taylor-Couette Flow

Another commonly studied pattern forming system discussed in this dissertation is the flow of a Newtonian fluid between two concentric cylinders, one or both of which

are rotating (Taylor-Couette flow). At rotation rates below a critical value only the azimuthal velocity field is non vanishing (uniform state). At a critical value in rotation rate Taylor Vortices [12] form as radial and axial components arise in the velocity field forming a pattern. Axial periodicity occurs at roughly twice the gap between the cylinders [13]. With increasing angular velocity, Taylor Vortices will lose stability to more complicated states, until at large enough angular velocity aperiodic flows are observed. Experimental studies of this system also reported [14] early indications that the Ruelle-Takens picture of the route to turbulence is a more appropriate description than the Landau picture. When fluid motion in the annulus is (near) laminar the fluid is Newtonian; viscous stresses are proportional to the velocity gradient.

While contemporary Taylor-Couette studies are interested in the bifurcations, symmetry-breaking and associated pattern complexities that occur as the rotation rates are varied in smooth and spatially complicated containers, interest in fluid motion between two rotating cylinders can be traced back at least as far as Sir Isaac Newton. In *Principia* (1687) Newton wrote about the expected flow in a annulus between two rotating infinitely long cylinders [15] (section 9, book II). By 1888, Arnulf Mallock and Maurice Couette had separately built the first experimental devices to rotate cylinders about a fluid annulus, although their primary goal was to determine viscosity. In 1923 [12] Taylor considered the annulus fluid motion and compared predictions arising from the equations formulated by Navier (1823) and Stokes (1845) for the onset of laminar flow with his experimental observations. Taylor performed the associated linear stability without the benefit of computers and his results were considered confirmation of both the Navier-Stokes equations and no-slip boundary conditions.

### 1.1.3 Faraday Surface Waves

Both of the pattern forming systems introduced to this point are typically driven by time independent forcing. A pattern forming system driven strictly by time dependent forcing is a vertically oscillated open dish of fluid. Instability in this system is parametrically driven and results in the formation of surface waves. Michael Faraday [16] first (1831) investigated the instability leading to standing surface waves on the free surface of a fluid in a vertically oscillated container as the amplitude was increased (Faraday surface waves). Typically, surface waves in a Faraday wave experiment display a subharmonic time dependence, they respond at half the drive frequency. Thereby, a discrete time translation by a drive period inverts the fluid surface, rendering the surface periodic at twice the drive period. This subharmonic discrete time translation symmetry is a temporal form of inversion symmetry. If it is present, regular stripes or squares are observed at onset.

In the absence of inversion symmetry hexagons and complex-ordered patterns [17] may be observed in Faraday surface waves. The inversion symmetry of time translation may be broken by inducing a harmonic response of the fluid to the vertical oscillations. Investigators have successfully induced harmonic fluid response through the use of very thin fluid layers, a viscoelastic fluid, or by using multiple judiciously chosen forcing frequencies. Regardless of the mechanism for breaking time translation symmetry, the effect is to allow resonant triads to form. As observed in the discussion of non-Boussinesq Rayleigh-Bénard convection (Sec.1.1.1) these nonlinear interactions may result in the formation of hexagons. Additionally, it has recently been found that resonant triads can lead to the formation of complex-ordered patterns (Fig. 2) which

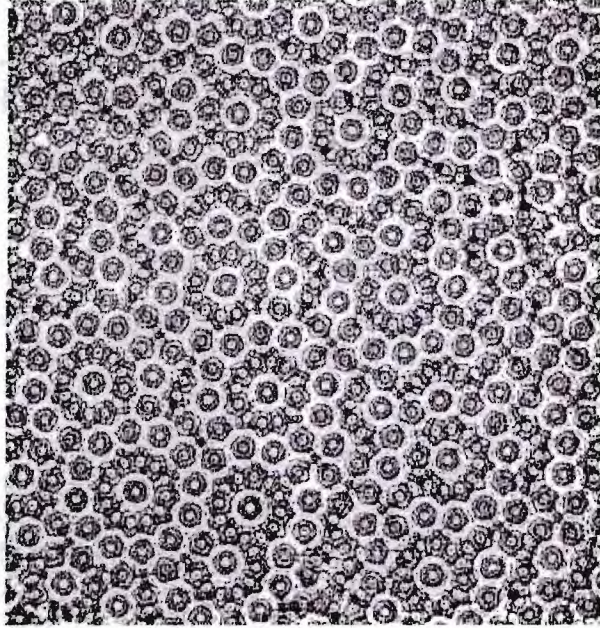


Figure 2: Twelve-fold symmetric quasicrystalline pattern in Faraday surface waves, reported by Gollub & Langer [2].

have the characteristics of non-trivial spatial structure described by a finite number of modes on interacting sublattices. Borrowing from condensed matter terminology, if these exotic patterns possess a unit cell which covers the plane they are called *superlattices* (i.e. square or hexagonal unit cell), while if the unit cell cannot fill the plane (i.e. pentagonal unit cell) they are called quasicrystals or quasipatterns.

Study of complex-ordered states in pattern forming systems is a relatively recent topic. On the basis of quasicrystals in microscopic systems Malomed, Nepomnyashchiĭ & Tribelskiĭ [18] first predicted macroscopic quasicrystals in spatially extended dissipative systems in 1989. Using a viscoelastic fluid and a single oscillation frequency eightfold symmetric quasipatterns were first experimentally confirmed in 1992 by Christiansen, Alstrøm & Levinsen [19]. Soon after (1993) Edwards & Fauve reported

[20] 12-fold quasipatterns when imposing two frequency forcing on a Faraday wave apparatus using a viscous fluid. Initial reports of superlattices were simultaneously made in different journals by Kudrolli, Pier & Gollub [21] and Arbell & Fineberg [22] in 1998. Both studies examined a viscous fluid in a Faraday wave apparatus subject to two frequency forcing over different parameter values. Later, Arbell & Fineberg [23] reported additional superlattices in the same system. Complex-ordered patterns have also been recently been reported in optical and ferrofluid [24] experiments. In the optical examples spatial symmetries in the quasipatterns and superlattices are usually imposed [25, 26, 17], but not always [27]. Mechanisms in the ferrofluid system are the same as in the Faraday surface waves.

Resonant triads have been found to be the formation mechanism of all the previously discussed complex-ordered patterns. These resonant three wave interactions may occur between modes on the same sublattice, between modes on different sublattices or between stimulated modes and other weakly damped (near critical) modes. In the various patterns there is a variety of these interactions, but they are almost always between three waves. The one exception occurs in the first experimental observation of macroscopic quasicrystals [19] in surface standing waves. In this case, the eightfold symmetric quasicrystals were attributed to the existence of four standing waves. Resonant triads, however, are the ubiquitous mechanism by which previously reported complex-ordered patterns form.

## 1.2 Effects of Time Dependent Modulation

Introducing time dependent modulation to a system driven by time independent forcing can lead to a variety of unexpected changes. In the mechanical example of a planar pendulum, parametric modulation can be introduced by vertically oscillating the base. This driving alters the stability of solutions observed in the absence of oscillation. Without modulation there are two solutions: hanging which is stable and inverted which is unstable. Vertically oscillating the base can destabilize the hanging solution. Conversely, the inverted solution can be stabilized by the modulations. By analogy with the pendulum, patterns in spatially extended systems subject to significant parametric modulation are expected to change stability. Time dependent modulation in pattern forming systems driven by time independent instabilities has been realized in a few hydrodynamic experiments. Results from these investigations have indicated that modulation shifts the onset of instability (either stabilizing or destabilizing the uniform state). However, several other predictions about the influence of time dependent modulation have remained unconfirmed due to physical limitations of the modulation realizations.

## 1.3 Outline

The primary focal point of this dissertation is the effects of time dependent modulation on a canonical pattern forming system driven by time independent forcing; Rayleigh-Bénard convection. The dissertation body is divided into four chapters. Chapter 2 introduces the effects of parametric modulation by solving the mechanical system of a pendulum with an oscillating pivot point. Stability in the modulated system is shown

to change from that in the unmodulated case by closed form relations defining solution stability. Second, the relevant literature describing the effects of modulation on three pattern forming systems is reviewed. Experimental results in this literature have been constrained to a relatively narrow parameter range and unable to investigate some predictions. For the system considered in this dissertation experiments were not previously feasible and calculations are done to demonstrate how the development of compressed gas convection in the 1990s facilitates experimental results reported here. Chapter 3 details the experimental devices which were constructed to perform the laboratory investigations. Additionally, analysis tools and numerical methods are introduced. Chapter 4 reports experimental and numerical results directly relevant to addressing previously made predictions as well as considering the patterns present at onset. Chapter 5 details patterns found away from onset. Over relatively small values of the modulation parameters the experiment is dominated by the thermal driving, *i.e.*, it is similar to classical Rayleigh-Bénard. At relatively large modulation parameter values the modulations dominate the pattern formation. A parameter regime where flows from both driving types compete and coexist is found and detailed. When the two driving types have relatively equal influence several complex-ordered patterns are reported for the first time in a convection system. A mechanism for the formation of these patterns is identified and symmetries present in the system are found to play a key role in the formation of these patterns directly from the uniform state. Finally, directions for future studies are proposed.

The stability calculations described here (Sec. 3.6.1) were performed by Jon Bougie and Jack Swift at the University of Texas - Austin. Extensive numerical work, including all simulations investigating patterns were performed by Werner Pesch and

Oliver Brausch at Physikalisches Institut der Universität Bayreuth in Germany. The numerical methods used for pattern simulations are detailed in the Ph.D. dissertation of Oliver Brausch [28].

## CHAPTER 2

# Parametric Modulation

Parametric modulation of a system can alter the stability of unmodulated states and result in novel behavior. A common mechanical example is a planar pendulum whose base is periodically oscillated in the vertical direction. When the base is stationary (no oscillations) the pendulum has two mathematical solutions: hanging and inverted. In the absence of driving only the hanging solution is physically observed. Friction is always present in physical systems resulting in any small perturbation of the hanging solution dying out as the pendulum returns to its steady state; this solution is said to be stable and attracting. By contrast, the other mathematical solution is unstable and repelling since any perturbation of the inverted state results in the pendulum falling over and eventually settling into the hanging position, thereby changing state. Introducing parametric forcing by vertically oscillating the pendulum base may alter the stability of both solutions. Depending on the amplitude and frequency of base oscillations the hanging solution may be destabilized while the inverted solution may be stabilized.

Studies of the effect of time dependent modulation on hydrodynamic pattern formation produced by a time independent instabilities began as a conversation between two University of California researchers [29]. In the early 1960s Harry Suhl was at

UC-San Diego and working on ferromagnetic resonance in the presence of parametric modulations [30, 31]. During a visit to UC-Berkeley he and a member of the Berkeley physics faculty (F. Reif) discussed the potential effects of modulation on hydrodynamics. At that time Russell Donnelly was a young Assistant Professor at University of Chicago who was working on hydrodynamics in Taylor-Couette flow experiments. Suhl and Reif placed a call to Donnelly and within a few days they had begun the first set of modulated hydrodynamic experiments. In particular, Donnelly implemented parametric forcing by periodically modulating the inner cylinder rotation rate about nonzero mean while the outer cylinder was held fixed. After collecting data during the summer of 1962 Donnelly, Reif and Suhl reported [32] the initial results of these seminal experiments. They concluded parametric modulation stabilized the fluid motion over the parameter range considered. Donnelly continued working on the problem and after performing more extensive experiments in the summer of 1963 he reported further results in 1964 [33] confirming the initial observations of stabilization.

Limitations in accessible parameter range, complications in the theoretical description and difficulties in interpreting the initial modulated Taylor-Couette flow results stimulated investigation into other related hydrodynamic systems [34]. The experimental fluid has a limited response to the modulation of cylinder rotation rates given by the propagation of a viscous wave. This limitation restricts rotation modulated Taylor-Couette experimental trials to small modulation displacement amplitudes and low modulation frequencies. Interpretation of experimental results also proved problematic. There were several disagreements between experimental and theoretical results reported in the literature, both quantitative and qualitative. These

disagreements were the basis for a number of additional investigations which eventually resolved the discrepancies and demonstrated some observations made in the initial experiments by Donnelly, Reif and Suhl [32] and Donnelly [33] had been misinterpreted. These problems stimulated a second line of modulated hydrodynamics inquiry where the temperature gradient in a Rayleigh-Bénard convection cell was periodically modulated about nonzero mean [34]. Modulation was achieved by oscillating either the bottom surface temperature or both the bottom and top surface temperatures. While thermally modulated Rayleigh-Bénard convection is more amenable to theoretical analysis it is also severely limited in dynamical parameter range since the fluid again is restricted in its response to modulations. In this case, the propagation of thermal waves are the limitation.

A third line of modulated hydrodynamics inquiry that does not suffer from the same physical limitations as the two previous examples is Rayleigh-Bénard convection in the presence of time-periodic acceleration (acceleration modulated Rayleigh-Bénard convection). Theoretical and numerical [35] investigations of acceleration modulated Rayleigh-Bénard have predicted stability changes similar to those of the previous two examples, but the lack of any experimental results has limited the number of investigations.

This Chapter is intended to put the experimental and numerical results on acceleration modulated Rayleigh-Bénard convection to be reported in Chapters 4 & 5 in context. Section 2.1 presents a stability analysis of a simple mechanical system, a planar pendulum. Parametric modulation is introduced by time-periodic oscillations of the pendulum base. As a result of the modulation, stability of the unmodulated

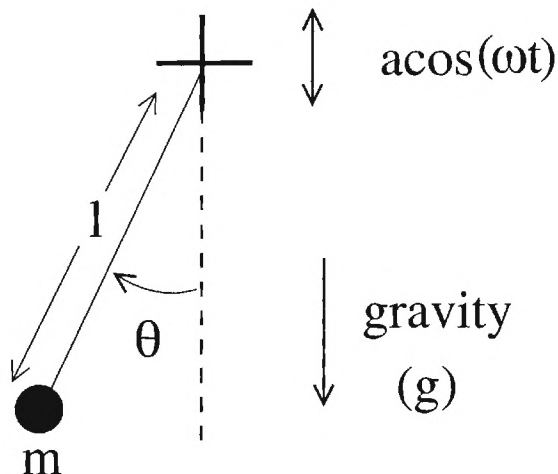


Figure 3: A pendulum with a vertically oscillating base.

solutions is shown to change over parameter ranges. Closed form stability conditions are derived for this relatively simple example. Section 2.2 reviews the existing literature on modulated hydrodynamics by examining three realizations that have been extensively studied: rotation modulated Taylor-Couette, thermally modulated Rayleigh-Bénard convection, and acceleration modulated Rayleigh-Bénard convection. Consistent predictions of the effects of modulation exist for all three cases, although experiments have only been performed for the first two examples. Order of magnitude calculations demonstrate why prior to this work no acceleration modulated Rayleigh-Bénard convection experiments have been reported.

## 2.1 Mechanical Analogy

Insight into the possible effects of parametric modulation on hydrodynamic stability can be gained by considering the well-studied mechanical system of a planar pendulum

with an oscillating base (Fig. 3). In the absence of base oscillations ( $\omega = 0$ ) the Lagrangian for the pendulum is

$$L(\theta) = \frac{1}{2}ml^2\dot{\theta}^2 + mgl \cos \theta. \quad (3)$$

The corresponding equation of motion is given by

$$\ddot{\theta} + \omega_0^2 \sin \theta = 0, \quad (4)$$

with a single variable  $[\theta(t)]$  and  $\omega_0^2 = g/l$ . Eq. (4) has two solutions (eigenstates) where  $\ddot{\theta}_* = \dot{\theta}_* = 0$ :  $\theta_* = 0$  (hanging) and  $\theta_* = \pi$  (inverted). These eigenstates correspond to fixed points in phase space. Rewriting the equation of motion as two first order equations,

$$\begin{aligned} \dot{\theta} &= \psi & \text{and} \\ \dot{\psi} &= -\omega_0^2 \sin \theta, \end{aligned} \quad (5)$$

allows the fixed point stability to be found from the eigenvalues  $\lambda$  of the associated Jacobian,

$$\det(\mathbf{J} - \lambda\mathbf{I}) = \begin{vmatrix} \frac{\partial \dot{\theta}}{\partial \theta} - \lambda & \frac{\partial \dot{\theta}}{\partial \psi} \\ \frac{\partial \dot{\psi}}{\partial \theta} & \frac{\partial \dot{\psi}}{\partial \psi} - \lambda \end{vmatrix} = \begin{vmatrix} -\lambda & 1 \\ -\omega_0^2 \cos \theta & -\lambda \end{vmatrix}. \quad (6)$$

In general these eigenvalues will be complex. The real parts indicate stability and the rate of approach while the imaginary components set the oscillatory frequencies. The sign of the real component determines stability; eigenstate is stable if  $\Re(\lambda) < 0$  and unstable if  $\Re(\lambda) > 0$ . In phase space,  $\Re(\lambda) < 0$  corresponds to a flow tending towards a solution (associated state is attracting) while  $\Re(\lambda) > 0$  indicates the flow of states is moving away from a solution (associated state is repelling). The rate

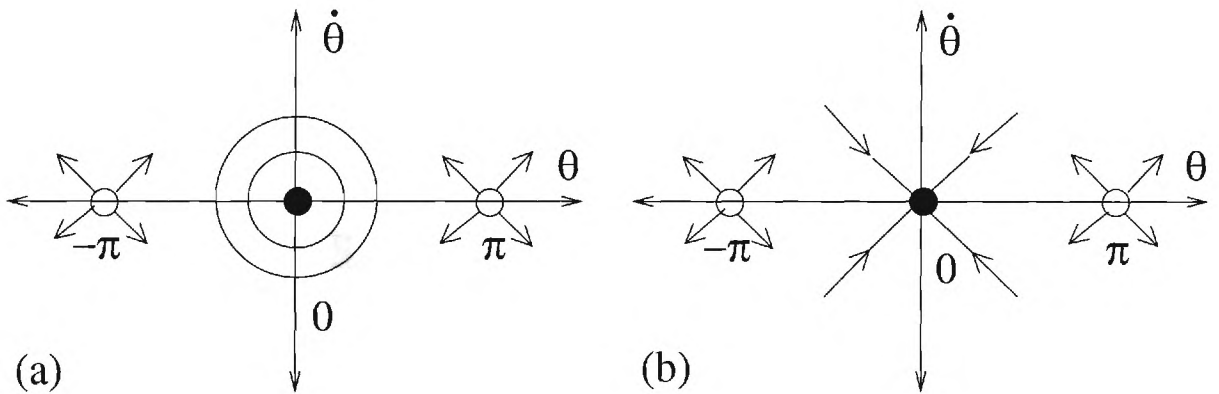


Figure 4: Phase space plots for an oscillator (a) without dissipation and (b) with dissipation.

at which the flow is moving towards a solution is given by the magnitude of  $\Re(\lambda)$ . Along the boundary between stable and unstable [ $\Re(\lambda) = 0$ ] perturbations do not grow or decay (fixed point is marginally stable). At  $\theta_* = 0$ ,  $\Re(\lambda) = 0$  meaning in the absence of dissipation the pendulum is marginally stable, Fig. 4(b). Physically a small displacement of the hanging state will result in the pendulum harmonically oscillating about  $\theta = 0$  with constant maximum amplitude. If friction were included the  $\Re(\lambda) < 0$  and  $\theta_* = 0$  would be stable and attracting [Fig. 4(a)]. For the case without friction the oscillation frequency will given by the imaginary part of the Jacobian's eigenvalue [ $\Im(\lambda) = \omega_0$ ]. Conversely, at  $\theta_* = \pi$ ,  $\Re(\lambda) > 0$  and the pendulum is unstable. The associated fixed point is repelling. Any perturbation about  $\theta_* = \pi$  results in the pendulum falling over while in phase space the flow will move away from this fixed point ( $\theta_* = \pm\pi, \dot{\theta}_* = 0$ ), Fig. 4(b).

Time-periodic vertical base oscillations cause the hanging ( $\theta_* = 0$ ) solution to become unstable over a range of oscillation amplitude and frequency. Vertical oscillations of the base can be included in the previous equation of motion by allowing

gravity to become time dependent [ $g(t) = g + a \cos(\omega t)$ ]. The equation of motion is then given by

$$\ddot{\theta} = -\omega_0^2[1 + \epsilon \cos(\omega t)] \sin \theta, \quad (7)$$

where  $\epsilon = \frac{a}{g}$  is a nondimensional acceleration. Eq. (7) is a form of the Mathieu equation with the same fixed points as in the absence of modulation ( $\omega = 0$ ):  $\theta_* = 0$  and  $\theta_* = \pi$ . Parametrically forced systems typically display a response at half the drive frequency. With this in mind, fixed point stability can be investigated in the small angle approximation ( $\sin \theta \approx \theta$ ) by assuming a solution, called an ansatz, and looking at the conditions under which the assumption is valid. Plugging the ansatz  $\theta(t) = e^{\lambda t} \cos(\frac{\omega}{2}t + \pi)$  into Eq. (7) and applying the technique of harmonic balance leads to the  $\lambda^2$  characteristic equation

$$\lambda^2 = -\left(\frac{\omega^2}{4} + \omega_0^2\right) + \sqrt{\omega^2\omega_0^2 + \omega_0^4\epsilon^2/4}. \quad (8)$$

The boundary between stable and unstable parameters coincides with  $\lambda^2 = 0$ . Thereby, marginal stability occurs when

$$\epsilon = \epsilon_0 = 2 \left| \frac{\omega^2}{4\omega_0^2} - 1 \right|. \quad (9)$$

Looking back at Eq. 8 indicates

$$\theta_* = 0 \quad \text{is} \quad \begin{cases} \text{stable,} & \epsilon < \epsilon_0 \\ \text{unstable,} & \epsilon > \epsilon_0 \end{cases}, \quad (10)$$

as graphically shown in Fig. 5(a).

Conversely, an oscillating base causes the inverted solution ( $\theta_* = \pi$ ) to become stable over a range of  $\epsilon$  and  $\omega$ . To use a small angle approximation transform the

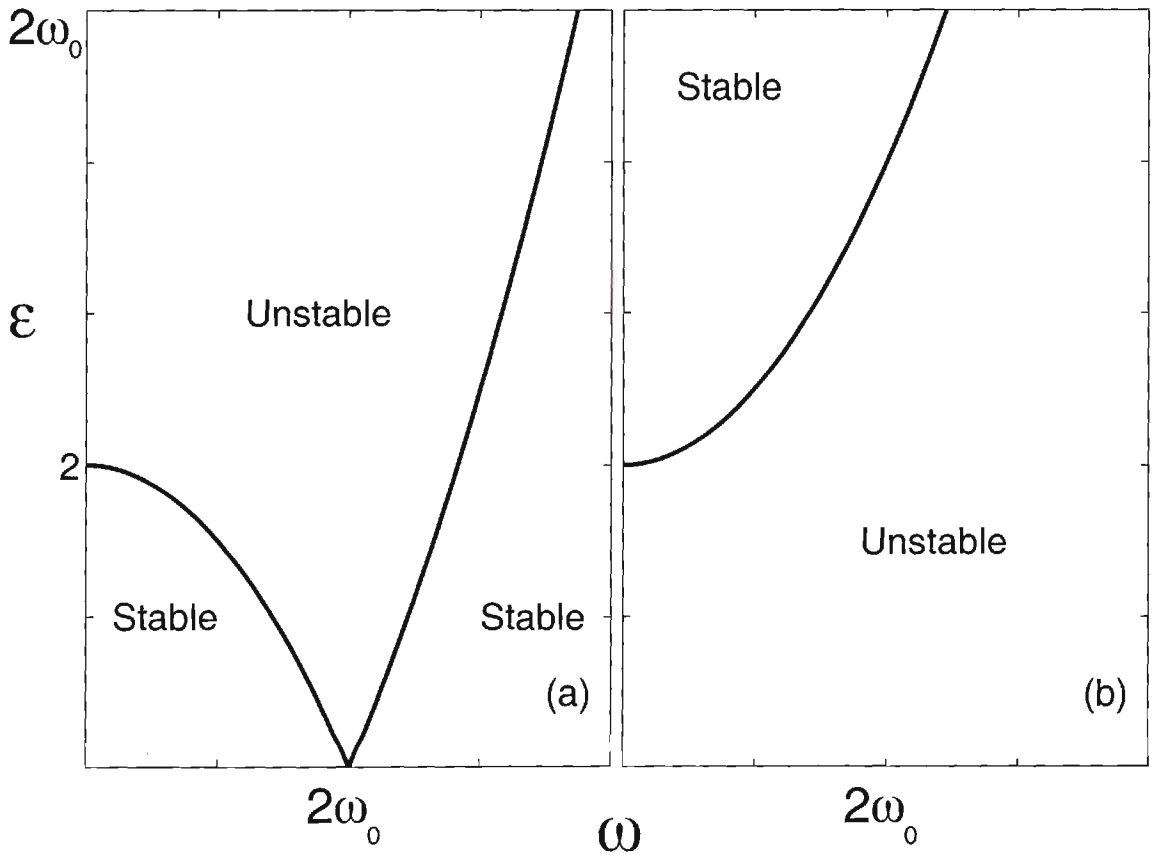


Figure 5: Stability plots in terms of the nondimensional acceleration ( $\epsilon$ ) versus the oscillation frequency  $\omega$  for (a) a hanging pendulum and (b) an inverted pendulum.

reference axes by letting  $\theta = \theta_1 + \pi$  and plug into Eq. (7). The equation of motion becomes

$$\ddot{\theta}_1 = \omega_0^2(1 + \epsilon \cos \frac{\omega}{2}t) \sin \theta_1. \quad (11)$$

Notably the only change from the hanging case is the sign of the  $\sin \theta_1$  coefficient. Using the previous ansatz, plugging into the equations of motion and pushing through the same calculation as for the hanging solution leads to the marginal stability condition

$$\epsilon = \epsilon_o = 2\left(\frac{\omega^2}{4\omega_0^2} + 1\right). \quad (12)$$

The corresponding stability diagram is shown in Fig. 5(b). Notably, the only difference between the hanging and inverted calculations is the sign of  $\omega_0^2$  throughout.

While the planar pendulum is a highly simplified model it does bring out some interesting effects which might be expected in more complex systems subject to time-periodic modulation. Stability of system states may be altered, causing either stabilization or destabilization. Physically unobserved states, like the inverted pendulum, may be stable – even attracting over a range of parameters. Additionally, these stability changes may lead to novel behaviors and unanticipated transitions between states that were not observed in the absence of modulation.

## 2.2 Modulated Hydrodynamics

Drawing an analogy between an unstable fluid and the inverted pendulum one might expect modulation of a fluid system would lead to stability changes and potentially, observation of new states. Initial experimental results for rotation modulated Taylor-Couette flow [32, 33] indicated modulation stabilized fluid motion at some finite

(small) modulation and had diminishing effect with increasing modulation. Besides the fundamental questions of understanding the effects of modulation on hydrodynamics these results had numerous potential applications in industrial processes. In manufacturing the rate of production can be limited by the rate at which laminar or smooth flow is maintained in the process, for example in paper production. The ability to improve stabilization of these processes so that higher flow rates could be attained while maintaining laminar or smooth flow could then allow production rates to be increased. As will be discussed in Sec. 2.2.1 interpretation of these early experiments were questioned and lead to numerous other experimental, numerical and theoretical investigations.

Due to the similarities between Taylor-Couette flow and Rayleigh-Bénard convection instabilities a number of investigators chose the latter system in an effort to gain more definitive results [34]. The instability in Rayleigh-Bénard convection is buoyancy driven and the initial investigations modulated this driving by imposing sinusoidal bounding plate temperature variation about nonzero mean. While the theoretical description in this case was more manageable the laboratory investigations suffered from physical limitations similar to those present in modulated Taylor-Couette flow. The limited physical response of the fluid to driving restricted accessible modulation parameters to small displacement amplitudes and low frequencies. At high frequency all modulation is confined to a very thin Stokes layer at the boundary [36]. Experimental results for this system appeared consistent with those observed in Taylor-Couette flow, but the limitations in dynamical range again restricted experiments to focusing on shifts in initial onset of fluid motion over a relatively small modulation range.

In addition to thermal modulation stabilizing conduction other investigators [36,

[37] predicted fundamental changes to the onset of convection. In the initial investigations of thermally modulated Rayleigh-Bénard it was assumed the onset planform would be parallel stripes. However, it was shown by Roppo, Davis, & Rosenblat [36] that the onset planform should actually be hexagons. Thermal modulations caused inversion symmetry to be broken over a range of parameters initial calculations indicated should be experimentally observable. Initial experiments [38] did not observe the predicted hexagons and subsequent theoretical work [37] indicated the hexagons would be difficult to find then previously predicted [36]. Another set of experiments [39] did observe the hexagons, but additionally found interesting patterns composed of intermixed stripes and hexagons not previously considered.

*Buoyancy in a Rayleigh-Bénard convection apparatus* can also be modulated by vertically oscillating (shaking) the fluid layer. The oscillations result in time dependent acceleration in the frame of the fluid. This type of driving force modulation is not limited in dynamical range as the previous two examples since the variation in acceleration is propagated vertically through the thin fluid layer at approximately the speed of sound. However, attaining dimensionless parameters significantly large enough to observe interesting behavior requires dimensional modulation amplitudes which were until recently prohibitively large. Thereby, only theoretical and numerical investigations of acceleration modulated Rayleigh-Bénard convection have been reported.

The remainder of this chapter will review existing literature for all three mentioned forms of pattern forming systems with an additional parametric modulation:

rotation modulated Taylor-Couette flow, thermally modulated Rayleigh-Bénard convection and acceleration modulated Rayleigh-Bénard convection. The initial theoretical/numerical investigations as well as the experimental trials have focused primarily on establishing changes in stability near the initial onset of fluid motion while other interesting modulation effects have remained unconfirmed or simply unreported.

There are other forms of modulated hydrodynamics which are currently being investigated. One example where preliminary results also indicate modulation has a stabilizing effect is a Rayleigh-Bénard convection apparatus rotated about the vertical at a rate modulated about nonzero mean [40]. Other interesting examples include cases where the modulation is spatial instead of temporal. Examples of the latter case include Taylor-Couette flow apparatuses where the cylinder walls are spatially periodic [41]. For spatially modulated Taylor-Couette flow the modulation causes both destabilization and stabilization in comparison to the unmodulated flow that is qualitatively similar to the results for rotation modulated Taylor-Couette flow.

### 2.2.1 Rotation Modulated Taylor-Couette Flow

As discussed in the introduction modulated hydrodynamic studies began in the early 1960s with reports of experimental work by Donnelly, Reif, & Suhl (1962) [32] and Donnelly (1964) [33]. Their seminal investigations examined flow stability in a Taylor-Couette flow apparatus when the outer cylinder was held fixed and the inner cylinder rotated with periodic modulations about some mean rotation rate,  $\Omega = \bar{\Omega} + \Delta\Omega \cos(\omega t)$ : mean rotation rate  $\bar{\Omega}$ , modulation amplitude  $\Delta\Omega$ , and modulation frequency  $\omega$ . They reported modulation stabilized the fluid over a restricted  $\omega$  range and had little effect at relatively large or small  $\omega$  values. The stabilization was reported to

$\Omega_1$	$\epsilon_1$	$\Omega_2$	$\epsilon_2$
$\bar{\Omega}_1 + \epsilon_1 \cos \omega t$	$\epsilon_1$	$\bar{\Omega}_2$	$\epsilon_2$
$\bar{\Omega}_1$	$\epsilon_1$	$\bar{\Omega}_2 + \epsilon_2 \cos \omega t$	$\epsilon_2$
$\bar{\Omega}_1 + \epsilon \cos \omega t$	$\epsilon$	$\bar{\Omega}_2 + \epsilon \cos \omega t$	$\epsilon$
$\bar{\Omega}_1 + \epsilon \cos \omega t$	$\epsilon$	$\bar{\Omega}_2 - \epsilon \cos \omega t$	$-\epsilon$

Table 1: Table of inner ( $\Omega_1$ ) and outer ( $\Omega_2$ ) cylinder rotations considered by Carmi & Tustaniwskyj [1].

have a maximum at a dimensionless frequency of  $\omega \sim O(10)$ , that decreased for larger or smaller  $\omega$ . It was later shown that the criterion used to determine stability was somewhat arbitrary and lead to the qualitatively wrong result for a range of  $\omega$ . An article on modulated hydrodynamic by Homsy in 1974 [42] and a review of the subject by Davis [43] in 1976 called for more experimental results with improved dynamical range to guide the theoretical and numerical studies. Based on the interpretation confusion, Donnelly and coworkers decided to investigate the simplest example in a Taylor-Couette system where a single cylinder is periodically rotated about zero mean in an unbounded fluid. Predictions of Seminara & Hall (1976) indicated the flow would be destabilized, as was confirmed by Park, Barenghi, & Donnelly in 1980.

Carmi & Tustaniwskyj [1] published a pair of theory papers addressing stability in four realizations of modulated hydrodynamics in a Taylor-Couette flow apparatus. The four cases are shown in Table 2.2.1 where cylinder rotation rates and modulation amplitudes for the inner and outer cylinders are  $\Omega_1, \epsilon_1$  and  $\Omega_2, \epsilon_2$ , respectively. From their theoretical and numerical work Carmi & Tustaniwskyj concluded that flow would be stabilized by the first type of modulation (inner cylinder modulated, outer cylinder constant rotation) while all three of the other modulation forms should result in destabilization. Walsh & Donnelly reported experimental results in 1988 [44]

for the second system listed by Carmi & Tustaniwskyj. Their results were in qualitative disagreement with the predictions; modulation of the outer cylinder resulted in stabilization. Walsh & Donnelly also repeated the original modulated-rotation Taylor-Couette experiments [32, 33]. For modulation of the inner cylinder rotation rate about nonzero mean with the outer cylinder held fixed they found flow destabilization using standard stability criteria. Qualitative disagreement on the second case of Carmi & Tustaniwskyj encouraged a reexamination of the predictions. Wu & Swift [45] used the approach of Hall [46] to consider both cases experimentally investigated by Walsh & Donnelly. Results from Wu & Swift's theoretical and numerical work were in qualitative agreement with the experiments, although quantitatively there were large differences.

### **2.2.2 Thermally Modulated Rayleigh-Bénard Convection**

Use of thermally modulated Rayleigh-Bénard convection to study the influence of time-periodic modulation on hydrodynamics began with a paper published by Venezian in 1969 [34]. He was initially drawn to modulated Rayleigh-Bénard convection since, in the absence of modulation, the Taylor-Couette flow instability (under the assumptions of axisymmetric disturbances and a narrow annulus) was known to be mathematically analogous to the Rayleigh-Bénard convection instability [42, 43] while the latter case was easier to describe theoretically. He considered modulation arising from sinusoidal temperature variation at both the top and bottom plates or just the bottom bounding plate. Assuming a layer of infinite lateral extent Venezian found [34] large  $\omega$  ( $\omega \gg 1$ ) would have little effect on the onset of convection while a stabilization

would occur [ $R > R_c(\omega = 0)$ ] at smaller  $\omega$  [ $\omega \sim O(1)$ ]. He found maximum stabilization occurred in the limit  $\omega \rightarrow 0$ . The experiments of Donnelly, Reif and Suhl [32] and Donnelly [33] which Venezian hoped to better understand through the thermal analog [34] also indicated little effect from modulation at  $\omega \gg 1$  and increasing stabilization at lower  $\omega$ . However, the experiments found maximum stabilization at  $\omega \sim O(1)$  with evidence for destabilization as  $\omega \rightarrow 0$ .

Soon after Venezian's results were reported Rosenblat & Herbert [47] addressed the low frequency limit by developing criteria which took into account the fluid being laterally finite to predict the shift in onset. In qualitative agreement with experiments their results indicate maximum stabilization occurring at  $\omega \sim O(1)$ . The first experimental results on thermally modulated Rayleigh-Bénard convection were reported by Finucane & Kelly in 1976 [48]. In particular, they studied air and found qualitative agreement with the predictions of Rosenblat & Herbert as well as the original Taylor-Couette flow experiments. Finucane & Kelly reported destabilization ( $R < R_c$ ) for  $\omega \lesssim 3$  and stabilization ( $R > R_c$ ) for the largest  $\omega$  reported ( $\omega \approx 3.5$ ). Unfortunately, the definition of stability was the source of numerous qualitative disagreements and even resulted in both Homsy [42] and Davis [43] dedicating significant space to defining what stability for a modulated fluid means in their papers.

Thermal modulation was confirmed to shift the onset of fluid motion. Niemela & Donnelly [49] used the short response times of liquid Helium I coupled with heating and cooling of both top and bottom plates to extend the dynamical range of thermally modulated experiments. Their experimental findings confirmed the predictions of Rosenblat & Herbert [47]. For  $Pr = 0.49$  experiments found maximum stabilization occurring at  $\omega \approx 10$  while Rosenblat & Herbert's predictions indicated maximum

stabilization at  $\omega \approx 7$ . However, they did not have much data at the larger frequencies and agreement was mostly qualitative.

Additionally, thermal modulation has been predicted and confirmed to change the planform at onset. Using a perturbation approach Roppo, Davis, & Rosenblat [36] concluded modulation of a bounding plate temperature changes the bifurcation at onset from supercritical (forward) to subcritical (backwards). In a forward bifurcation the onset planform is parallel stripes whose amplitude grows continuously from zero. Alternatively, the stable onset planform for the backwards bifurcation is hexagons (see Sec. 1.1.1), whose amplitudes show a discontinuous jump at onset and display hysteresis. The mechanism for the formation of hexagons is resonant triads (see Sec. 1.1.3). In the case of thermal modulation the Boussinesq symmetry is broken by a nonlinear conduction profile. Based on these observations, Roppo, Davis, & Rosenblat predicted hexagons would be stable over an experimentally observable range of  $R$  at onset. Soon after Ahlers, Hohenberg, & Lücke [38] reported experimental results for thermally modulated Rayleigh-Bénard which failed to observe the predicted hexagons. Ahlers, Hohenberg, & Lücke concluded side wall influence might be masking the predicted onset of hexagons. Hohenberg & Swift [37] applied a Lorenz-type model to extend the perturbation results [36] to a wider parameter range. From the Lorenz model Hohenberg & Swift showed that Roppo, Davis, & Rosenblat had vastly overestimated (by a factor of  $\approx 100$ ) the range of observable hexagons. Hohenberg & Swift concluded that the bifurcation structure would not be experimentally observable, but with careful selection if the physical parameters hexagons might be found. Experiments reported by Meyer, Cannell, & Ahlers [39] qualitatively agreed with both the theoretical predictions [36, 37] and quantitatively with those of Hohenberg

& Swift. Additionally, over a range of parameters where stripes and hexagons were expected to be simultaneously stable experiments indicated hexagons and stripes existed in mixed states. This was an unexpected result since the stripes and hexagons were not separated into distinct domains. Theoretical descriptions always assumed either stripes or hexagons, not both in mixed domains.

Even with the improved  $\omega$  range achieved by Niemela & Donnelly [49] thermally modulated experimental studies are constrained to a relatively narrow parameter range as were the rotation modulated Taylor-Couette flow experiments. Due to these limitations previous modulated hydrodynamic experiments have been prevented from finding fluid motion at twice the drive frequency or investigating the region of pattern formation away from onset.

### 2.2.3 Acceleration Modulated Rayleigh-Bénard Convection

Instead of thermal modulations to achieve a time dependent buoyancy force the acceleration may be modulated by vertical oscillations of the fluid layer. In generalizing the simple pendulum (Sec. 2.1) to allow for base oscillations it was convenient to simply consider gravity to be modulated. A similar approach may be used to write the equations of motion for thermal convection with time dependent acceleration [ $g \rightarrow g(t) = g_{stat} + a \cos(\omega t)$ ],

$$\begin{aligned} \nabla \cdot \mathbf{v} &= 0 \\ \nabla^2 \mathbf{v} + \hat{\mathbf{z}}(1 + \epsilon \cos \omega t)\Theta - \nabla P &= \frac{1}{Pr}(\mathbf{v} \cdot \nabla \mathbf{v} + \frac{\partial \mathbf{v}}{\partial t}) \\ \nabla^2 \Theta + R\hat{\mathbf{z}} \cdot \mathbf{v} &= \mathbf{v} \cdot \nabla \Theta + \frac{\partial \Theta}{\partial t}. \end{aligned} \tag{13}$$

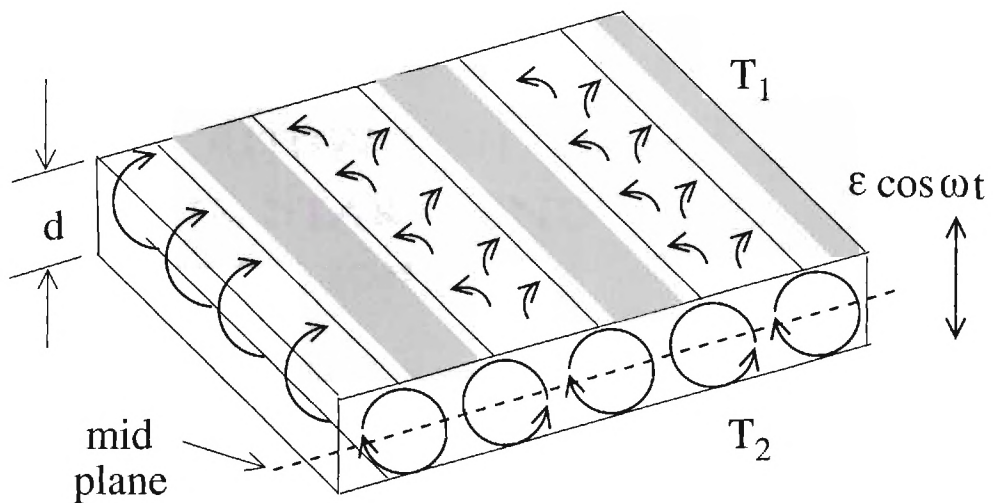


Figure 6: Sketch of stripes in a fluid layer driven out of equilibrium by both an imposed temperature difference and parametric oscillations. Temperature difference is defined in terms of the uniform top plate temperature  $T_1$  and uniform bottom plate temperature  $T_2$  ( $T_2 > T_1$ ) by  $\Delta T = T_2 - T_1$ . Periodic oscillations are defined by a dimensionless acceleration  $\epsilon$  and a dimensionless angular frequency  $\omega$  through the driving  $\epsilon \cos \omega t$ . The fluid layer depth is given by  $d$ . Shaded lines represent stripes that would be observed when viewing a parallel roll state by a shadowgraph from above.

These equations are valid in the Boussinesq approximation and have four dimensionless parameters:  $R$ ,  $Pr$ ,  $\epsilon$  and  $\omega$ . Recall from Sec. 1.1.1, the Rayleigh number  $R$  and the Prandtl number  $Pr$  are sufficient to describe the state of a fluid in the absence of modulation. The additional modulation parameters are dimensionless acceleration  $\epsilon$  and dimensionless modulation frequency  $\omega$ . In describing the state of the system it is convenient to replace  $\epsilon$  by a dimensionless displacement amplitude,  $\delta Fr = \frac{\epsilon}{\omega^2}$ . In terms of experimentally measurable quantities the state of the fluid with modulated acceleration may be described by:

$$R = \frac{\alpha d^3 \Delta T g_{stat}}{\nu \kappa}, \quad Pr = \frac{\nu}{\kappa},$$

$$\delta Fr = \frac{\kappa^2}{d^4 g_{stat}} \delta', \quad \text{and} \quad \omega = \frac{d^2}{\kappa} \omega'. \quad (14)$$

These definitions are written in terms of dimensional displacement amplitude  $\delta'$  (cm), dimensional oscillation angular frequency  $\omega'$  (Hz), fluid layer depth  $d$  (cm), imposed temperature difference  $\Delta T$  ( $^{\circ}\text{C}$ ), kinematic viscosity  $\nu$ , thermal diffusivity  $\kappa$ , thermal expansivity  $\alpha$ , and the constant gravitational component  $g_{stat}$ .

Theoretical and numerical results indicate acceleration modulation with heating from below stabilizes the conductive state over the majority of parameters. If the top bounding surface of the fluid is warmer than the bottom (heating from above) an analogy may be made to the hanging pendulum while if the bottom is warmer than the top (heating from below) an analogy to the inverted pendulum is appropriate. Using these analogies Gresho & Sani reported the first investigation of acceleration modulated Rayleigh-Bénard convection in 1970 [35] for both heating from above and below. They solved a form of the Mathieu equation to examine convective onset. A similar equation was used in another comprehensive study by Ahlers, Hohenberg,

& Lücke in 1985 [50], though they derived the equation from a Lorenz model mode truncation of the appropriate Boussinesq equations [Eqs. (13)]. The current discussion will be limited to the case of heating from below (numerical results for the case of heating from above can be found in the Ph.D. dissertation of Oliver Brausch [28]. Beginning from  $\omega = 0$ , Gresho & Sani reported changes in conduction stability for increasing  $\omega$  at constant  $\delta Fr$ . Increasing  $\omega$  from  $\omega = 0$  initially results in stabilization of conduction ( $R_c > 1708$ ). As  $\omega$  increases conduction is initially increasingly stabilized. At sufficiently large  $\omega$  another instability precedes the previous one and a maximum in conduction stability will occur. For further increases in  $\omega$  stabilization will begin to decrease due to this second instability. Corresponding conduction stabilization can reach several times the unmodulated  $R_c$ .

The types of predicted flows display different spatial and temporal characteristics. Three possible types of fluid motion were predicted: harmonic, subharmonic, and relaxation oscillations. Harmonic flow is the first instability at smaller modulation parameters and is expected to display time dependence synchronous with the drive frequency  $\omega$ . In harmonic flow the velocity field would briefly reverse, although on average the fluid would overturn. The heat transport was predicted to be diminished for harmonic convection in comparison with the unmodulated case ( $\omega = 0$ ). Harmonic motion is expected at lower values of  $\delta Fr$  and  $\omega$ . Increasing  $\delta Fr$  or  $\omega$  from the unmodulated case conduction was found to be increasingly stabilized over the harmonic parameter range. The corresponding wave numbers at harmonic onset are relatively insensitive to  $\delta Fr$  and  $\omega$ , except as the onset of subharmonic flows is approached. As these parameters are increased conduction eventually loses stability to fluid motion displaying subharmonic response, this is the second instability which

precedes the harmonic instability at larger modulation parameters and the flow is then expected to be periodic at  $2\tau$ . Over a drive cycle subharmonic velocity fields reverse about zero mean; there is no net motion of the fluid. Correspondingly the heat transport of subharmonic flows is dramatically reduced in comparison with the  $\omega = 0$  case. Wave numbers of subharmonic states are strongly dependent on the modulation parameters ( $\delta Fr$  and  $\omega$ ). Based on the significant difference between harmonic and subharmonic wave numbers Gresho & Sani argued that there would be an abrupt change as the system passed from harmonic to subharmonic fluid motion. The third type of temporal response is relaxation oscillations. These were predicted to occur beyond the subharmonic region at relatively very large  $\delta Fr$  and  $\omega$ . Temporal response of the relaxation oscillations was predicted to be on the  $O(10\omega)$ , displaying explosive bursts.

The results of Gresho & Sani were qualitatively confirmed by Biringen & Peltier in 1990 [51] who included three spatial dimensions in a numerical study. Clever, Schubert, & Busse [52, 53] also reported numerical solutions of the Oberbeck-Boussinesq [Eqs. (13)] in qualitative agreement with the other investigations. Clever, Schubert, & Busse extended the considered parameter range to include  $1 \times 10^{-7} \leq \delta Fr \leq 1$ ,  $100 \leq \omega \leq 3000$  and  $0.71 \leq Pr \leq 50$ . Gresho & Sani considered only  $Pr = 7$ , while Biringen & Peltier reported results for  $Pr = 0.71$  and  $Pr = 7.1$ . Prandtl numbers for some common fluids are:  $Pr = 0.71$  (air),  $Pr = 0.93$  (compressed Carbon-Dioxide),  $Pr = 7$  (water), and  $Pr \approx 50$  (Silicon oil). The constant component of the effective gravitational acceleration was shown by Biringen and Peltier not to qualitatively alter the stability results. Considering the one- $g$  and zero- $g$  cases they found general qualitative agreement and quantitative agreement at large modulation amplitudes.

The various theoretical and numerical studies [35, 50, 51, 52, 53] of acceleration modulated Rayleigh-Bénard convection make several consistent predictions. First, moving away from the unmodulated limit conduction is expected to be stabilized with increasing  $\delta Fr$  and  $\omega$ , this stabilization may be significant. Second, conduction will lose stability to convection displaying harmonic time dependence and patterns of a characteristic wave number ( $q_c^H$ ) over a range of  $\delta Fr$  and  $\omega$ . For large enough values of  $\delta Fr$  and  $\omega$  the degree of stabilization a subharmonic instability will precede the harmonic instability and  $R_c$  will begin to decrease with increasing modulation parameters. Conduction will now lose stability to convection displaying a subharmonic time dependence forming patterns of a distinct characteristic wave number  $q_c^S$  that is larger than the harmonic,  $q_c^S > q_c^H$ . While Gresho & Sani predicted  $q_c^S$  was independent of the modulation parameters the more detailed analysis of Clever, Schubert, & Busse found  $q_c^S$  was sensitively dependent on  $\omega$ . The dependence of  $q_c^S$  on the modulations parameters was not reported by Biringen & Peltier.

Physical limitations associated with the standard fluids for investigating Rayleigh-Bénard convection have excluded any experimental verifications of the various predictions. To confirm the predictions requires sufficient dynamical range to reach the interesting parameters and a reliable means of measurement. The feasibility of performing successful modulated-acceleration experiments is extremely sensitive to the fluid used. Two commonly used fluids are water and Silicon oil. For both of these  $Fr \sim O(1 \times 10^{-9})$  with typical fluid layer depths  $d \sim O(1)$  cm. In order to reach subharmonic convection at  $\omega = 1000$  Gresho & Sani [35] predicted  $\delta Fr \sim 10^{-5}$  and  $R \sim O(10^4)$  would be required. Eqs. (14) indicate this would require  $f' \sim O(1)$  Hz

and  $\delta' \sim O(10^4)$  cm. The prohibitively large  $\delta'$  is the reason for a lack of experimental verification of the various predictions for acceleration modulated Rayleigh-Bénard convection.

As discussed in Chapter 1 compressed gas convection has been refined over the past ten years. Shadowgraphy provides a reliable qualitative and quantitative visualization technique for compressed gases. A commonly used gas like  $\text{CO}_2$  under 34 bar has  $Fr \sim O(1 \times 10^{-5})$  and  $Pr \sim O(1)$ . To reach subharmonic convection at  $\omega = 100$  requires dimensionless displacement magnitudes of  $\delta Fr \sim 4 \times 10^{-4}$ . Compressed gas convection typically occurs in very thin layers where  $d \sim O(6 \times 10^{-2})$  cm. Inverting Eqs. (14) reveals that reaching subharmonic convection in compressed  $\text{CO}_2$  would require  $f' \sim O(10)$  Hz and  $\delta' \sim O(1)$  cm, both of which are attainable in the laboratory. Thereby, using compressed gases it should be possible to experimentally investigate many of the predictions made for acceleration modulated Rayleigh-Bénard convection including stabilization, the existence of harmonic and subharmonic convection as well as the transition between harmonic and subharmonic flows.

# CHAPTER 3

## Laboratory

To experimentally investigate acceleration modulated Rayleigh-Bénard problem a convection cell is attached to a mechanical shaking device. Design of the convection cell is based on the one described by de Bruyn *et al.* [54], but shares features with the original apparatus for compressed gas convection investigated by Croquette [55]. Vertically oscillating the convection cell with a hydraulic shaker produces the time dependent acceleration in the frame of the fluid layer. This apparatus may be thought of as a hybrid of two standard devices in pattern formation studies: Rayleigh-Bénard convection and Faraday waves, although there is no free fluid surface. Studies with both of these devices have produced a substantial body of literature and lead to numerous design refinements that enable us to rapidly and effectively construct our apparatus. Our experiment will be described in terms of four subsystems: a convection cell, a shaking device, pattern visualization and computer control of experimental conditions as well as data acquisition/analysis. An overview of the complete device is shown schematically in Fig. 7.

Numerical solutions of the Oberbeck-Boussinesq equations [Eqs. (13)] are used to verify and augment the experimental results. A pseudo-spectral method is employed [56, 28] in solving Eqs. (13). The numerical code used in these solutions is generalized

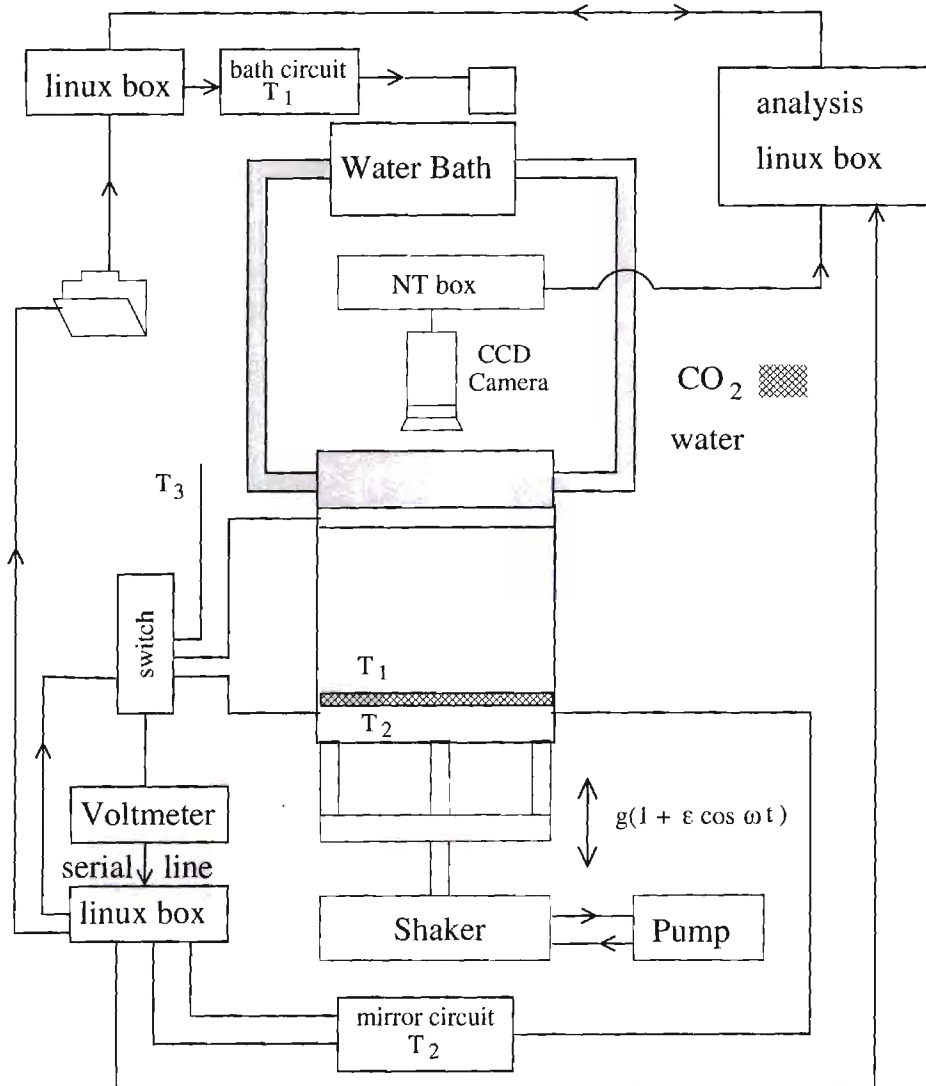


Figure 7: Overview of the experimental configuration.

from one developed and extensively tested on classical (unshaken) Rayleigh-Bénard convection.

### 3.1 Convection Cell

Design of the convection cell [Fig. 8] attempts to balance apparatus simplicity and reliability under vertical oscillations with lateral size of the cell. In the convection cell configuration employed here cooling water removes heat from the experiment by passing from an external water bath over the pressure vessel lid which has an inner diameter below which is the upper surface of a 2.54 cm thick sapphire crystal. The crystal acts as a window into the cell with the upper surface exposed to water at 1 bar while the lower surface is in contact with the fluid at pressures between 30 bar and 35 bar. The lower sapphire surface is the top plate of the convection cell. For uniformity the top plate needs to be flat and crystal deformations due to large pressure differentials or aspect ratios limit our investigations to pressures  $P \lesssim 50$  bar and  $\Gamma \lesssim 50$ . Lateral boundaries for the cell are provided by a cylindrical stack of filter paper typically of 3.8 cm inner diameter and 5.5 cm outer diameter, although the outer diameter may be varied to alter the sidewall influence. These side-walls rest on the gold-coated face of a cylindrical aluminum block 0.6 cm thick and 5.08 cm in diameter (Fig. 9). It provides a reflective surface (mirror) for the imaging technique and the bottom surface of the cell. Attached to the bottom of the aluminum block is a resistive heating pad for warming the bottom plate and the principal source of temperature control.

This convection cell sits in a cylindrical aluminum can 6.75 cm high, 6.93 cm inner

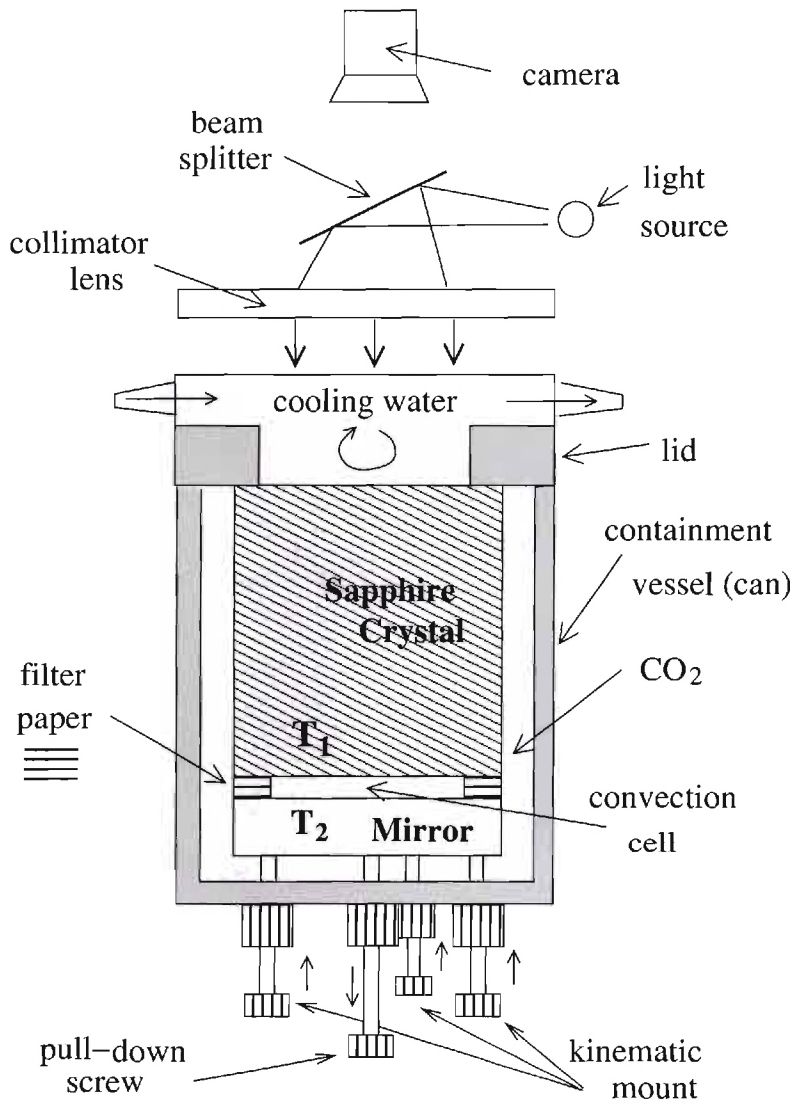


Figure 8: Schematic of the compressed gas convection cell.

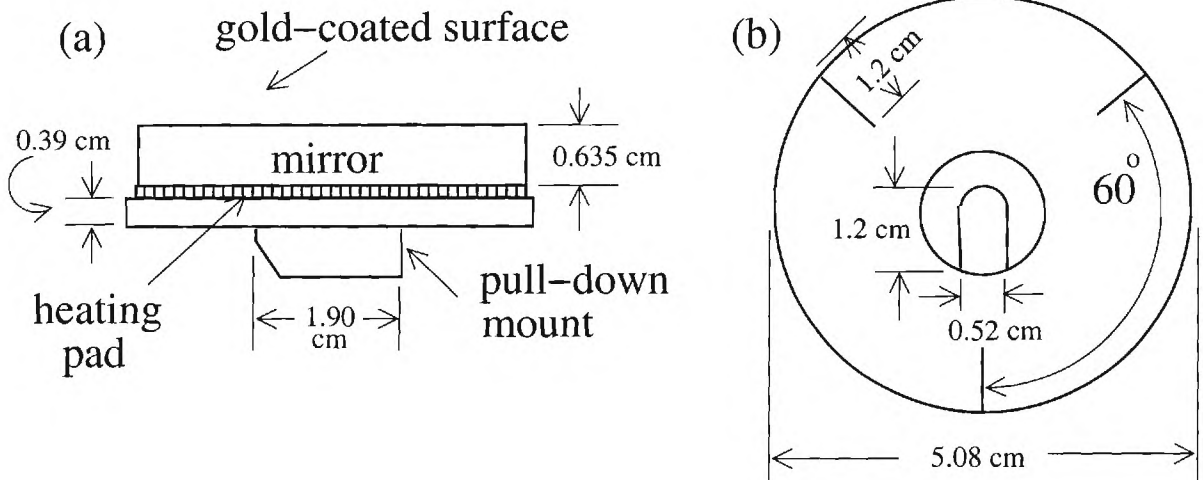


Figure 9: Aluminum mirror that acts as the bottom surface of the convection cell (see SIDE view).

diameter and 8.95 cm outer diameter. A 1.016 cm thick, 8.95 cm in outer diameter, 4.11 cm inner diameter cylindrical aluminum plate serves as the upper lid of the pressurized vessel [Fig. 10]. Four Newport 1/4-80 Fine Adjustment Screws (AJS-2) with NPT pressure fittings pass through the bottom of the can, acting as a kinetic mirror mount. Three of the screws are arranged in a centered equilateral triangle of 11.43 cm side length serving as kinematic points used to level the mirror with respect to the bottom crystal surface, while the fourth screw passes through the center and pulls down on the mirror against the kinematic mount to ensure the mirror does not move when the apparatus is oscillated. Pressure seals for the four screws use Viton O-rings to avoid  $\text{CO}_2$  penetration of the O-rings would result in a loss of effective seal as bubbles in the O-ring would form. Under pressure the sapphire crystal presses against a size 031 Viton V-75 O-ring seated in the bottom of the upper retaining plate. The plate is attached by 8 evenly spaced pairs of 1.5 cm-long, 4-40 hex-ended

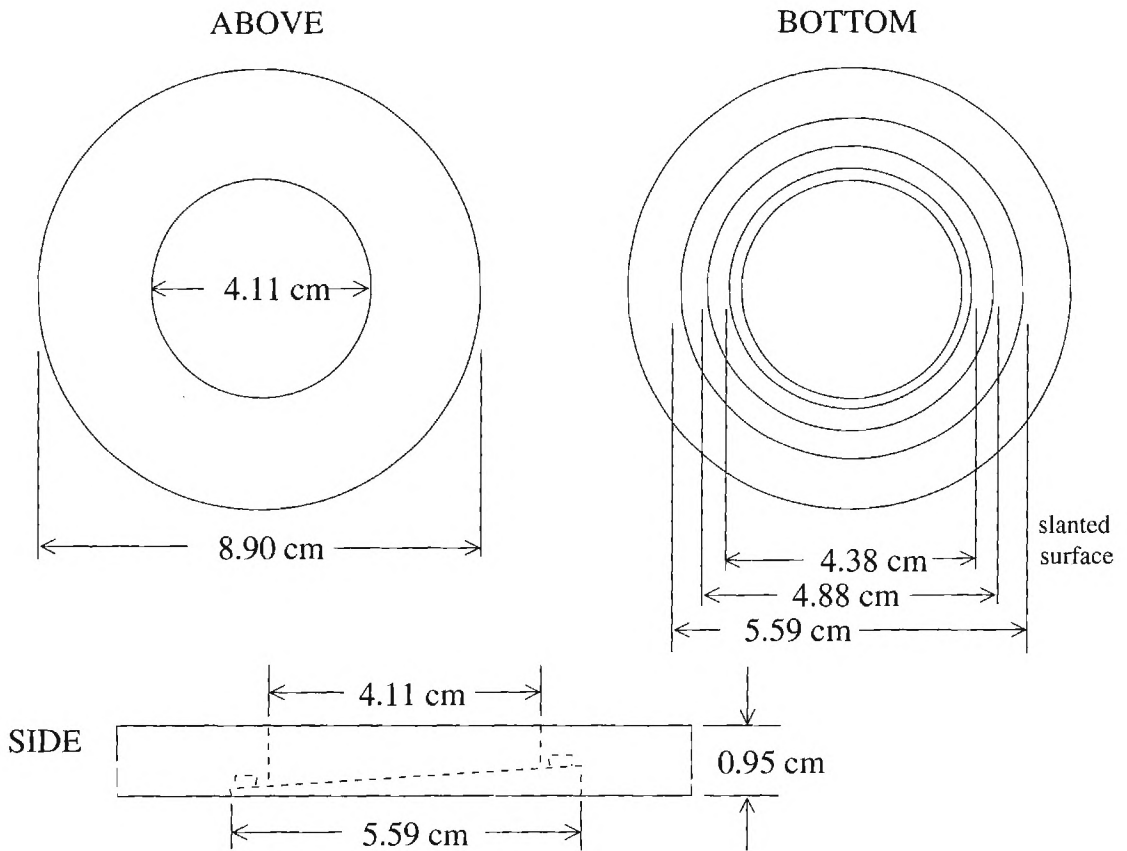


Figure 10: Dimensions of the pressure vessel top retaining plate. Upper surface of the sapphire crystal is slanted and must be aligned to seat into the top plate.

screws 1.5 cm apart. A size 040 Buna N-70 O-ring is seated in the upper plate. Dow Corning high vacuum grease is applied to both of these seals and all of the screws are replaced each time the can is opened.

There are four NPT pressure fittings passing through the can side. The two lower fittings are used for sensing and controlling the temperature of the mirror and will be covered in the control section. The two upper fittings are used to fill the vessel with 99.99% pure CO<sub>2</sub> from a pressurized reservoir tank. A Victor model SR 4F compressed gas regulator attached to the tank allows the external pressure to be

roughly set and the pressure vessel to be gradually filled. As CO<sub>2</sub> fills the can it seeps through the porous filter paper to fill the convection cell.

## 3.2 Vertical Oscillations

Two separate vertical oscillation configurations are employed in attaining the results detailed in this dissertation. Both set-ups employ the same hydraulic pump to supply the mechanical shaking devices with pressurized hydraulic fluid. The pump circulates Premium Antiwear 46 weight hydraulic fluid at 1700 PSI. Team Vibration Testing Equipment manufactured the mechanical shaking devices (shakers). These shakers use a servo valve to regulate the hydraulic pressure and thereby mechanically displace a driving rod. The rod is coupled to the convection cell bottom, supplying the vertical oscillations and time dependent acceleration in the frame of the fluid layer. Restrictions on the attainable accelerations are imposed by the maximum hydraulic pressure through the cross-sectional surface area of the driving rod and the mass of the convection cell. To maintain maximal acceleration range it is necessary to restrict convection cell mass as well as minimize cross-sectional driving rod area. The bulk of these results are attained with the first mechanical shaker (Fig. 11). Maximum displacement for this configuration is  $\delta' \approx 2$  cm. Recoil damping is provided by a stack of Lead coated plywood sheets which rest on four radial F/FR13 truck tire tubes. The shaker is mounted directly to the plywood sheets by four bolts which pass through the stack. Towards each of the four corners of the plywood stack an additional bolt is tightened to further secure the sheets and reduce spurious vibrations. The range of accessible frequencies is  $0 \leq \omega' \lesssim 20$  Hz. Due to the response

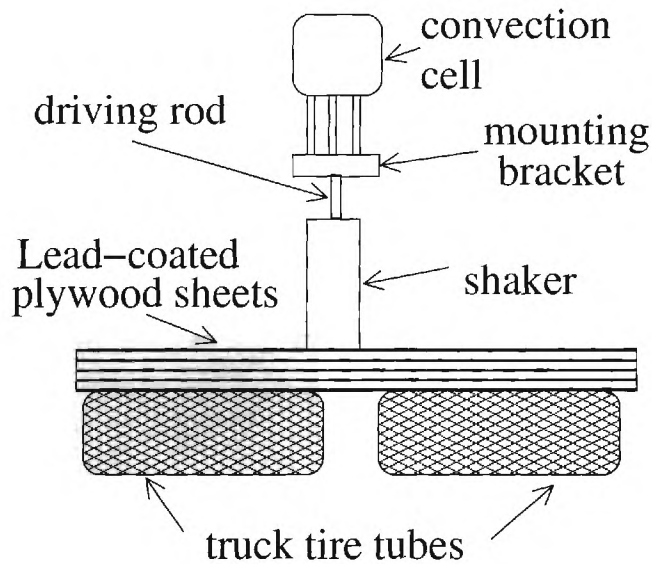


Figure 11: Sketch of the first mechanical shaking device.

of the servo valve this shaker is limited to sinusoidal oscillations. Attached directly to the drive rod is an aluminum mounting bracket [Fig. 12]. Three hex-bolts attach 1.27 cm diameter 11.43 cm long circular legs to the mounting bracket. The legs are attached to the bottom of the convection cell pressurized can allowing access to the leveling screws. The circular drive rod may rotate and displays lateral vibrations of  $\pm(1\% - 2\%)$  at typical displacement amplitudes ( $\delta'$ ), both of which lead to spurious experimental effects that the construction of the second oscillation configuration is designed to address.

The second experimental shaking configuration (Fig. 13) has the advantages of increased stroke, improved response to driving waveform, elimination of drive shaft rotations and reduction of the lateral accelerations due to vibrations. Maximum stroke with the second mechanical shaker is 15.25 cm. In this case the shaker is bolted to an aluminum plate and the bottom of an open-ended bulk container (box)

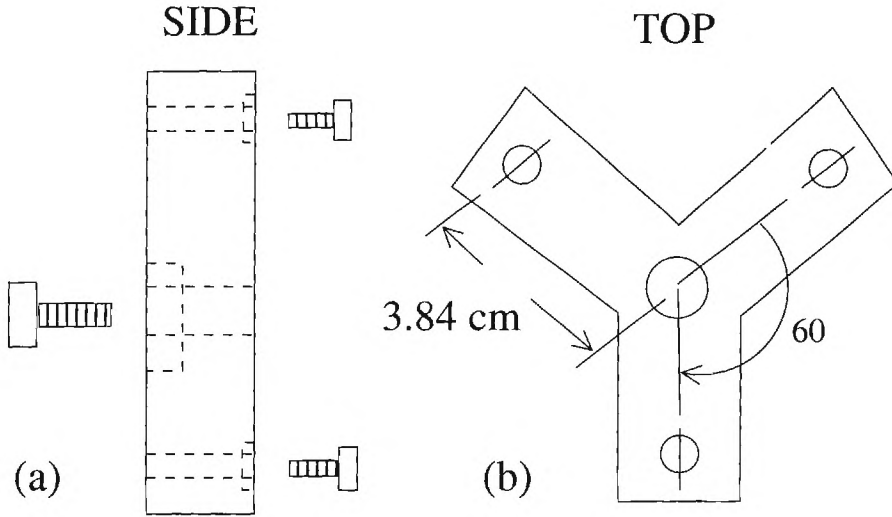


Figure 12: First shaker mounting bracket connecting the convection cell to the driving rod. View from the side (a) and from above (b).

constructed of 12 and 13 gauge steel. The box is filled with  $\approx 1050$  lbs. of sand for ballast and rests on 96 tennis balls for vibration damping. Instead of connecting the drive rod directly to the convection cell mounting bracket as in the first configuration, the drive rod in the second set-up is attached to a rectangular slide [Fig. 13] which passes through an air-bearing. A connecting rod with an embedded bearing (Fig. 14) mounts the drive rod to the rectangular slide and allows for slight misalignments between the two rods.

NewWay Bearings supplied the air-bearing and slide that prevents the drive rod from rotating and reduces the lateral vibrations dramatically. Pressurized air for the bearing comes from the building supply which passes through two Whatman-Balston Air Products air and moisture filters. The grade DX first filter and grade BX second filter together remove 99.99% of particles and mist from the air stream to protect the air bearing which is sensitive to water and oil. A regulator attached downstream of

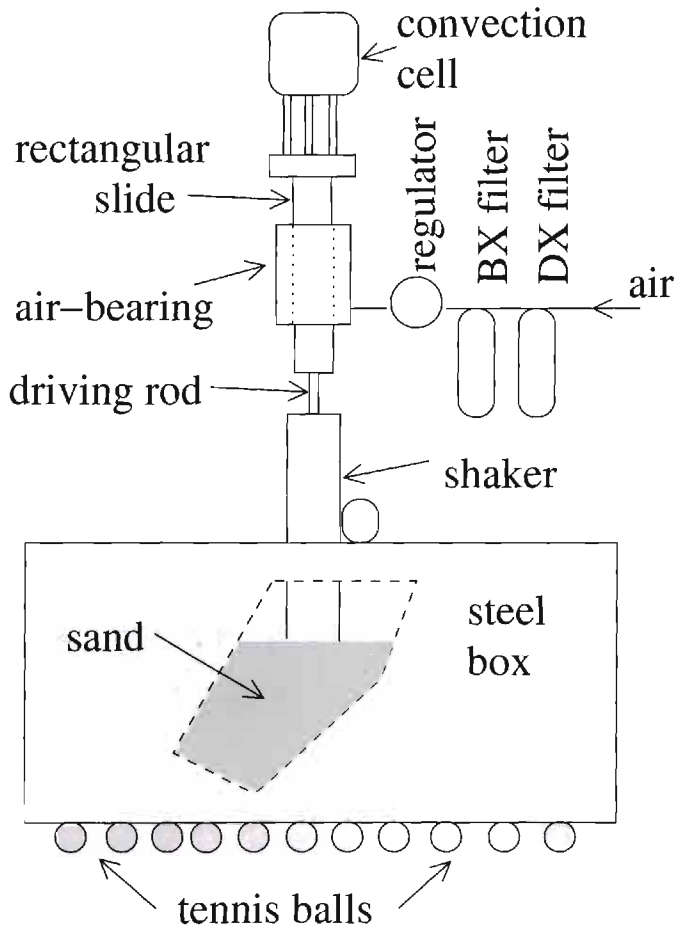


Figure 13: Sketch of the second mechanical shaking device. This shaker has improved dynamical range over the first configuration and employs a rectangular slide on the driving rod to eliminate driving rod rotations and reduce lateral vibrations.

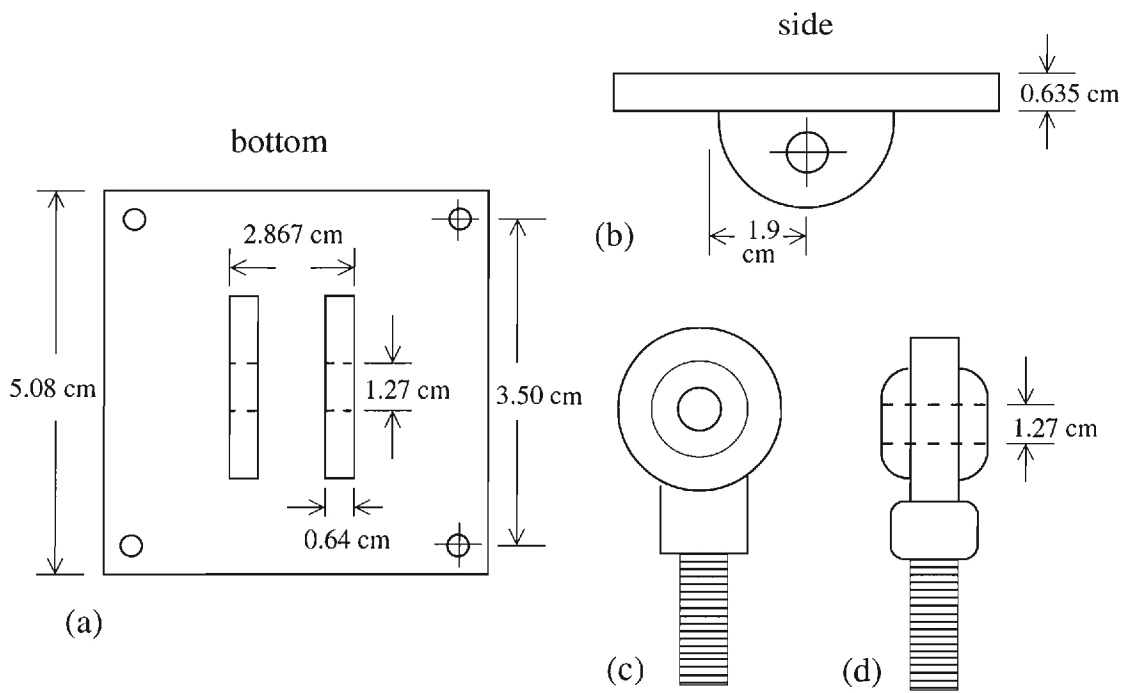


Figure 14: Second shaker mounting bracket connecting the driving rod to the rectangular slide and the swivel bearing used.

the second filter restricts the wall pressure to the 60 PSI called for in the bearing specification. A 1/16 in. clear Swaglock tube connects the filters to the bearing.

Aligning the air-bearing relative to the vertical axis and isolating it from external vibrations are addressed by the mounting apparatus shown in Fig. 15. The air-bearing rests on a alignment plate suspended from three springs. A triangular mount allows leveling of the plate and bearing relative to the vertical axis by adjustment of three screws. While these mounting points in principle allow vibrations to be transmitted to the leveling plate, the springs damp out some of these vibrations and in practice the transmitted effects are minimal and do not seem to have any significant effect on the experiment.

### 3.3 Imaging Convection

Fluid flows are imaged using the technique of shadowgraphy [Fig. 16]. This well-established [54, 57] imaging method is particularly attractive since it relies only on variations in the index of refraction to visualize the fluids temperature field. Light from a point source is reflected by a beam splitter through a collimator lens. The now parallel light passes through the convection cell sapphire window and fluid layer to be reflected by the gold-plated surface of the aluminum mirror. In turn, this light passes back through the sapphire crystal and collimator lens, past the beam splitter, through the camera lens and is incident on the CCD array. Shadowgraphy takes advantage of the fluid's index of refraction temperature dependence which causes the fluid temperature variations to act as lenses. The index of refraction is lower for warmer fluid causing upflowing columns to have lower indexes of refraction while

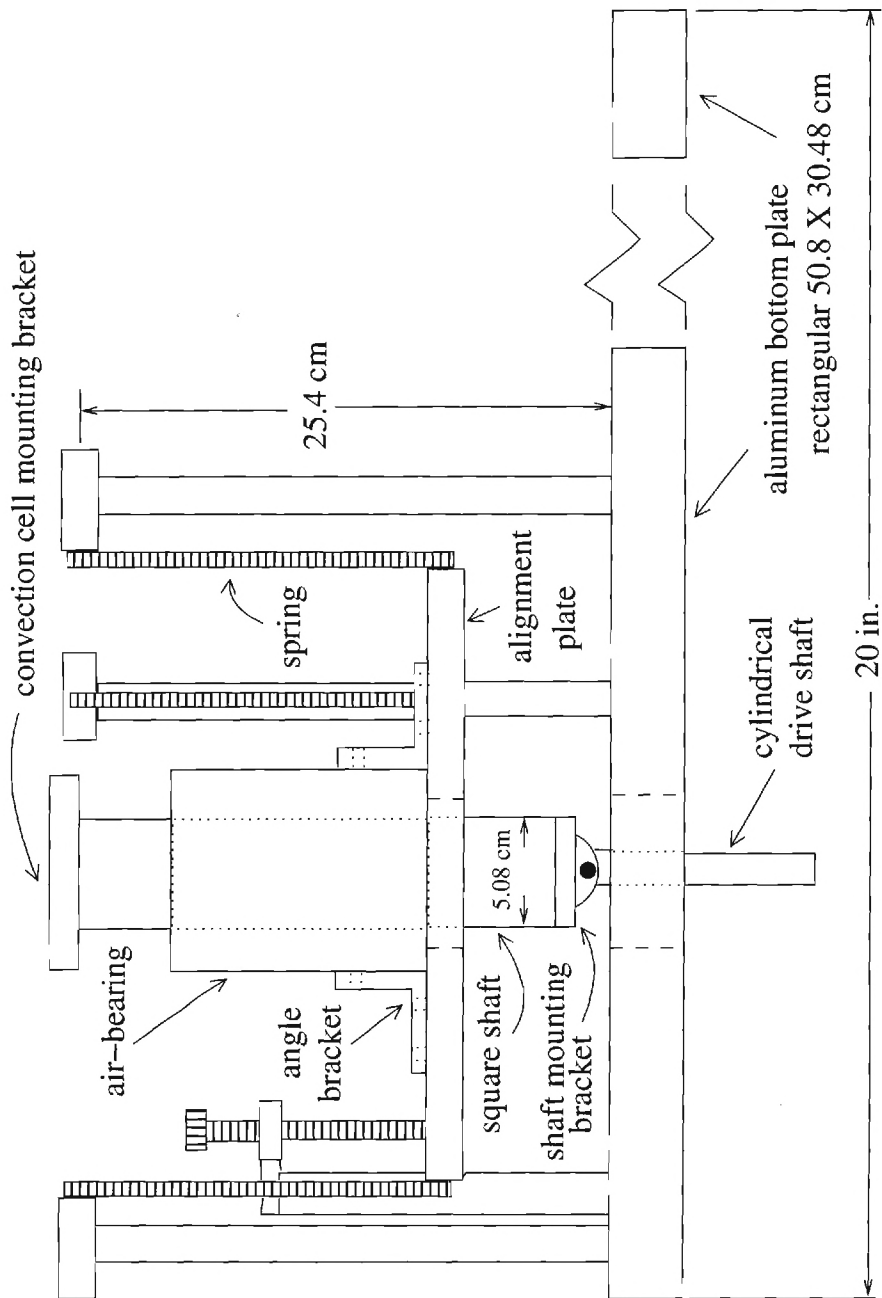


Figure 15: Alignment table for the square air-bearing which is attached to the alignment plate by angle brackets and suspended by springs. The springs act as vibration damping.

downflowing columns have higher indexes. These variations translate into light being focused towards regions of higher index of refraction, cooler downflowing columns. By varying the camera lens imaging plane relative to the focal plane [Fig. 16] the light and dark areas may be switched. For the patterns reported in this dissertation light areas correspond to cold columns and downflows while dark areas correspond to upflows. Using compressed gases greatly enhances the sensitivity of the shadowgraph [55] since the refractive index is reinforced and the contrast is enhanced due to the very thin layers which may be used. Shadowgraph contrast is proportional to the second spatial derivative. For the current purposes this qualitative geometric optics description is sufficient, although it should be mentioned that by including physical optics this method may be made quantitative [54].

Optical components used in producing the shadowgraph are commonly available. Illumination comes from a 30 watt Quartz Halogen source through a 4.8 mm diameter fiber optic which yields approximately 4000 foot candles at 15.25 cm. A Melles Griot beam splitter redirects source light through a collimator lens. Since the collimator lens has a 50 cm focal length the point light source is positioned at the focal distance from the collimator lens mid-plane. A Sonic XC77 CCD Camera Module with an appropriate 35 mm lens attached records the shadowgraph. Images are acquired by shuttering the camera to ensure the flow is visualized at the same phase of the drive.

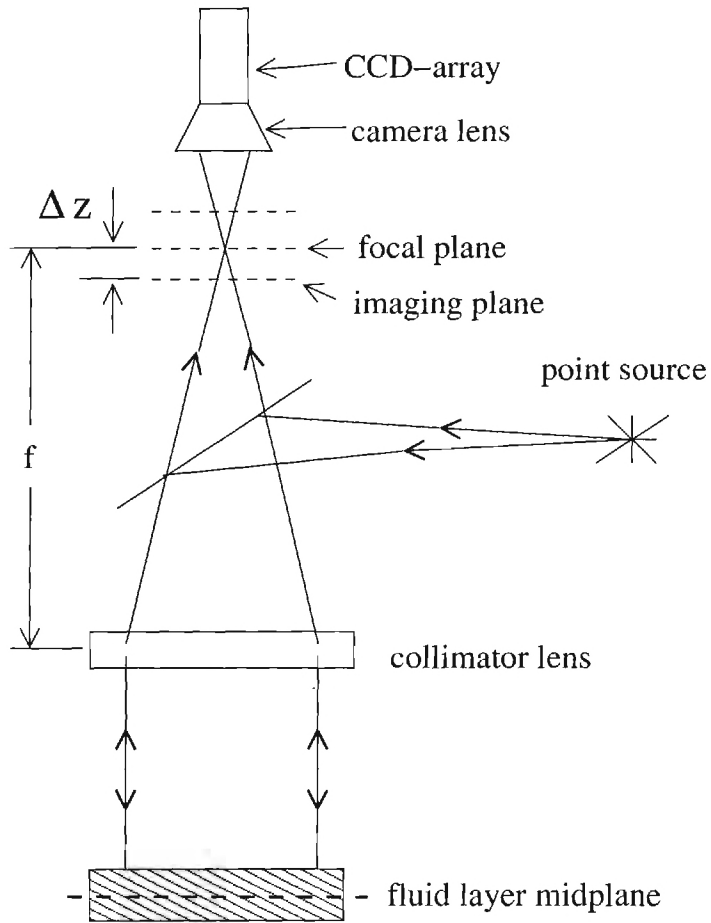


Figure 16: Schematic of the shadowgraph configuration. The collimator lens has a focal length  $f$ . The camera lens is focused on the imaging plane, a distance  $\Delta z$  further from camera than the focal plane. Shades in the presented experimental images could be reversed by changing the imaging plane to a distance  $-\Delta z$ ; closer to the camera than the focal plane.

## 3.4 Computer Control

Computers are used to measure and regulate experimental quantities, to record images, dynamically analyze results and autonomously search the dimensionless parameter space. The important physical quantities of  $T_1$ ,  $T_2$  and pressure were dynamically controlled using linear Proportional-Integral-Derivative (PID) control algorithms. These were implemented on surplused 386 and 486 computers utilizing National Instrument LabPC+ data acquisition boards and a series of analog circuits. Computer code to record images as detailed in the previous section was written in C by Todd Meyrath and controlled by Linux shell scripts written to automate the experiment. Analysis of the images was performed by a series of functions written in the MatLab environment and dynamically called from the controlling shell scripts. Based on the results from the analysis and predefined conditions the controlling bash scripts would change physical quantities of the experiment, record data and again start analysis.

### 3.4.1 Temperature

The two most important temperatures to stabilizing the experiment are the mid-plane fluid temperature  $\bar{T}$  and  $\Delta T$ . All four of the system parameters ( $\delta Fr$ ,  $\omega$ ,  $R$  and  $Pr$ ) depend on these two temperatures. The Rayleigh number is linearly proportional to the temperature difference,  $R \sim \Delta T$ , while all of the parameters depend on  $\bar{T}$  through  $\nu$ ,  $\kappa$  and  $\alpha$ . Both  $\Delta T$  and  $\bar{T}$  are defined in terms of  $T_1$  and  $T_2$ :  $\Delta T = T_2 - T_1$  and  $\bar{T} = (T_1 + T_2)/2$ . Since the sapphire crystal is in contact with a water bath changes in  $T_1$  occur on a long time scale while  $T_2$  may change on a much shorter scale. Due

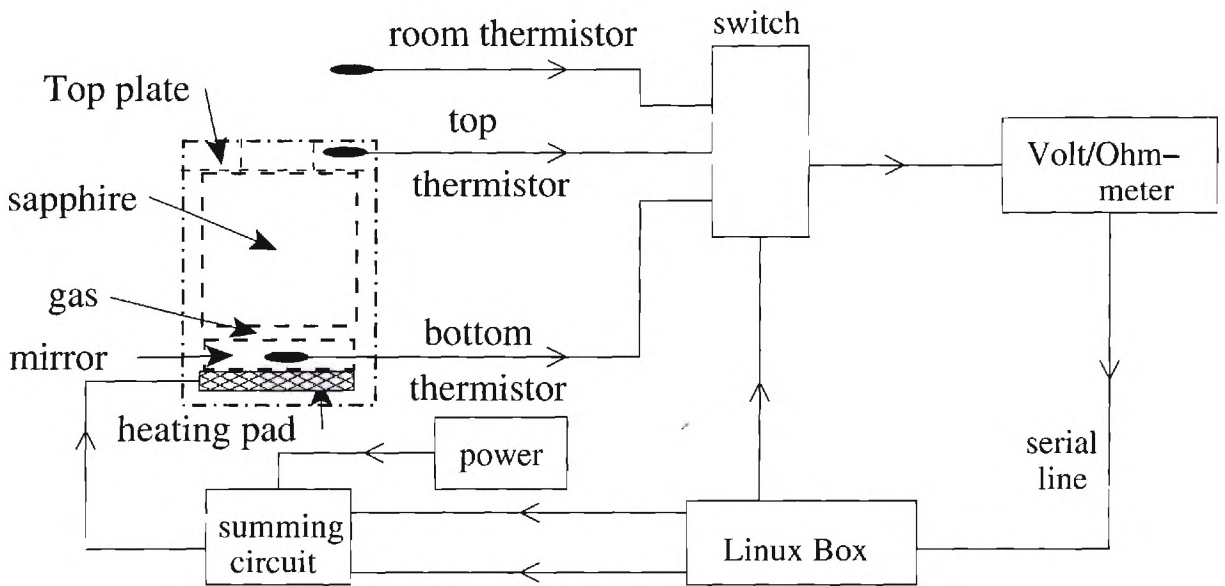


Figure 17: Overview of the temperature control system which controls both  $\Delta T$  and  $\bar{T}$  using linear PID algorithms.

to this separation of response scales  $\Delta T$  is controlled primarily by changing  $T_2$  while the water bath is used to more slowly regulate  $T_1$  and hence control  $\bar{T}$ . Temperatures are measured by recording the resistance in  $100\text{ K}\Omega$  thermistors and then converting the measured resistance to temperature by matching calibration curves. The top thermistor is located in a hole on the side of the top retaining plate while the bottom one is placed in the bulk of the mirror. Heat sink compound is used in both cases to maintain thermal contact between the thermistors and the surrounding material.

The temperature control system is shown schematically in Fig. 17. A National Instruments LabPC+ data acquisition board installed in a 386 computer running Linux (Slackware - kernel 2.0.28) controls  $\Delta T$  by  $T_2$ . The control algorithm uses outer and inner control loops to enhance speed, which turns out to be crucial to

maintaining reasonable temperature control. One step in the outer control loop begins with `T_ctrl.c` opening the switch connected to the top thermistor. The control program then instructs the multi-meter to take a resistance reading and opens the computer's serial line where the multi-meter is attached. After reading the serial line the computer closes the line and opens all switches. The measured resistance ( $R_1$ ) is then converted to the top plate temperature ( $T_1$ ) by matching to a calibration curve. Now that  $T_1$  is known the inner control loop begins with the closing of the switch to the bottom plate temperature. Using the same process as described for the top thermistor the bottom temperature is calculated after which all devices are closed and switches opened. From  $T_1$  and  $T_2$  the error in  $\Delta T$  is calculated. This error is used in a linear proportional+derivative (PD) control scheme to calculate a new current to be sent to the bottom plate heater.

Since digital to analog (DAC) channels on the LabPC+ board are limited to a resolution of 4096 ( $2^{12}$ ) steps, two DAC channels were used to enhance resolution. Using one channel for coarse grain control and the other for fine grain control provides  $2^{24}$  control steps. After calculating the appropriate current the DAC lines send out the voltages to the summing circuit (Fig. 18). Operational amplifiers scale the voltages on the DAC lines: DAC0 is divided by one and DAC1 is divided by 1000. These are then added together by a third operational amplifier resulting in voltages from 0 to 10 Volts with a resolution of 0.00239 mV. Since the  $T_1$  changes over a much longer time scale than  $T_2$  the inner control loop will repeat the control of  $T_2$  multiple times (typically between 5 and 10) before ending and moving into the outer loop to measure  $T_1$  again.

Simultaneously another linux box is used to regulate  $\bar{T}$  by PID control of the water

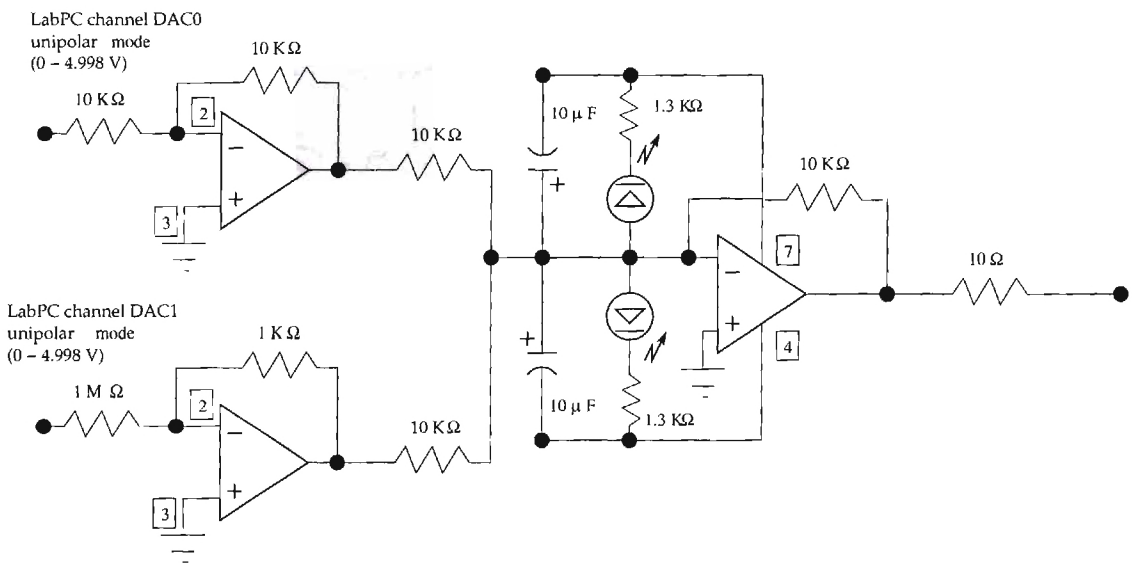


Figure 18: Circuit used in computer control of the bottom plate temperature. It accepts input from two computer channels (DAC0 and DAC1), scales the applied voltage to a fine and a coarse scale resulting in much higher resolution than would be achievable with a single channel. Maximum output voltage is 10 V with a resolution of 0.00239 mV.

bath. The computer controlling  $\Delta T$  streams  $T_1$  and  $T_2$  to files which are then read by the other computers being used for control. Periodically (usually every 60 seconds) the computer controlling  $\bar{T}$  will calculate the current error in  $\bar{T}$ . This error is used in a PID algorithm to calculate the new water bath temperature which is loaded into the bath by a voltage imposed on the controller. Imposed voltage of 10 mV corresponds to a 1 C; thereby, 300 mV input results in a bath temperature of 30 C. Control voltage is sent to the bath by a digitally programmable circuit (Fig. 19). A +5 V reference voltage (Analog Devices REF-02) is multiplied by the gain across the first operational amplifier in Fig. 19 which is inverted and scaled. Circuit output voltage is controlled by altering the gain across the first operational amplifier. Resistance in this gain coefficient is computer controlled by digitally programming two Digital Potentiometers (Analog Devices AD7376) using BASH and GAWK scripts running on the bath control computer. Each Digital Potentiometer has 128 ( $2^7$ ) resistance steps; providing 256 control steps for the circuit shown in Fig. 19. For the anticipated range of 15.0 C to 30.0 C this corresponds to control steps of 0.06 C.

Using the algorithms provided in this subsection reasonable control of  $\Delta T$  and  $\bar{T}$  are achieved. Relatively short response times of the bottom mirror are used to control  $\Delta T$  with a control algorithm with  $\approx 0.6$  seconds between steps. The described control algorithm has an accuracy of  $\Delta T \lesssim \Delta T_{set} \pm 0.008$  C. Transients associated with small changes in  $\Delta T$  are relatively short,  $O(1)$  minute for a change of 1 C. Response of the water bath used to control  $\bar{T}$  is significantly slower. The water bath control algorithm typically performs a control step once every 60 seconds. This control speed is more rapid than the bath can usually respond, but helps keep  $\bar{T}$  constant once the mean temperature has stabilized. Control of  $\Delta T$  is important for most experiments, while

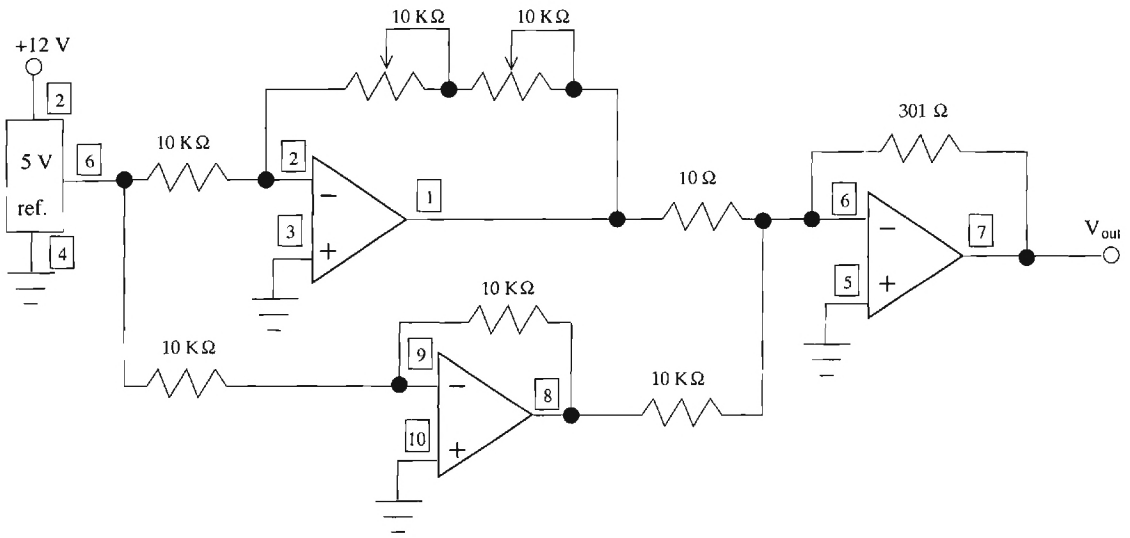


Figure 19: Circuit diagram for the programmable circuit used in controlling the water bath temperature. The boxed numbers are the pin placements for associated connections. Input voltage is supplied by the 5 Volt reference chip. Circuit output voltage ranges from 150 mV to 300 mV depending on the gain present from the operational amplifier. Gain is computer controlled by digitally programming values into two variable resistors providing resolution of 0.5859 mV over the voltage range.

control of  $\bar{T}$  is only necessary for those experiments where it is crucial that one or both of the modulation parameters ( $\delta Fr$  and  $\omega$ ) are held fixed.

### 3.4.2 Pressure

A pressurized gas canister supplies  $\text{CO}_2$  to the experiment which is connected to a downstream pressure sensor and a gas reservoir used for finer resolution pressure control. An overview of the gas supply and regulation system is shown schematically in Fig. 20. A pressurized tank is filled with 99.99% pure  $\text{CO}_2$  at a nominal tank pressure of 830 PSI. This supply is controlled by a Victor model SR 4F regulator rated to 3000 PSI. The regulator may be used to roughly set the convection cell pressure. Downstream from the convection cell is a SensorTec model TJE/3883-12TJA pressure sensor rated to 1000 PSI. Connected downstream from the pressure sensor is a cylindrical aluminum container 5.08 cm in diameter and 10.16 cm in height with a resistive heating pad attached to the bottom. Downstream from the reservoir is a Swaglock Nupro plug valve rated to 206 bar (at 21.1°C) that allows the convection cell to be bled or purged. Clear 0.3 cm tube is used to connect all of these elements with Swaglock fittings on all mounts. Two NPT pressure fittings pass through the upper part of the containment vessel allowing  $\text{CO}_2$  to pass through the pressurized can.

Pressure in the convection cell can be regulated by supplying current to the heating pad, increasing the temperature inside the reservoir, expanding the  $\text{CO}_2$  and increasing the pressure. Prior to starting an experimental run the regulator and shut-off valve are used to set the pressure in the containment vessel to a value  $\approx 1$  to 4 PSI

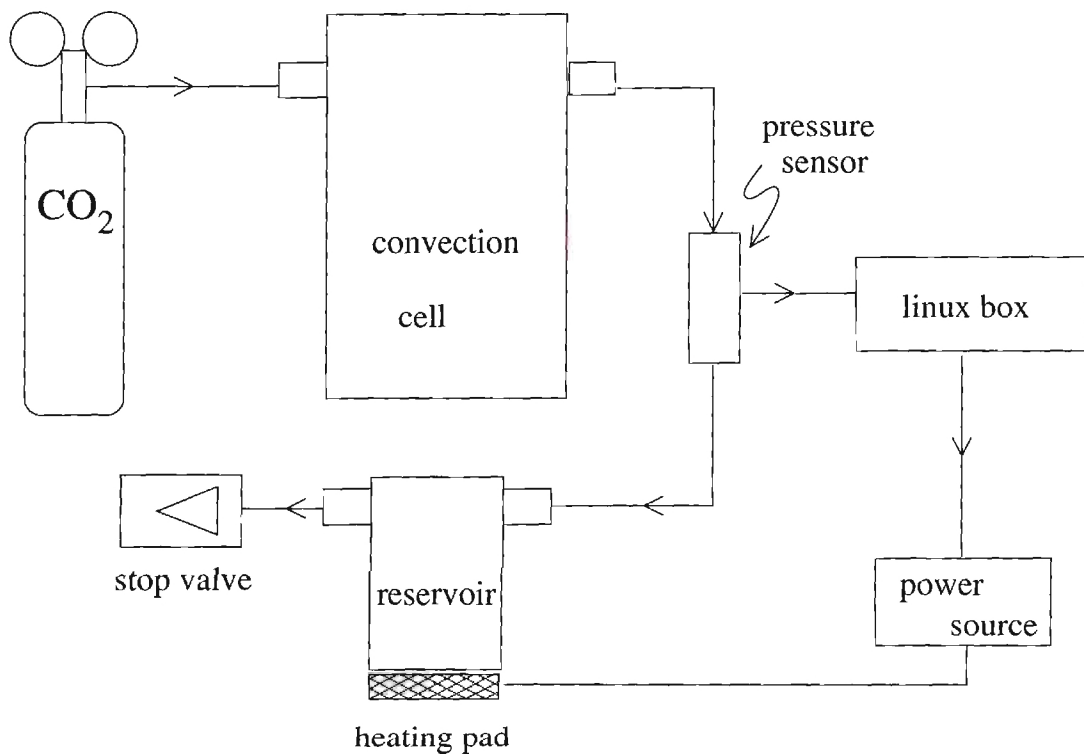


Figure 20: Schematic of the CO<sub>2</sub> supply and pressure control system. Pressurized 99.99 % pure CO<sub>2</sub> is supplied by a tank at 830 PSI. Cell pressure is measured by a SensorTec sensor and fine pressure control is provided by regulating heat supplied to a downstream gas ballast.

below the desired setting. A computer program (P\_ctrl.c) then performs some number of sequential reads of the pressure sensor and uses the average value to find the pressure error. This error is fed through a linear PID control routine which calculates the current that should go to the heating pad until the next control step. Typically, the number of sequential reads is between 100 and 500 while the typical control step is every 1 or 2 minutes.

### 3.5 Analysis

Laboratory data is dynamically analyzed in concert with the experiment to provide the system location in the nondimensional parameter space while the experiment is operating. Calculating the four dimensionless parameters [Eqs. (14)] requires knowing the fluid's physical characteristics  $\nu$ ,  $\kappa$ ,  $\alpha$  as well as the oscillation frequency  $\omega'$  and oscillation displacement amplitude  $\delta'$ . Fluid properties are derived from the recorded data of  $\bar{T}$ ,  $P$  and  $d$  by a computer code developed in Guenter Ahler's group at the University of California-Santa Barbara. This code has been developed and tested over an extended period and can reliably supply a large number of physical characteristics for CO<sub>2</sub>. The dimensioned modulation quantities  $\delta'$  and  $\omega'$  are found from the drive signal recorded at the corresponding data point. Typically, the signal has 16384 points recorded at 100 Hz. Drive signal recording begins when the CCD camera begins acquiring images. After the drive signal is recorded the voltage from an accelerometer is measured. The accelerometer is bolted to the convection cell mounting bracket and provides another source for the drive signal from the instantaneous acceleration, typically recorded at 1000 Hz. Power spectra of these signals computed

in the MatLab environment yield  $\delta'$  in Volts and  $\omega'$  in Hz. From calibrated data  $\delta'$  is converted from Volts to cm by a multiplicative conversion factor. Once  $\nu$ ,  $\kappa$ ,  $\alpha$ ,  $\delta'$ , &  $\omega'$  are found they are plugged into Eqs. (14) with the known quantities of  $g_{stat}$  &  $d$  to produce the data point in the dimensionless four parameter space.

Due to the location of the top thermistor the finite conductivity of the sapphire window introduces a relatively small correction into the measured value of  $T_1$ . Since the bottom thermistor is located inside the aluminum mirror the measured  $T_2$  is a reasonably accurate value. However, the top thermistor being located in the top retaining plate (Fig. 8) requires a correction to the measured  $T_1$  to get accurate values for  $\bar{T}$  &  $\Delta T$ . To approximate the correction to  $T_1$  the thermal conductivity of the CO<sub>2</sub> and the sapphire crystal can be taken into account through the thermal current,

$$\frac{k_{gas}}{d_{gas}} \Delta T_{gas} = \frac{k_{sap}}{d_{sap}} \Delta T_{sap}, \quad (15)$$

where  $k$  is the coefficient of thermal conductivity,  $d$  is the thickness of the material, and  $\Delta T$  is the temperature difference across the material. The subscripts *gas* and *sap* indicate the material; CO<sub>2</sub> and sapphire, respectively. Using values from the CRC tables [58] yields,

$$\Delta T = \Delta T' \left[ 1 - \frac{1}{(1 + 766.47d)} \right] \quad \text{and} \quad \bar{T} = \bar{T}' + \frac{1}{2} \left[ \frac{\Delta T'}{(1 + 766.47d)} \right], \quad (16)$$

where  $\Delta T'$  is the measured temperature difference,  $\bar{T}'$  is the measured mid plane temperature, and  $d$  is the fluid layer depth.

Quantities and techniques used to analyze patterns throughout this dissertation are introduced through the characterization of a computer-generated pattern (Fig.

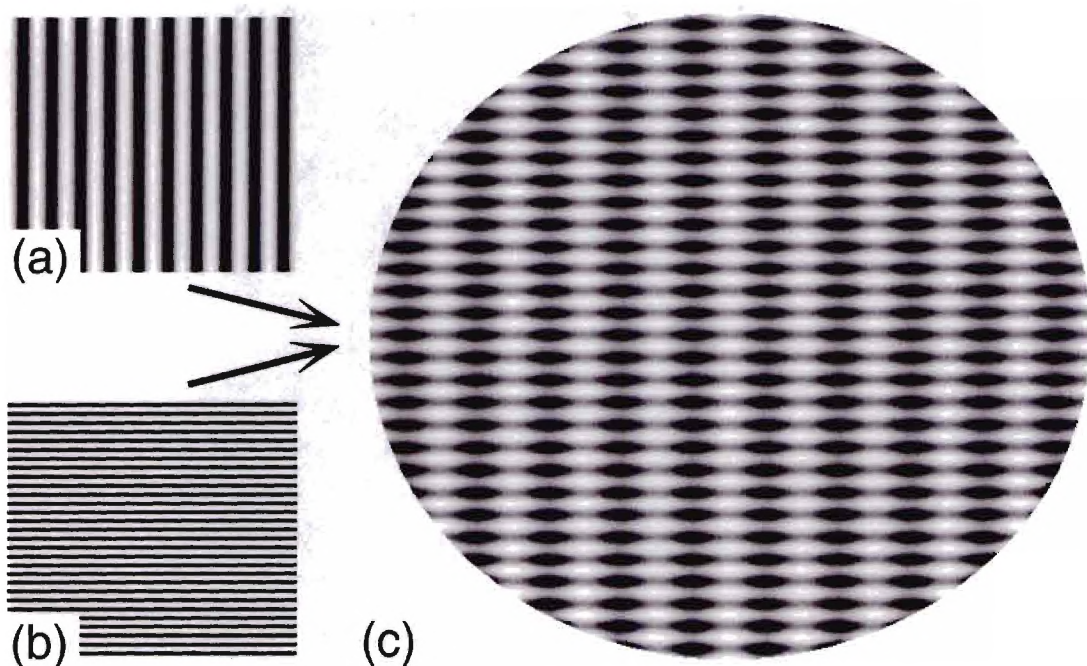


Figure 21: Computer generated patterns  $u(x, y) = \cos qx$  (a) and  $u(x, y) = \cos 2.9qy$  (b) are summed to produce a pattern (c) composed of wave numbers typical of experimental images. All these patterns are 480 by 480 pixels with a circular mask applied to (c) to simulate the experimental lateral boundaries.

21). Like the majority of the experimental images to be described the computer generated pattern is defined on a 480 by 480 point grid. In the experimental images this grid occurs from digitizing the continuous image. The computer generated pattern is defined by  $u(x, y) = \cos q_x x + \cos q_y y$ , where  $u(x, y)$  is the pattern intensity at the Cartesian pair  $(x, y)$ ,  $q_x$  is the horizontal wave number and  $q_y$  is the vertical wave number. To facilitate comparison with experiments  $q_x$  and  $q_y$  are chosen to have a ratio representative of typically observed patterns ( $q_y/q_x = 2.9$ ). Analysis of the patterns begins with calculation of the mean ( $\langle u \rangle$ ) and variance [ $var(u)$ ] of pattern intensities defined by

$$\langle u \rangle = \frac{1}{nm} \sum_{j=1}^n \sum_{i=1}^m u_{ij} \quad \text{and} \quad (17)$$

$$var(u) = \frac{1}{nm} \sum_{j=1}^n \sum_{i=1}^m (u_{ij} - \langle u \rangle)^2, \quad (18)$$

respectively. Since the computer-generated pattern is symmetric about zero  $\langle u \rangle = 0$ .

Pattern characteristics can often be well described in the wave number domain. To reduce the aliasing (an effect of working with a finite pattern) a radial Hanning mask is applied to the image. The family of Hanning masks [ $H(r)$ ] are defined by,

$$H(r) = \begin{cases} \frac{1}{2}[1 + \cos(\pi r/r_0)], & r \leq r_0 \\ 0, & r \geq r_0 \end{cases} \quad (19)$$

where  $r$  is the radius from the image mid point and  $r_0$  determines the radius at which the pattern tapers off. For these investigations  $r_0 = 240$ . The two-dimensional spatial Fourier Transform is performed on the masked image. The Transform provides the relative phase angles and magnitude squared (power spectrum) of the image in wave

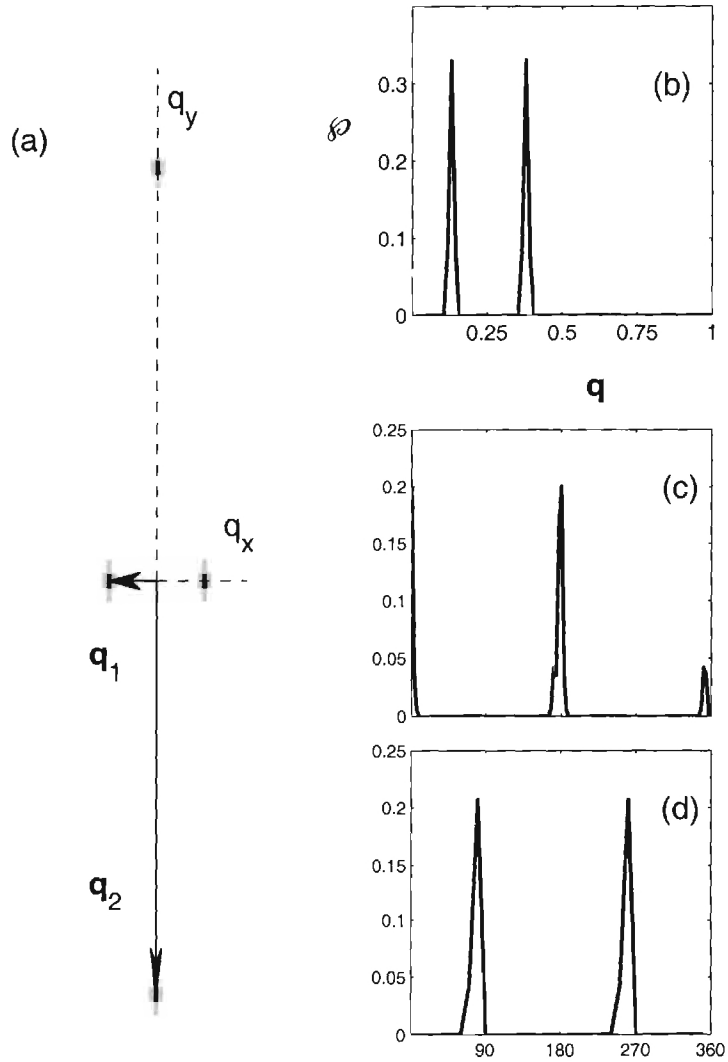


Figure 22: Power spectrum for the computer generated pattern in Fig. 21(c). (a) Two-dimensional spatial power spectrum can be represented in terms of (b) the radial power  $[\phi(q)]$  and angular power populations (c & d). Angular power is computed over wave number bands.

number space. Populated lattice sites indicate the wave numbers present in the real space pattern. Each of the four power spectrum corners is a point of zero wave number. The power spectrum is divided into four square panels, each of which is reflected so zero wave number occurs at the power spectrum center. Wave vectors (modes) of the same magnitude then lie on a circle centered about the power spectra center. The example patterns' power spectra [Fig. 22(b)] displays four discrete peaks, divided into two pairs. The inner pair of peaks have wave numbers of  $q_x$  and the outer pair of peaks has wave numbers of  $q_y$ . For the example pattern where only a few discrete modes are populated the simplest method for determining the patterns' spectral structure is to calculate the wave numbers and angles for each populated mode directly.

However, experimental patterns often contain various defects that result in domains of multiple orientations and a distribution of wave numbers. The wave number over a given range may be defined by the weighted average populated wave number over a band. Attaining laboratory patterns that are sufficiently ideal that only a few modes are required for a complete spectral description is relatively unusual. Typically, the desired information is the global average wave number ( $q$ ) over some wave number band of interest. For these purposes it is convenient to separate the two-dimensional power spectra information into radial [Fig. 22(b)] and angular [Fig. 22(c) & 22(d)] components. These components are then averaged over all of the images acquired at a given set of parameters, yielding average  $q$  distributions in radial and angular directions. Three spectral quantities useful for describing patterns can be found directly from the average radial power. The first is the relative power ( $\rho$ ), which is typically computed over a band of wave numbers. In the example pattern

(Fig. 21) stripes in the horizontal and vertical directions were chosen to have two distinct wave numbers  $q_x$  and  $q_y$  ( $q_x = 2.9q_y$ ). Correspondingly, the radial power (power as a function of  $q$ ) displays two peaks [Fig. 22(b)]. To compute the power at  $q_x$  and  $q_y$  a band of wave numbers about each peak is considered. Contributions to the distribution are excluded when they drop below some noise threshold, typically set to 0.5%. Applying this method once to a band of wave numbers about each of the two pronounced peaks in Fig. 22(b) yields the relative contribution from the vertical stripes [Fig. 21(a)]  $\wp_x = 0.499$  and the relative contribution from the horizontal stripes [Fig. 21(b)]  $\wp_y = 0.499$ . Since the power spectrum can be understood as a measure of the variance in a pattern over a set of wave vectors and both the vertical (x) and horizontal (y) components of the example pattern have unity amplitudes the power contributions at the two distinct wave numbers should be equal. The first two moments of  $\wp(q)$  distributions,

$$\langle q \rangle = \frac{\int_{q=0}^{\infty} q^2 \wp(q) dq}{\int_{q=0}^{\infty} q \wp(q) dq} \quad (20)$$

$$\langle q^2 \rangle = \frac{\int_{q=0}^{\infty} q^3 \wp(q) dq}{\int_{q=0}^{\infty} q \wp(q) dq}, \quad (21)$$

may be used to define the compute the global wave number  $q = \langle q \rangle$  and the width of a  $q$  distribution ( $\sigma = \sqrt{\langle q^2 \rangle - \langle q \rangle^2}$ ). Using the set of programs written to analyze the experimental images yields:  $q^H = 0.131$ ,  $\sigma^H = 7.61 \times 10^{-3}$ ,  $q^S = 0.380$ , and  $\sigma^S = 7.59 \times 10^{-3}$ . From these calculated wave numbers the ratio  $q^S/q^H = 2.90$  in confirmation of the originally chosen wave numbers.

## 3.6 Numerics

### 3.6.1 Conduction Marginal Stability

As a first step in considering the effects of time dependent acceleration on convection, calculations of conduction stability are performed. Using a Galerkin method as described by Clever, Schubert & Busse [52] the predictions of modulation enhanced conduction stability are reproduced over a range of parameters. Conduction is found to be significantly stabilized by time dependent acceleration. For the purpose of the analysis the fluid is assumed to lie between two parallel plates of infinite lateral extent separated vertically by a distance  $d$ . Temperature of the upper plate is  $T_1$  while that of the bottom plate is  $T_2 = T_1 + \Delta T$ . Both plate temperatures are assumed to be uniform. Boundary conditions at the bounding plates are

$$T = \begin{bmatrix} T_1, & z = 1/2 \\ T_1 + \Delta T, & z = -1/2 \end{bmatrix} \quad \text{and} \quad \mathbf{v} = 0, \quad z = \pm 1/2. \quad (22)$$

The conducting steady state solution ( $\mathbf{v} = 0$ ,  $\frac{\partial}{\partial t} = 0$ ) which satisfies these boundary equations as well as the hydrodynamic equations of motion is given by:

$$T_{cond} = T_0 + \Delta T \left( \frac{1}{2} - z \right). \quad (23)$$

Taking this conducting state as the base state, it is possible to find the conditions for which this state becomes unstable to infinitesimal perturbations, giving way to a convective state. To do so, consider perturbations to the fluid temperature, velocity, and pressure distribution of the base state:

$$T = T_{cond} + \Theta, \quad \mathbf{v} = \mathbf{v}, \quad p = p_{cond} + \delta p. \quad (24)$$

Linearizing the Oberbeck-Boussinesq equations [Eqs. (13)] to consider perturbations about conduction yields:

$$\nabla \cdot \mathbf{v} = 0, \quad (25)$$

$$\nabla^2 \mathbf{v} + (1 + \epsilon \cos \omega t) \Theta \hat{\mathbf{z}} - \nabla p = \frac{1}{\text{Pr}} \frac{\partial \mathbf{v}}{\partial t} \quad (26)$$

$$\nabla^2 \Theta + R v_z = \frac{\partial \Theta}{\partial t}. \quad (27)$$

Due to the symmetry in the  $x$ - and  $y$ -directions, it makes sense to eliminate  $y$  and consider only the  $x$ - and  $z$ -directions. For such a system of two-dimensional motions, the Boussinesq condition allows us to characterize the velocity field by a scalar potential  $\phi$  yielding,

$$\mathbf{v} = \nabla \times (\nabla \times \phi \hat{\mathbf{z}}). \quad (28)$$

Substituting this velocity potential into Eq. 26 and taking the  $y$ -component of the curl of each side of the equation yields

$$\frac{\partial}{\partial x} (\nabla^4 \phi - (1 + \epsilon \cos \omega t) \Theta) = \frac{1}{P} \frac{\partial}{\partial t} \left( \frac{\partial}{\partial x} \nabla^2 \phi \right). \quad (29)$$

Linearizing the temperature equation and inserting the potential gives

$$\nabla^2 \Theta - R \frac{\partial^2 \phi}{\partial x^2} = \frac{\partial \Theta}{\partial t}. \quad (30)$$

We can use Eqs. (29) & (30) with the boundary conditions,

$$\phi = \frac{\partial \phi}{\partial z} = \Theta = 0 \quad \text{at} \quad z = \pm 1/2, \quad (31)$$

to find the linear stability of the base state.

The coupling of the equations along with the nature of the boundary conditions prevents this system from being analytically solvable. Thus, we must find a numerical

approximation. It should be noted that the set of functions

$$f_\nu(z) = \sin[\nu\pi(z + 1/2)], \quad (32)$$

provide an orthogonal basis of solutions which satisfy the boundary conditions for  $\Theta$ , while

$$g_\nu(z) = \begin{cases} \frac{\cosh\left(\tilde{\gamma}_{\frac{1}{2}(\nu+1)}z\right)}{\cosh\left(\frac{1}{2}\tilde{\gamma}_{\frac{1}{2}(\nu+1)}\right)} - \frac{\cos\left(\tilde{\gamma}_{\frac{1}{2}(\nu+1)}z\right)}{\cos\left(\frac{1}{2}\tilde{\gamma}_{\frac{1}{2}(\nu+1)}\right)}, & \text{for } \nu \text{ even} \\ \frac{\sinh\left(\hat{\gamma}_{\frac{1}{2}\nu}z\right)}{\sinh\left(\frac{1}{2}\hat{\gamma}_{\frac{1}{2}\nu}\right)} - \frac{\sin\left(\hat{\gamma}_{\frac{1}{2}\nu}z\right)}{\sin\left(\frac{1}{2}\hat{\gamma}_{\frac{1}{2}\nu}\right)} & \text{for } \nu \text{ odd,} \end{cases} \quad (33)$$

satisfy the boundary conditions for  $\phi$ , where  $\tilde{\gamma}_{\frac{1}{2}(\nu+1)}$  and  $\hat{\gamma}_{\frac{1}{2}\nu}$  are the positive roots of the equations,

$$\begin{aligned} \tanh\left(\frac{1}{2}\tilde{\gamma}\right) - \tan\left(\frac{1}{2}\tilde{\gamma}\right) &= 0 \quad \text{and} \\ \coth\left(\frac{1}{2}\hat{\gamma}\right) - \cot\left(\frac{1}{2}\hat{\gamma}\right) &= 0, \end{aligned} \quad (34)$$

given in Chandrasekhar [59]. Thus, any expansion in these functions will satisfy the boundary conditions. In addition, we will assume a periodic dependence on  $x$  with wavenumber  $q$ .

The functions  $g_\nu(z)$  and  $f_\nu(z)$  above can be divided into two classes: those that are symmetric about  $z = 0$  (cases of odd  $\nu$ ) and those that are antisymmetric about  $z = 0$  (cases of even  $\nu$ ). It was shown by Clever & Busse [60] that the conduction state is stable with respect to antisymmetric perturbations in  $z$  as long as it is stable with respect to symmetric perturbations in  $z$ . Thus, it will suffice to look only at the case in which  $\nu$  is odd.

Finally, we wish to find the condition for marginal stability – that is, when the perturbations neither grow nor shrink in time. Recall from the pendulum stability

discussion in Sec. 2.1 that this means a time dependence of  $e^{\sigma t}$ , where  $Re[\sigma] = 0$ . Due to the sinusoidal driving term, it is expected that  $Im[\sigma] \neq 0$ . In fact, there are two cases to consider. In the first case, the fluid flows at the same frequency (and integer multiples thereof) as the driving force. These are pure *harmonic* flows which may be represented by

$$\begin{aligned}\phi &= \sum_{\substack{\beta+\nu \leq N \\ \beta, \text{ odd } \nu}} (\hat{a}_{\beta\nu} \cos \beta\omega t + \check{a}_{\beta\nu} \sin \beta\omega t)(\cos qx)g_\nu(z) \quad \text{and} \\ \Theta &= \sum_{\substack{\beta+\nu \leq N \\ \beta, \text{ odd } \nu}} (\hat{b}_{\beta\nu} \cos \beta\omega t + \check{b}_{\beta\nu} \sin \beta\omega t)(\cos qx)f_\nu(z).\end{aligned}\quad (35)$$

The other case is one in which the fluid flows with  $1/2$  (and higher odd half integer multiples) of the driving frequency. These are pure *subharmonic* flows, which may be represented by the expansions:

$$\begin{aligned}\phi &= \sum_{\substack{\beta+\nu \leq N \\ \text{odd } \beta, \text{ odd } \nu}} (\hat{a}_{\beta\nu} \cos \frac{\beta}{2}\omega t + \check{a}_{\beta\nu} \sin \frac{\beta}{2}\omega t)(\cos qx)g_\nu(z) \quad \text{and} \\ \Theta &= \sum_{\substack{\beta+\nu \leq N \\ \text{odd } \beta, \text{ odd } \nu}} (\hat{b}_{\beta\nu} \cos \frac{\beta}{2}\omega t + \check{b}_{\beta\nu} \sin \frac{\beta}{2}\omega t)(\cos qx)f_\nu(z).\end{aligned}\quad (36)$$

Note that these expansions are simply the  $N^{\text{th}}$  order truncations of sums which should converge to the exact solution for harmonic or subharmonic oscillations as  $N \rightarrow \infty$ .

All that remains is to take the  $N^{\text{th}}$  order approximation, and plug the expansion into the differential equations. This changes the linear differential equations in  $\Theta$  and  $\phi$  into a system of linear algebraic equations in the coefficients  $\hat{a}_{\beta\nu}$ ,  $\check{a}_{\beta\nu}$ ,  $\hat{b}_{\beta\nu}$ , and  $\check{b}_{\beta\nu}$ . This system yields a characteristic equation in the four nondimensional parameters ( $R$ ,  $Pr$ ,  $\epsilon$  &  $\omega$ ) and a wavenumber  $q$ . Recall that  $\epsilon$  is the acceleration nondimensionalized by gravity and  $\delta Fr = \epsilon/\omega^2$ .

Onset of convection is then determined for a fixed  $Pr$  and  $\omega$  by looking for onset over a range of  $\epsilon$ . For a given  $\epsilon$  a wavenumber  $q$  is chosen, and  $R$  is varied by an amount  $\delta R$  until it yields a root in the secular equation for the linear system. This value of  $R$  is stored, and  $q$  is increased by  $\delta q$ . The procedure is repeated and the smallest root in  $R$  is selected as the  $N^{th}$  order approximation to the critical Rayleigh number ( $R_c$ ) with corresponding wavenumber  $q_c$  for the  $\epsilon$  in question. The entire procedure is then repeated to find  $R_c$  and  $q_c$  over a range in oscillation amplitudes.

The iteration grid in these trials was chosen so that  $\delta R = 10$  and  $\delta q = 0.2$ , yielding the numerical value of  $R_c$  to within  $\pm 5$ . In some cases, multiple values of  $q$  yield identical results for the root in  $R$ . In this case, the mean of all such values is used for  $q_c$ . In no case was this range of  $q$  more than  $\pm 0.2$ , so this  $N^{th}$  approximation to  $q_c$  is found to better than  $\pm 0.1$ . This accuracy is limited by the number of terms used in the expansion. Thus, to find the best value, the truncation parameter  $N$  (recall the expansion is restricted as:  $\beta + \nu \leq N$ ) is increased until the computed approximation to the Rayleigh number changes by less than 5% when  $N$  is replaced by  $N - 2$ . In practice, this convergence was reached for harmonic flows by  $N = 7$ , where the maximum change was 3.6% right at the marginal stability cusp [Figs. 23(a) & 23(c)], and most of the values changed by less than 1%. For subharmonic oscillations, the convergence test was reached when  $N = 6$ , at which point all values changed by less than 1%.

### 3.6.2 Pattern Simulations

The nature of the numerical simulations are beyond the scope of this dissertation and are reported in detail in the dissertation of Oliver Brausch [28]. The basic task

is to solve the Oberbeck-Boussinesq equations [Eqs. (13)], and in some cases retain non-Boussinesq corrections. The numerical codes, which implement a pseudo-spectral method, were developed and tested extensively by Werner Pesch [56] in the context of simulating classical Rayleigh-Bénard convection. Pesch and Brausch modified the classical Rayleigh-Bénard convection codes to account for time dependent acceleration [61] to apply them to the current problem. Additionally, the dissertation of Oliver Brausch contains numerical investigations of behaviors not accessible to the experiments described here, including the case of heating from above ( $T_1 > T_2$ ) and relaxation oscillations.

# CHAPTER 4

## Onset of Convection

This chapter focuses on laboratory investigations of predictions made in the relevant literature for the effects of modulation on convection, the patterns observed near onset and the role of inversion symmetry in selecting the onset planform. First, results from the linear stability analysis described in Sec. 3.6.1, predicting the onset of instability, are presented. These calculations indicate modulation stabilizes conduction against perturbations over a large range of parameters. Second, predictions of modulation shifting onset are confirmed by measuring convection onset at  $\omega = 98.0$  in the laboratory. These measurements confirm the numerical expectations for critical Rayleigh  $R_c$  and wave numbers  $q_c$  at onset. Third, harmonic temporal dependence is experimentally confirmed and the patterns typically observed at harmonic onset are presented. Violations of the Boussinesq symmetry are found to produce hexagons in harmonic patterns over a parameter range. Lastly, subharmonic temporal dependence is confirmed for patterns at the appropriate parameter values and the patterns typical of subharmonic onset are presented and discussed.

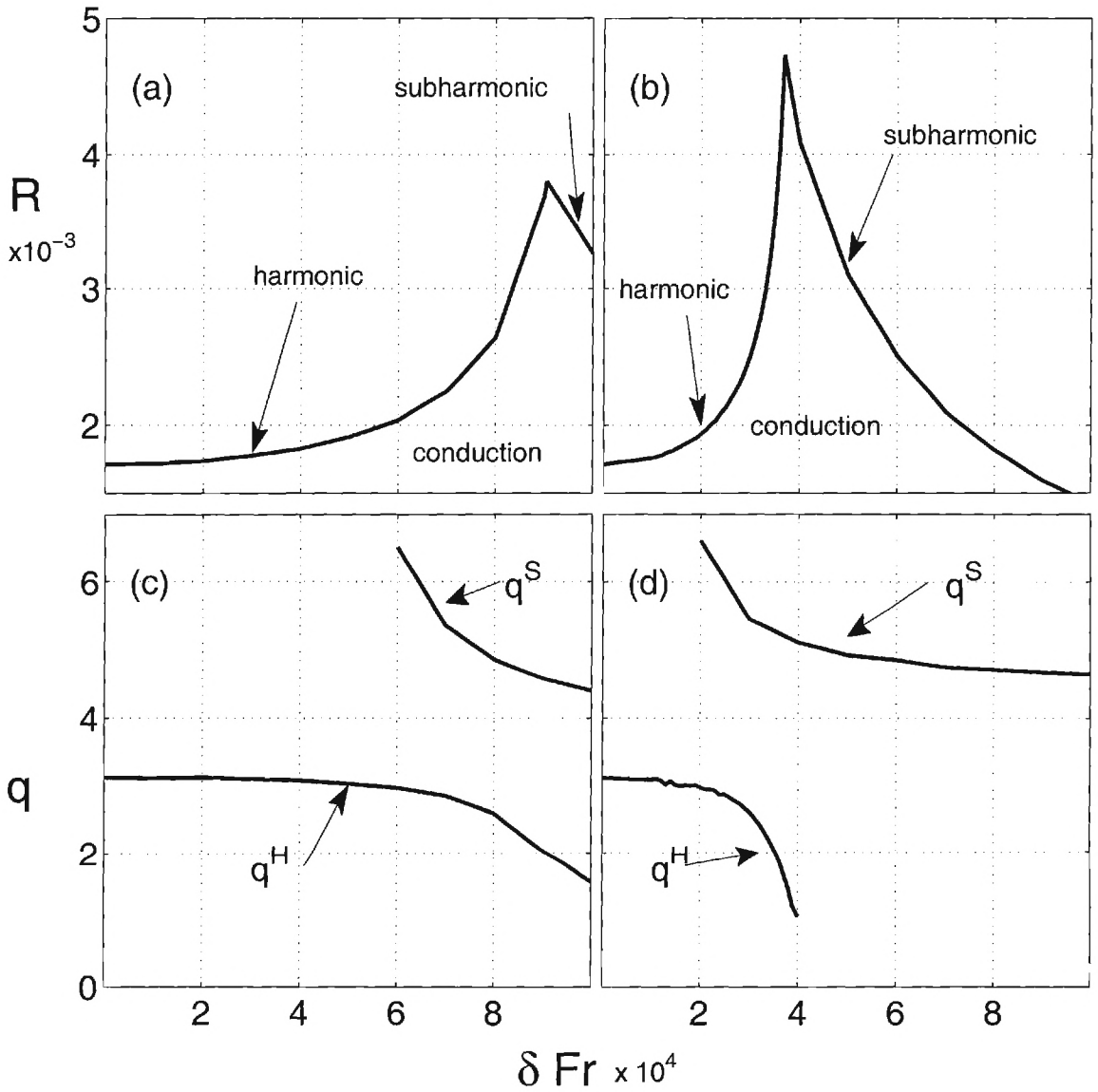


Figure 23: Results from a marginal stability analysis of the Boussinesq equations [Eqs. (13)] linearized about the conduction state for  $Pr = 0.93$  and  $\omega = 50$  (a & b) as well as  $\omega = 100$  (c & d).

## 4.1 Onset Predictions

Conduction marginal stability calculations indicate shifts in the onset of convection [Fig. 23(a) & 23(b)] are sensitive to the values of the modulation parameters ( $\delta Fr$  &  $\omega$ ). As described in Sec. 3.6.1 fluid motion is expected to display either harmonic (periodic at  $\tau$ ) or subharmonic (periodic at  $2\tau$ ) temporal dependence. The marginal stability curve for harmonic convection intersects with the classical Rayleigh-Bénard value  $R_c^0$  in the no-shake limit. Increasing modulation from the no-shake limit the onset of harmonic convection occurs at only slightly larger values initially. However, as either  $\delta Fr$  or  $\omega$  continue to increase the stabilization of conduction becomes significant [Fig. 23(a) & 23(b)]. In fact, the slope of the harmonic stability curve becomes quite large rather abruptly for sufficient modulation parameters. At larger values of the modulation parameters the harmonic instability is preceded by a subharmonic instability. With increasing  $\delta Fr$  or  $\omega$  conduction will be stable over a diminishing range of  $R$ . Depending on the modulation parameters subharmonic convection instability is expected to destabilize conduction below  $R_c^0$ . For example, at  $\omega = 100$ ,  $R < R_c^0$  for  $\delta Fr \gtrsim 9 \times 10^{-4}$ . Thus modulation may have a stabilizing or destabilizing effect depending on the values of the modulation parameters.

Marginal stability analysis also indicates the wave numbers of harmonic and subharmonic convection at onset ( $q^H$  &  $q^S$ , respectively) may take on significantly different values. For  $Pr \approx 1$  fluids (here  $Pr = 0.93$ )  $q^H$  is relatively independent of the modulation parameters except in the vicinity of the intersection of the marginal stability curves. By contrast,  $q^S$  is strongly dependent on the modulation parameters. In these investigations  $q^H > q^S$ .

A potentially interesting area of the parameter space is the intersection of the harmonic and subharmonic marginal stability curves. At this cusp conduction is stable over the largest region of  $R$  while varying either  $\delta Fr$  or  $\omega$  and holding the other modulation parameter fixed. Additionally, at the point of intersection conduction is expected to become unstable to both harmonic and subharmonic convection simultaneously. Onset at the *bicritical* point could occur to patterns at  $q^H$  &  $q^S$  or some combination of the two distinct wave numbers. The primary bifurcation at the bicritical point has a codimension of two. In parameter space the bicritical point location ( $\delta Fr = \delta Fr_{2c}$ ,  $R = R_{2c}$ ) moves to smaller  $\delta Fr$  and larger  $R$  with increasing  $\omega$  [Fig. 23(a-b)].

## 4.2 Onset Measurements

In the no-shake limit ( $\delta Fr = 0$ ,  $\omega = 0$ ) the experiment reduces to classical Rayleigh-Bénard convection. Onset of convection in classical Rayleigh-Bénard convection occurs at  $R_c^0 = 1708$  with  $q_c^0 = 3.116$ . If spatial inversion (Boussinesq) symmetry is approximately present the onset planform is parallel stripes. Our no-shake experiments find parallel stripes at onset (Fig. 24). Hexagons are not observed in the no-shake onset measurements indicating the Boussinesq symmetry is present at correspondingly small temperature differences,  $5.5 \lesssim \Delta T \lesssim 6.5$  C, depending on the cell depth.

Moving away from the no-shake limit by imposing vertical oscillations experiments confirm conduction is stabilized in quantitative agreement with marginal stability predictions [Figs. 25(a) & 58 – App. A]. Experiments mapping the onset of convection

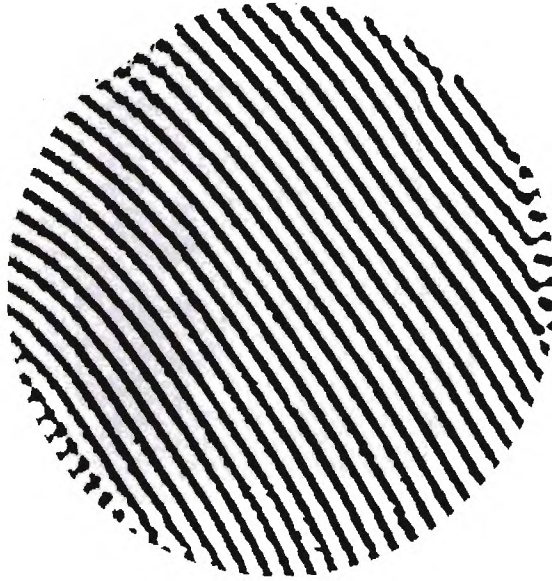


Figure 24: Parallel stripes observed near onset ( $Pr = 0.943$ ,  $R = 1760$ ) in the absence on shaking ( $\omega = 0$ ).

are performed at  $\omega = 98.0$ . Since  $\delta Fr \sim d^{-4}$  and  $R \sim d^3$  any small errors in the measurement of  $d$  are appreciable in the experimentally determined parameter values. By adjusting  $d$  within the certainty of its measurement the data points in Fig. 25 collapse directly on the linear stability curves.

In agreement with results previously reported by other investigators the current numerics indicate harmonic and subharmonic patterns display significantly different wave numbers. Shown in Fig. 23(c-d) are the predicted onset values for harmonic wave numbers  $q_c^H$  and subharmonic wave numbers  $q_c^S$  at (a)  $\omega = 50$  and (b)  $\omega = 100$ . Wave numbers of laboratory patterns are the first moment of a distribution in the radial power ( $\rho$ ) averaged over all images recorded at a data point (see Sec. 3.5 for example). Additionally, the second moment of this power distribution is the variance of the  $q$ -distribution, indicating the width  $\sigma$ . The  $q$ -values shown in Fig. 25(b) are

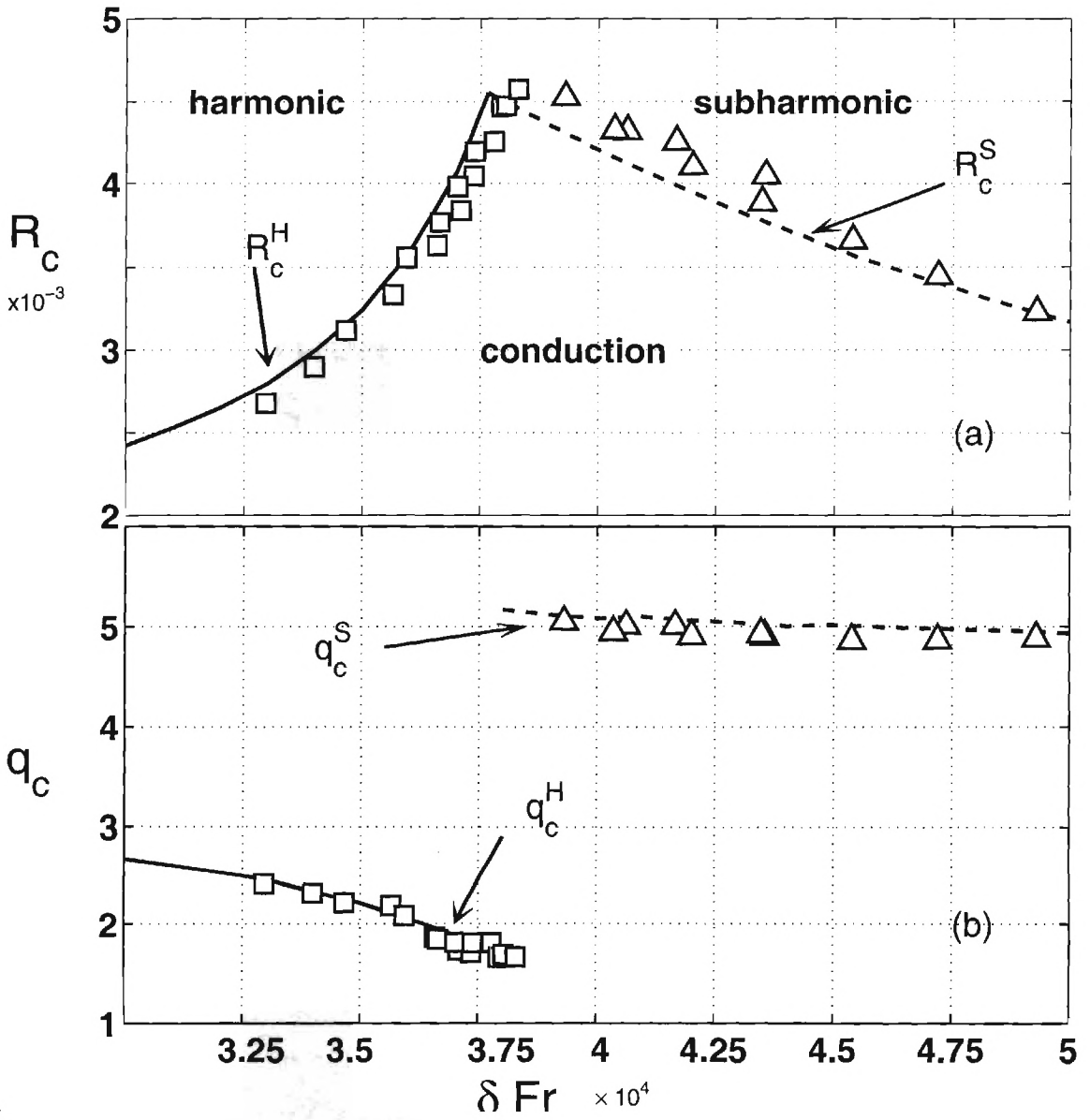


Figure 25: Comparison of conduction stability predictions with laboratory observations made at  $\omega = 98.0$  for (a)  $R_c$  and (b)  $q_c$ . Harmonic measurements are denoted by  $\square$  while  $\triangle$  marks measurements at subharmonic onset.

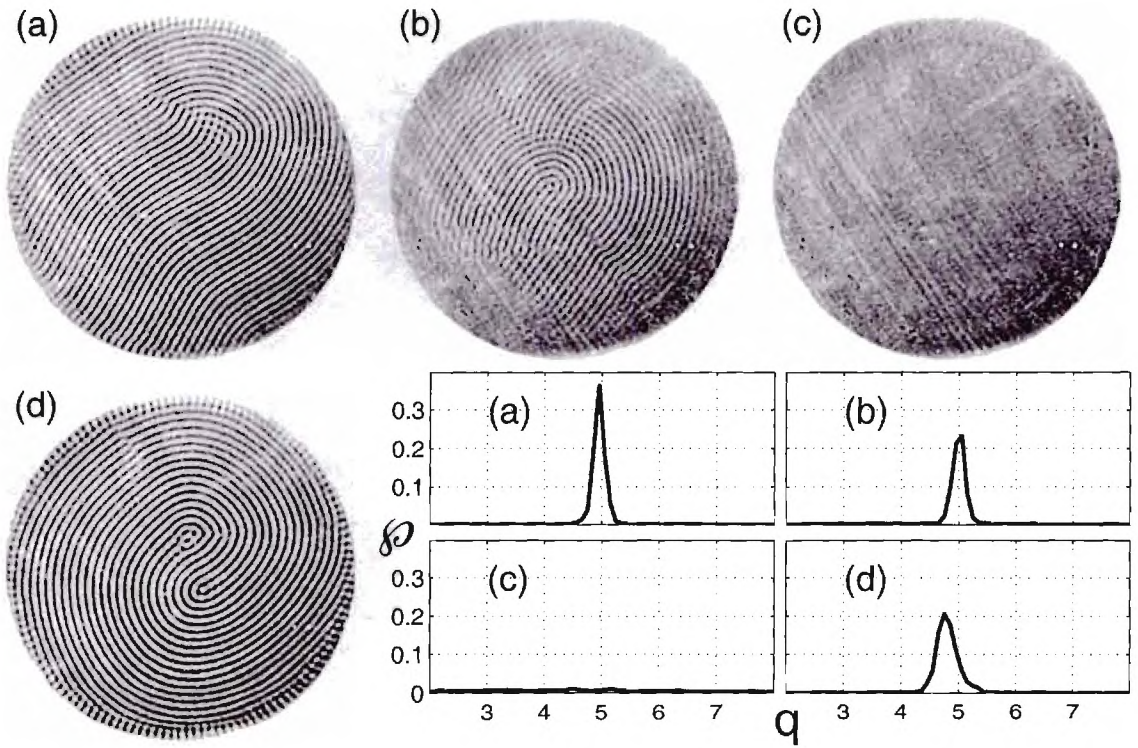


Figure 26: Images from an automated experimental run to determine stability boundaries and the corresponding  $\phi(q)$  for each image. Parameters are  $\omega = 99.4$  for all points and (a)  $\delta Fr = 4.06 \times 10^{-4}$  &  $R = 4280$ , (b)  $\delta Fr = 3.99 \times 10^{-4}$  &  $R = 4260$ , (c)  $\delta Fr = 4.91 \times 10^{-4}$  &  $R = 4260$ , and (d)  $\delta Fr = 4.29 \times 10^{-4}$  &  $R = 4220$ .

for the patterns observed at the last experimental data point before crossing into conduction. For the crossing shown in Fig. 26 the pattern used to calculate  $q^S$  is Fig. 26(b). Data used in producing Fig. 25(b) is the same as that used to produce Fig. 25(a).

In the laboratory these points are determined by slowly increasing  $\delta Fr$  at some  $R > R_c$  in steps of  $1 \times 10^{-6}$  until fluid motion is no longer detectable. The temperature difference is then incremented and the amplitude is decreased or increased sufficiently to ensure convection. Once the experiment displays convection  $\delta Fr$  is slowly varied to again approach conduction. This 'zig-zagging' across the marginal stability line is repeated as the experiment maps out the boundary. Each time the system parameters are changed the fluid was allowed to relax for  $\approx 3000\tau_v$  (45 minutes) before data is recorded to allow transients to die away. After recording images and moving them onto hard disk MatLab scripts on another computer analyzed the images by subtracting a uniform state background from each image and computing the spatial power spectra. When less than 10% of the individual images (typically 64 at each data point) displayed power at wavelengths less than the pixel width of the cell the state was called conduction. Post analysis of these trials demonstrated the reliability of this approach and typically the dynamical analysis did an excellent job of recognizing the loss of fluid motion.

Classical Rayleigh-Bénard convection studies (no-shake) have found pattern symmetries observed at onset are dependent on the nature of the primary bifurcation [62, 63, 64]. In the presence of Boussinesq symmetry, stripes are observed as a result of a supercritical (forward) primary bifurcation. When Boussinesq symmetry is not maintained the forward stripe bifurcation is unstable. Instead, hexagons are observed

at onset as the result of a subcritical (backwards) bifurcation (Fig. 1). Associated with this backwards bifurcation is a region of hysteresis allowing hexagons to be stable below the original onset. Moving away from onset stripes become the stable solution. Depending on the fluid and convection cell geometry used there may be an intermediate region of stripe-hexagon bistability observed [64, 63]. Bodenschatz *et al.* [62] studied the primary bifurcation in unmodulated compressed CO<sub>2</sub> when Boussinesq symmetry was violated. These authors confirmed the predicted bifurcation diagram for the stability of stripe and hexagon solutions. Using a large aspect ratio cell ( $\Gamma = 86$ ) and carefully controlling physical quantities they were able to observe the expected hysteresis in experiments, but did not observe stripe-hexagon bistability. The stability width for these various regions is dependent on how the Boussinesq symmetry is violated. In the experiments of Bodenschatz *et al.* a large  $\Delta T$  ( $\approx 29$  °C) was used to break Boussinesq symmetry by making the temporal dependence of the fluid properties significant enough that non-Boussinesq effects could be observed.

To investigate the nature of the bifurcations for acceleration modulated Rayleigh-Bénard convection two types of experimental approaches are employed. First,  $\delta Fr$  is slowly increased (decreased) from harmonic (subharmonic) convection while  $R$  is held fixed. After the system has passed into the conduction regime it continues slowly adjusting parameters to move further into conduction. While remaining at fixed  $R$  the experiment then 'turns-around' decreasing (increasing)  $\delta Fr$  until convection is again observed. Second, the 'zig-zagging' approach originally employed to determine the boundaries is used, only this time the system finds the boundary from inside conduction. In particular, the system begins from the conduction region and decreases

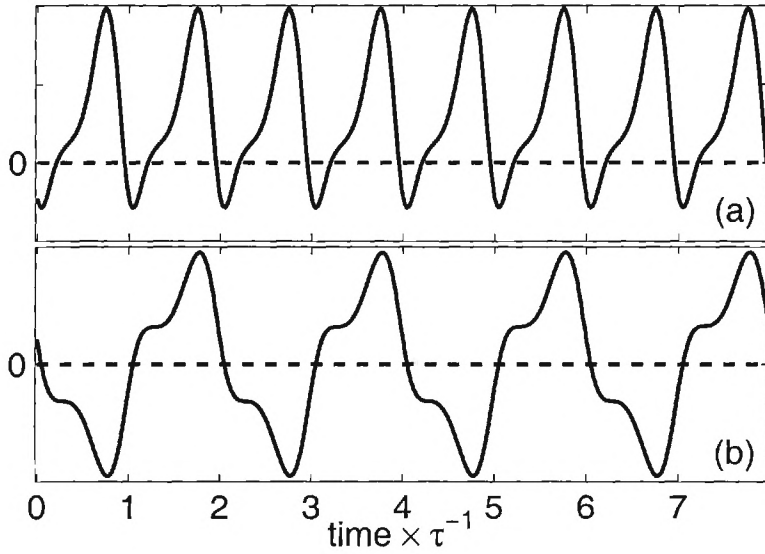


Figure 27: Temporal dependence of Fourier modes (*simulation*) in the fluid layer mid plane during simulations of (a) purely harmonic convection and (b) purely subharmonic convection.

(increases)  $\delta Fr$  at constant  $R$  until convection is detected. Next,  $R$  is changed and  $\delta Fr$  is increased (decreased) sufficiently for the system to be back in conduction. Now the whole process begins again as the experiment determines the next onset at the new fixed  $R$ . Marginal stability boundaries found from the first method as well as from comparing the boundaries found by zig-zagging along onset beginning from convection and conduction did not display hysteresis greater than the experimental resolution in  $\delta Fr$  ( $\approx 2 \times 10^{-6}$ ).

## 4.3 Harmonic Onset

### 4.3.1 Temporal Dependence

At relatively small modulation parameters fluid motion is expected to be harmonically modulated. For harmonic stripe patterns numerics indicate particle velocities will oscillate about nonzero mean [Fig. 27(a)]. Thereby, while volume element velocity will reverse directions during a drive cycle, on average the fluid will overturn. Heat-flux across the fluid layer is less than in the absence of modulation. While measuring particle velocities is not feasible for pure CO<sub>2</sub> the expected variations in temperature should be observable in the shadowgraph imaging technique. Shadowgraphy images the lateral temperature field gradients averaged over the depth of the fluid layer. Fig. 28 confirms the expected temporal dependence for a harmonic stripe pattern by showing the parallel stripe state changes at  $\tau/2$  and is periodic at  $\tau$  in the laboratory.

### 4.3.2 Harmonic Onset Patterns

At harmonic onset parallel stripes [Fig. 29(a)] and targets [Fig. 29(b)] are observed, both of which may contain domains of hexagons [Fig. 29(c-d)]. Parallel stripes and targets may be found anywhere ( $2000 \lesssim R \lesssim 4500$ ) along the harmonic stability curve [Fig. 25(a)], while domains of hexagons only occur close to onset at larger  $R$  values ( $3800 \lesssim R \lesssim 4800$ ). From classical Rayleigh-Bénard convection studies in compressed gases ( $Pr \approx 1$ ) it is known that parallel stripes form when the side wall forcing is minimal and that cell filling (giant) targets or spirals are present near onset when the side wall forcing is more significant (for example, due to side wall heating [65]). In

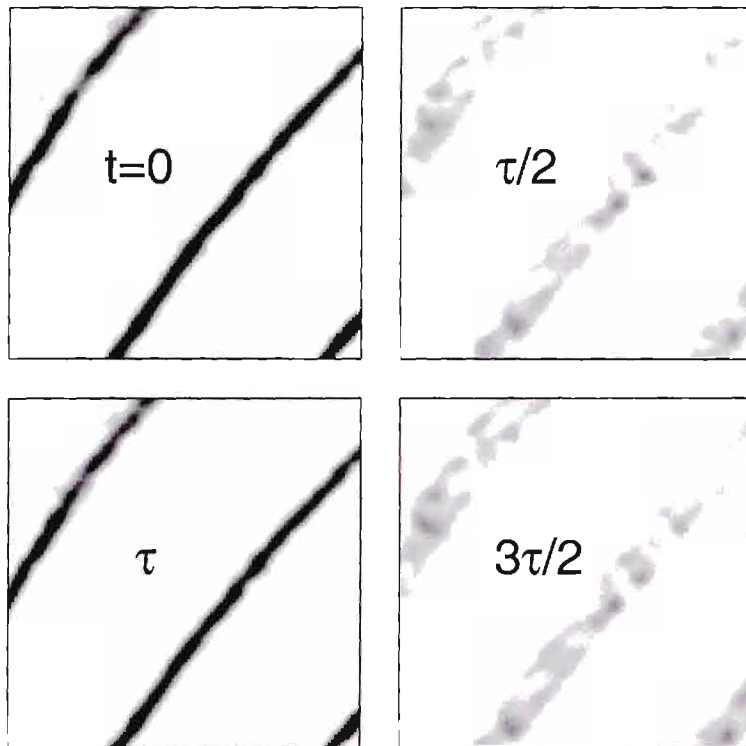


Figure 28: Shadowgraph (*experiment*) displaying harmonic temporal resonance, periodicity at  $\tau$ . At  $t = 0$  (a) the stripe state is well defined. For odd multiples of  $\tau$  (b & d) the stripe state becomes broader, while at even multiples of  $\tau$  the original state repeats (c). Each 128 by 128 pixel frame is over the same spatial location separated in time by  $\tau/2$ .

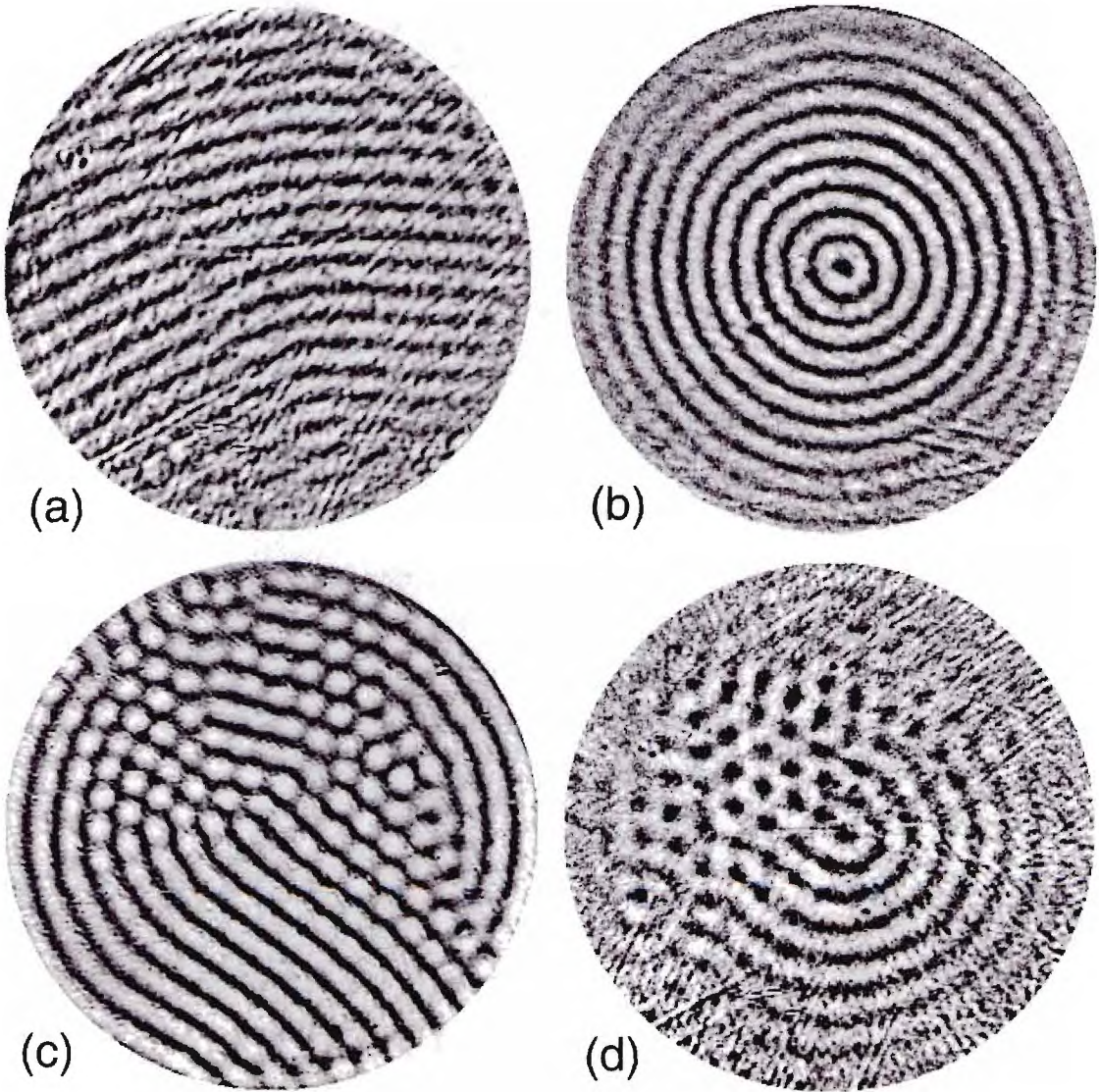


Figure 29: Harmonic onset striped patterns include: (a) parallel stripes ( $\delta Fr = 3.34 \times 10^{-4}$ ,  $\omega = 97.8$  &  $R = 3002$ ), (b) targets ( $\delta Fr = 3.29 \times 10^{-4}$ ,  $\omega = 98.0$  &  $R = 2979$ ), (c) stripes with hexagons ( $\delta Fr = 3.71 \times 10^{-4}$ ,  $\omega = 96.2$  &  $R = 4388$ ), and (d) targets with hexagons ( $\delta Fr = 3.76 \times 10^{-4}$ ,  $\omega = 96.6$  &  $R = 4107$ ).

the experiments we performed the forcing due to the side walls varies with the different experimental configurations. Stronger side wall forcing from the circular lateral boundary results in targets while weak side wall forcing allows a parallel stripe formation. In the experiments described here harmonic targets and spirals are observed during particular sets of laboratory trials. Targets may display light or dark cores, designating cold (downflowing) or warm (upflowing) centers, respectively. Domains of hexagons may be present in both striped and target base states at larger  $R$  values with the domains of hexagons becoming larger with  $R$ . Hexagons with both downflowing centers [Fig. 29(c)] and upflowing centers [Fig. 29(d)] are observed. Transitions between domains of locally upflowing and downflowing hexagons are also observed. Meyer, Cannell, & Ahlers reported [39] similar mixed stripe-hexagon patterns in a study of thermally modulated Rayleigh-Bénard. They were able to measure the various expected bifurcation points expected to be associated with non-Boussinesq effects resulting in a backwards bifurcation. Mixed hexagon-stripe states were observed when the hexagon and stripe attractors were expected to be simultaneously stable (corresponding to  $R_r < R < R_b$  in Fig. 1). Hexagons in the experiments of Meyer, Cannell, & Ahlers were reported to have downflowing centers with no mention of upflowing hexagons. Onset hexagons are not inversion symmetric. The presence of hexagonal domains indicates Boussinesq symmetry is no longer valid at the corresponding experimental conditions allowing resonant triads between the harmonic modes to select the hexagons. In thermally modulated Rayleigh-Bénard Boussinesq symmetry is violated by a nonlinear temperature profile. In the current experiments Boussinesq symmetry is broken due to the increased  $\Delta T$  ( $R \sim \Delta T$ ) required to reach such large  $R$  values. It should be expected that harmonic hexagons will be most noticeable in the vicinity

of the bicritical point since this is the conduction cusp where  $\Delta T$  is the largest at onset. Over the purely harmonic region the majority of stable states are strikingly similar to patterns found in classical Rayleigh-Bénard convection studies.

## 4.4 Subharmonic Onset

### 4.4.1 Temporal Dependence

At sufficiently large modulation parameters conduction is expected to lose stability to convection displaying subharmonic time dependence [Fig. 27(b)]. This type of fluid motion should occur as the system passes through the dashed line in Fig. 25(a). Oscillations in the subharmonic temperature field must satisfy the subharmonic time translation (inversion) symmetry which requires the field variables invert under discrete time translation by  $\tau$ . In terms of the shadowgraph this is displayed by the light and dark pattern areas switching every  $\tau$ . In the laboratory the experiment was tuned to just beyond the subharmonic marginal stability curve where a particular defect (convex disclination) that emphasizes inversion is common. Every even multiple of  $\tau$  the pattern in Fig. 30(a) occurs and every odd multiple of  $\tau$  the pattern in Fig. 30(b) is present. For Fig. 30(b) an arbitrary odd frame is chosen ( $t = 35\tau$ ) to demonstrate the switching. Due to the symmetric switching fluid packets would not turn over and consequently heat flux will be greatly reduced when compared to the flux in the absence of modulation.

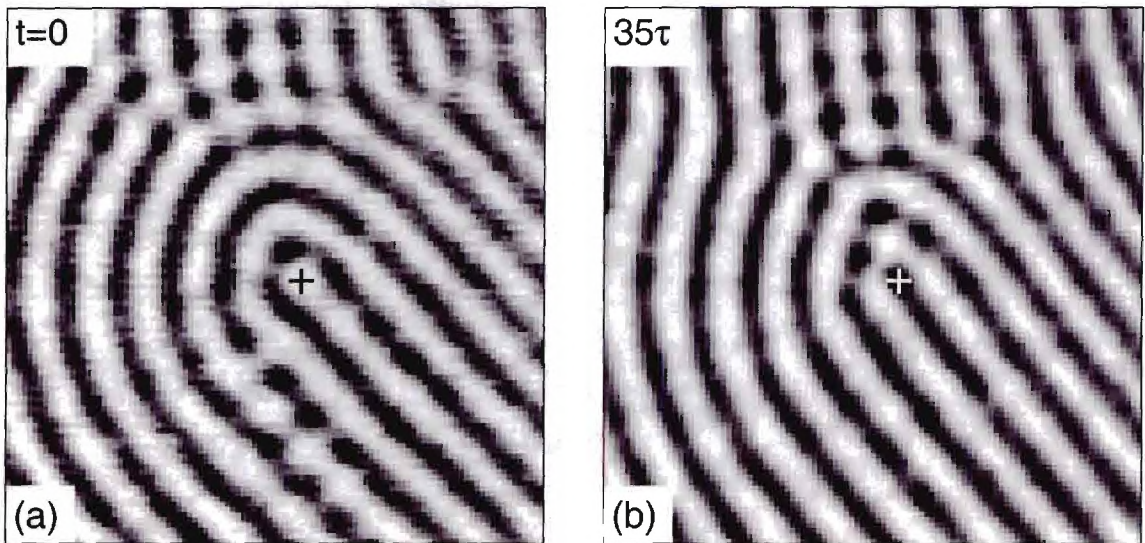


Figure 30: Close up of a convex disclination confirming subharmonic temporal dependence. Note, the + signs near the image centers, these are plotted at the same coordinates in both frames. The disclinations center stripe is light at even multiples of  $\tau$  [(a)  $t=0$ ] and dark at odd multiples of  $\tau$  [(b)  $t = 35\tau$ ]. Shown are the same spatial locations of 128 by 128 pixel images with the + signs at the same pixel values.

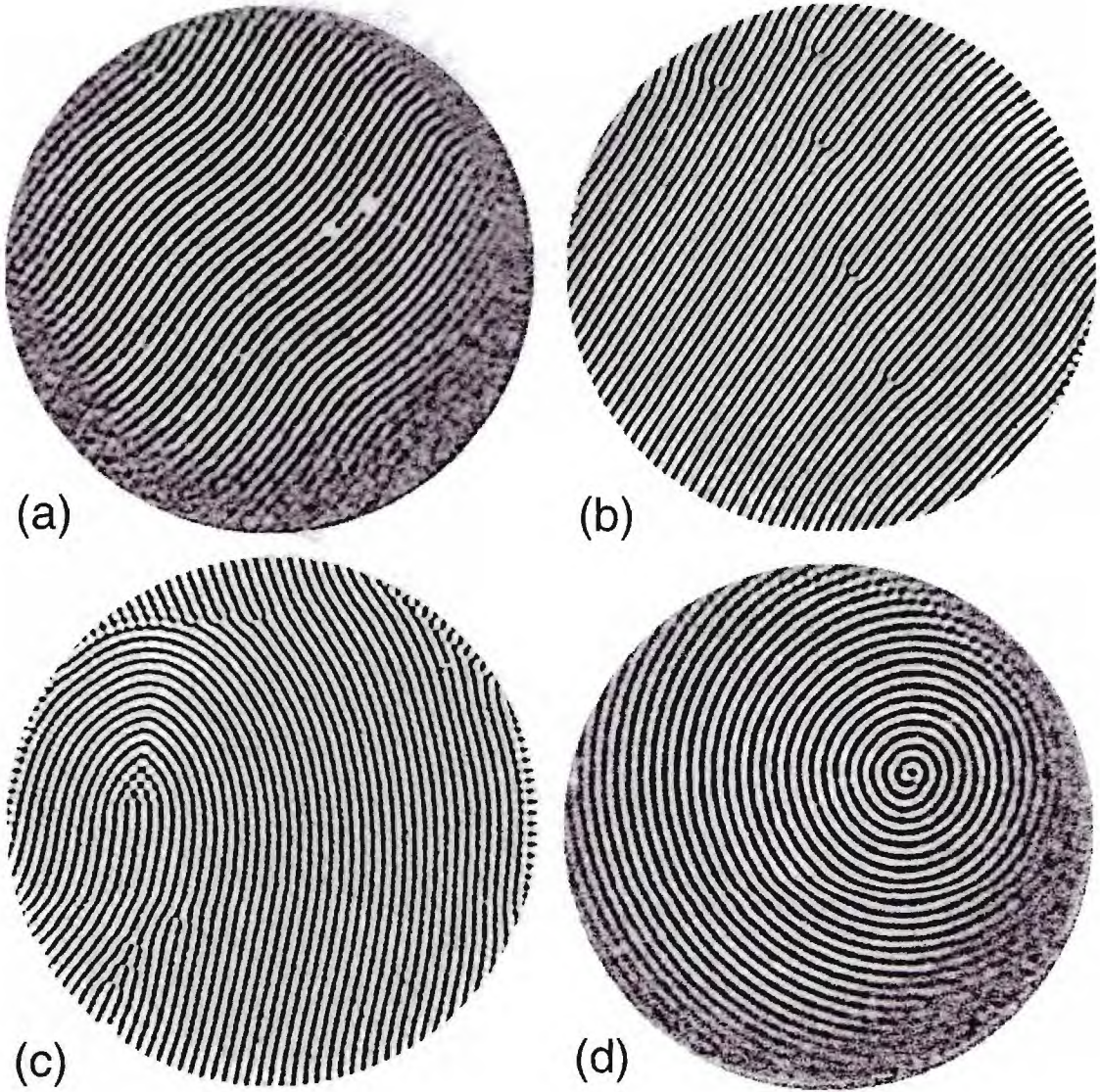


Figure 31: Examples of patterns observed near onset of subharmonic convection. Patch (a) of parallel stripes ( $\delta Fr = 4.02 \times 10^{-4}$ ,  $\omega = 97.9$  &  $R = 4395$ ), (b) parallel stripes with five dislocations ( $\delta Fr = 3.74 \times 10^{-4}$ ,  $\omega = 97.9$  &  $R = 4857$ ), (c) stripes with a giant convex disclination and several dislocations ( $\delta Fr = 3.34 \times 10^{-4}$ ,  $\omega = 97.5$  &  $R = 4811$ ), and (d) onset spiral ( $\delta Fr = 4.12 \times 10^{-4}$ ,  $\omega = 97.9$  &  $R = 4173$ ).

## 4.4.2 Subharmonic Onset Patterns

At the onset of subharmonic convection striped patterns form. Observed onset states are parallel stripes [Fig. 31(a-b)], stripes with a long wavelength distortion (Fig. 44 & [66]) and spirals [Fig. 31(d)]. Subharmonic stripes possessing a long wavelength distortion are only observed in rotating patterns (Sec. 5.3). Dislocations and convex disclinations are common point defects [67] present near onset [Fig. 31(b-d)]. If giant convex disclinations [Fig. 31(c)] or giant spirals [Fig. 31(d)] form at onset they are typically centered about the experiment mid point and may move off center as the system begins to move away from onset. In the majority of cases, the onset planform is parallel stripes. However, giant convex disclinations are also common near onset, while cell filling concave disclinations are not observed. All point defects may be described as the composite of two topological types: concave and convex. A disclination is the place where the pattern director field is undetermined. At subharmonic onset only convex disclinations are observed. Cell filling subharmonic spirals are present with increased side wall forcing and observed only when targets and spirals are the harmonic onset planform. However, subharmonic spirals are unusual even when targets are the harmonic onset planform. Due to the characteristic wave length of subharmonic patterns being substantially smaller than that of harmonic patterns it might be expected that side wall forcing would have less of an influence over the selected planform. Only one and three arm giant subharmonic spirals are observed. Hexagons are not observed anywhere along the subharmonic marginal stability curve. While violations of the spatial (Boussinesq) inversion symmetry resulted in harmonic hexagons at similar  $R$  numbers, subharmonic modes must also satisfy time-translation

inversion symmetry which continues to exclude hexagons near onset.

## 4.5 Discussion

Experiments confirm predictions that convection is stabilized by modulation. Results from a linear stability analysis of the equations of motion in the Boussinesq approximation are in qualitative agreement with the predictions reported by other authors [35, 50, 52, 53]. Experiments quantitatively agree with linear stability for the onset of both harmonic and subharmonic convection. No evidence of hysteresis is experimentally observed at the onset of convection. In the vicinity of the bicritical point where conduction stability is the most enhanced the temperature difference imposed across the fluid layer is relatively large and it is this large  $\Delta T$  that is responsible for violating the Boussinesq symmetry. At  $\omega = 98.0$  conduction was observed up to  $R = 4553$ .

Conduction is confirmed to become unstable to fluid motion displaying two distinct wave numbers:  $q^H$  and  $q^S$ . For  $R \lesssim 3100$  harmonic onset occurs to stripes or targets [Fig. 29(a)], while for larger  $R$  patterns display regions of coexisting hexagons like those shown in Fig. 29(c-d). The global  $q^H$  of these patterns is relatively constant with increasing  $\delta Fr$  until relatively close to the stability cusp, in confirmation of the expectations from linear stability. Subharmonic onset occurs to stripes, though convex disclinations are often observed [Figs. 26(a,b,d) & 31(c)].

Fluid motion was shown to occur in harmonic and subharmonic resonance to  $\omega$ . The temperature field is predicted for harmonic convection to oscillate with a period of  $\tau$  about nonzero mean, while for subharmonic flows it is expected to oscillate

with a period of  $2\tau$  about zero mean. Recording shadowgraphic images at half the modulation period  $\frac{\tau}{2}$  laboratory observations confirmed these predictions.

# CHAPTER 5

## Observations

In addition to confirming predictions made in the existing literature this dissertation examines patterns and transitions over a wide parameter range, revealing several novel characteristics of acceleration modulated Rayleigh-Bénard convection. Appendices A & B are reprints of two *Physical Review Letters* [66, 68] that summarize significant aspects of the results reported in this Chapter. Throughout this chapter frequent reference will be made to these appendices and the included figures.

This chapter will begin by describing the patterns observed as parameters are changed to move the fluid away from onset and into the region of harmonically modulated convection (Sec. 5.1.1). It will be shown that the observed purely harmonic patterns and transitions between them are typical of those found in classical (unmodulated) Rayleigh-Bénard convection. Numerical solutions of the Oberbeck-Boussinesq equations [Eqs. (13)] at the appropriate parameter values reproduce laboratory observations. Next, adjusting parameters to move away from the subharmonic onset typical examples displaying purely subharmonic modulation will be presented (Sec. 5.1.2).

For sufficiently large  $R$  conduction is not stable for any  $\delta Fr$  and experiments find a gradual transition between purely harmonic and purely subharmonic patterns

through a region of harmonic-subharmonic coexistence. The experimental boundaries defining the coexistence region track the conduction marginal stability curves well into the convection regime. Patterns on both sides of the pure harmonic-coexistence and pure subharmonic-coexistence boundaries are discussed in Secs. 5.2.1 & 5.2.2, respectively. Spectral measures are used to characterize a typical pass through coexistence at constant  $R$  and varying  $\delta Fr$ . Numerical solutions of the Oberbeck-Boussinesq equations [Eqs. (13)] reproduce both the pure patterns and coexistence states near the coexistence boundaries. Pattern rotations observed in experiments, but not in numerics, are described in Sec. 5.3. While these rotations are found to be influenced by the magnitude of lateral drive shaft vibrations pattern rotations have the curious property that harmonic and subharmonic modes always rotate in opposite directions. Next (Sec. 5.4), observations of complex-ordered patterns are reported in both experimental and numerical trials. The transition to these exotic states from various parameter directions is considered. Experiments probing these transitions suggest interactions between the stimulated modes are involved in the pattern formation. In Sec. 5.4.3 a mechanism that is qualitatively different than the resonant triads used to explain the formation of superlattices and quasipatterns in other pattern forming systems is proposed. The roles of system symmetries in planform selection are discussed and violations of the Boussinesq symmetry are found to explain differences between the experimental and numerical results in the vicinity of the bicritical point. Finally, in Sec. 5.4.4 the sensitive wave number dependence of  $q_c^S$  on  $\omega$  for  $Pr \approx 1$  fluids is used to investigate changes in complex-ordered structure as the separation between  $q_c^H$  &  $q_c^S$  is varied. Several other novel complex-ordered patterns are reported, all of which are found to satisfy the formation mechanism proposed in Sec. 5.4.3.

## 5.1 Observed Patterns

A rich variety of patterns which may display one of two distinct characteristic lengths and associated time scales (pure states) are observed in the convection regime. In Chapter 4 the onset of these patterns was considered and it was found that harmonic patterns occur for relatively smaller values of the modulation parameters, while subharmonic patterns are found at relatively larger values of the modulation parameters. Harmonic states and the transitions between these patterns are typical of those patterns observed in unmodulated Rayleigh-Bénard convection studies. These include parallel stripes, multi-foci stripes, multi-arm spirals, and spiral defect chaos away from onset. Purely harmonic responding patterns are composed of the larger length scale, while the length scale for purely subharmonic patterns is significantly smaller. Typical subharmonic patterns are a striped base state that may contain defects including disclinations, dislocations, grain boundaries, and cross-rolls. Additionally, subharmonic stripes are found to possess transverse modulations over a range of parameters away from onset. Beyond the transverse modulated stripes, relatively far from onset, subharmonic patterns lose all discernible structure.

### 5.1.1 Harmonic Patterns

Harmonic onset patterns (see Sec. 4.3.2) undergo a transition to spiral defect chaos as the system moves further into the convection regime by combinations of decreasing  $\delta Fr$  and increasing  $R$  at fixed  $Pr$  and  $\omega$  (Fig. 32). Domains of hexagons observed near onset at larger  $R$  values are replaced by a cell filling striped state as the system

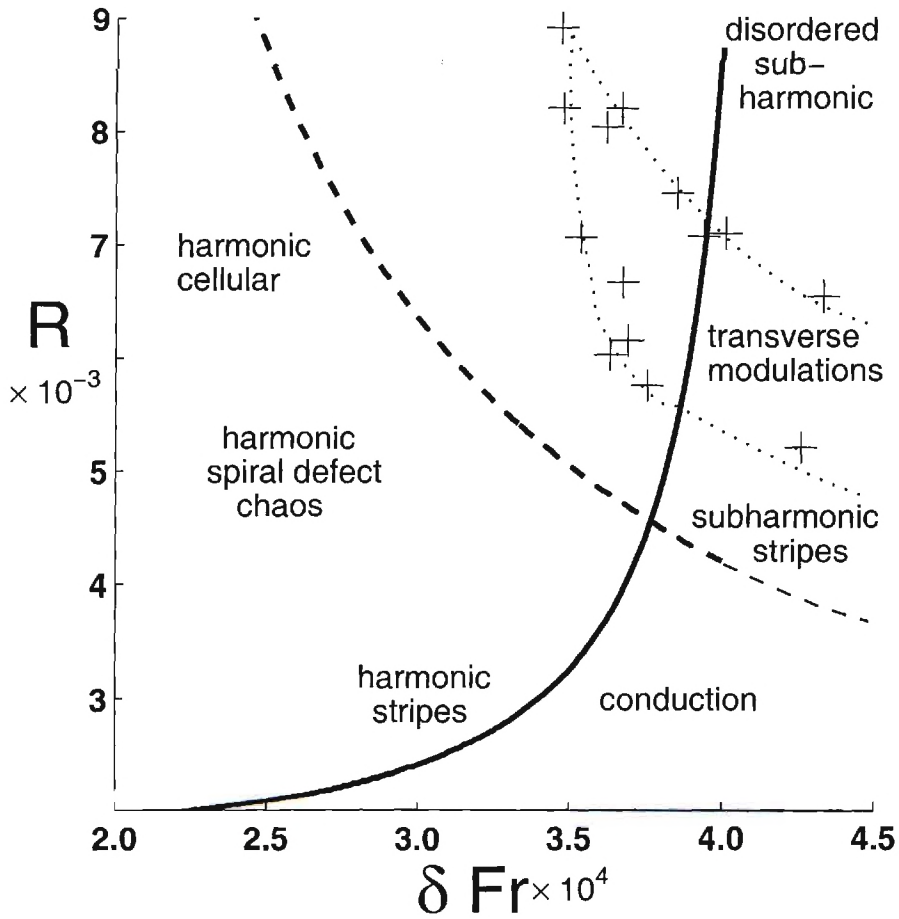


Figure 32: Parameter space showing conduction marginal stability curves for harmonic (solid) and subharmonic (dashed) convection as well as experimentally determined regions of behavior. Experimental measurements of the transverse modulated (see text) subharmonic stripes (+) are fitted with a dotted line to help guide the eye.

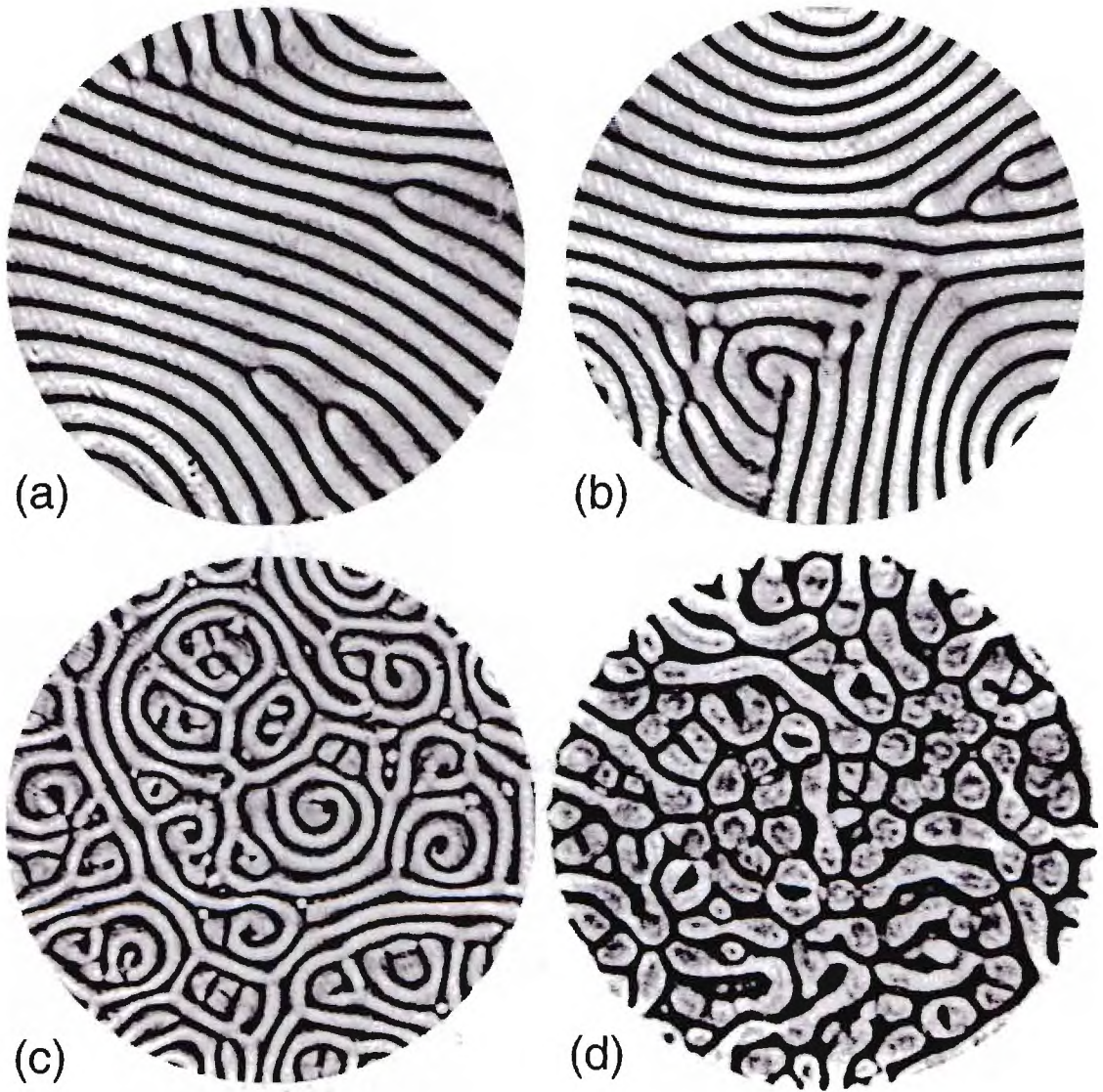


Figure 33: Examples of typical patterns observed moving away from onset stripes: (a) stripes with defects and two wall foci forming ( $\delta Fr = 3.47 \times 10^{-4}$ ,  $\omega = 98.4$ , &  $R = 3820$ ), (b) three foci stripes ( $\delta Fr = 3.36 \times 10^{-4}$ ,  $\omega = 98.4$ , &  $R = 3830$ ), (c) spiral defect chaos ( $\delta Fr = 2.06 \times 10^{-4}$ ,  $\omega = 96.2$ , &  $R = 4290$ ), and (d) far from onset cellular patterns ( $\delta Fr = 2.70 \times 10^{-4}$ ,  $\omega = 100.3$ , &  $R = 7920$ .)

begins to move into the convection regime. In the thermally modulated Rayleigh-Bénard experiments of Meyer, Cannell, & Ahlers [39] parallel stripe states were also observed after the mixed stripe-hexagon patterns as the system moved further from onset. Depending on the magnitude of side wall influence this striped state could be parallel stripes (weaker forcing) or giant targets (stronger forcing). Our observations in acceleration modulated Rayleigh-Bénard are consistent with those made by Meyer, Cannell, & Ahlers [39] in thermally modulated Rayleigh-Bénard. In the transition from parallel stripes to spiral defect chaos, stripe's ends become increasingly perpendicular to the lateral side walls creating focus singularities. Initially, two foci will form [Fig. 33(a)] and as the stripe curvature increases patterns similar to the so-called Pan-Am states observed in classical Rayleigh-Bénard convection at comparable  $Pr$  and aspect ratio form. Moving away from onset stripe curvature will gradually increase and more wall foci will emerge [Fig. 33(b)]. As more focus singularities become present, increasing numbers of dislocations and grain boundaries will be found in the pattern interior. Generally, once the number of wall foci is larger than four, spirals will begin to appear in the interior of the pattern (spirals do not typically arise at the boundaries). The system will then begin to display spiral defect chaos composed of left and right handed spirals [Fig. 33(c)]. As spiral defect chaos gradually fills the convection cell the power spectrum distribution broadens. However, the increasing  $q^H$  width ( $\sigma^H$ ) is still characterized by a well-defined characteristic  $q$ . For sufficient  $\delta Fr$  and relatively large  $R$  values the characteristic  $q$  becomes less well-defined,  $\sigma^H$  becomes large as spiral defect chaos gradually gives way to patterns qualitatively similar to Fig. 33(d), composed of cellular structures and some stripe sections without spirals. The emergence of dislocations and grain boundaries, focus singularities

and the increasing of  $\sigma^H$  about a characteristic  $q$  observed in the transition from stripes to spiral defect chaos in harmonic patterns is the same as reported in classical *Rayleigh-Bénard* [69, 65].

When the side wall influence is more substantial the onset striped pattern is a target and the transition to spiral defect chaos is somewhat different from the transition from parallel stripes. Moving away from onset targets typically lose stability as a dislocation which may be nucleated at the side walls translates radially to the target center (core), resulting in the formation of a one arm spiral. Moving away from onset a defect mediated transition from targets to spirals occurs (Fig. 34). Pairs of defects emerge in the pattern due to skew-varicose instabilities [Fig. 34(a & d)]. One defect will translate radially to the spiral core producing a one arm spiral, while the other defect will translate radially to the side walls and be annihilated [Fig. 34(b)]. In Figs. 34(b) & 35(a) the defect pairs originate due to a skew-varicose instabilities which result in one arm spirals and targets. Sufficiently near onset this mechanism can result in continuous switching between targets and one arm spirals (Fig. 34). Continuing away from onset additional defects enter the pattern due to skew-varicose instabilities producing multi arm spirals, as many as six arm spirals being observed. Occasionally, an additional instability results in the targets or spirals cores moving off-center. An example of this off-center instability is shown in Fig. 35(b-c) for a three arm spiral. As the fluid moves away from onset skew-varicose and off-center instabilities result in numerous defects throughout the pattern and the spiral will become unstable as spiral defect chaos [Fig. 35(d)] forms. The defect mediated transition from cell filling targets to spirals and off-center motion of spiral centers during the gradual transition to spiral defect chaos (which contains numerous smaller spirals) has been reported in

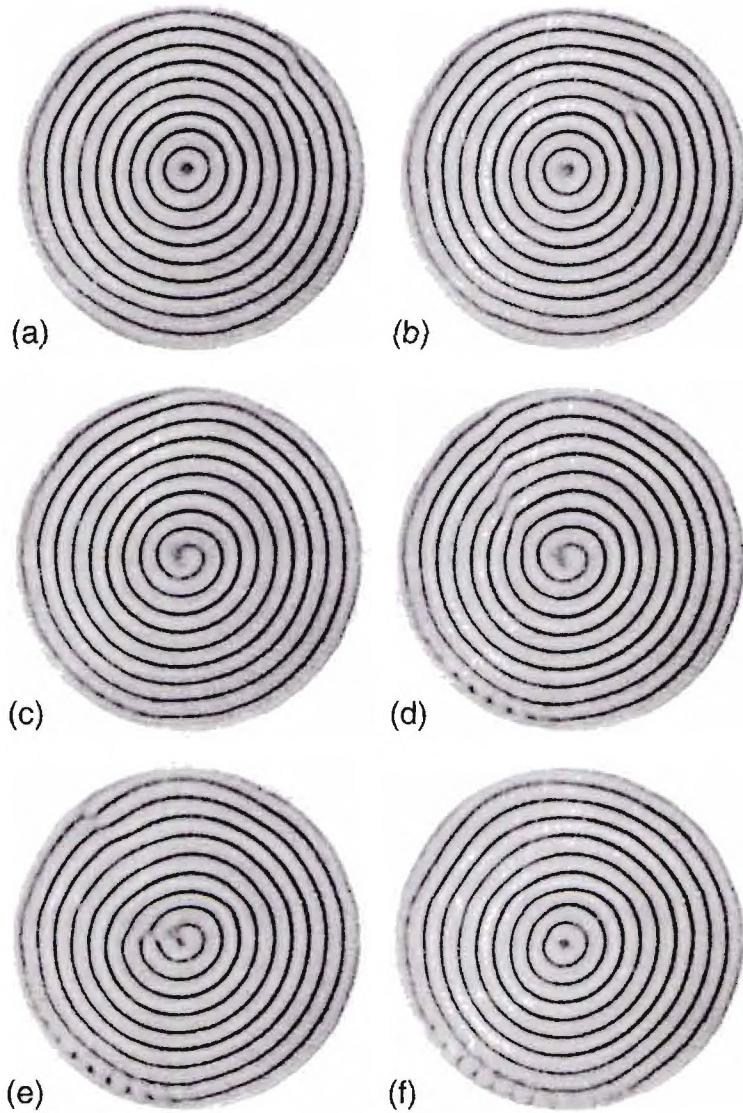


Figure 34: Examples of dislocation pairs due to skew-varicose instabilities mediating oscillations between targets and one-arm spirals. Images are separated in time (in seconds) at the same parameters ( $\delta Fr = 1.74 \times 10^{-4}$ ,  $\omega = 98.4$ , &  $R = 2480$ ): (a)  $t = 0$ , (b)  $t = 10$ , (c)  $t = 30$ , (d)  $t = 40$ , (e)  $t = 45$ , & (f)  $t = 60$ .

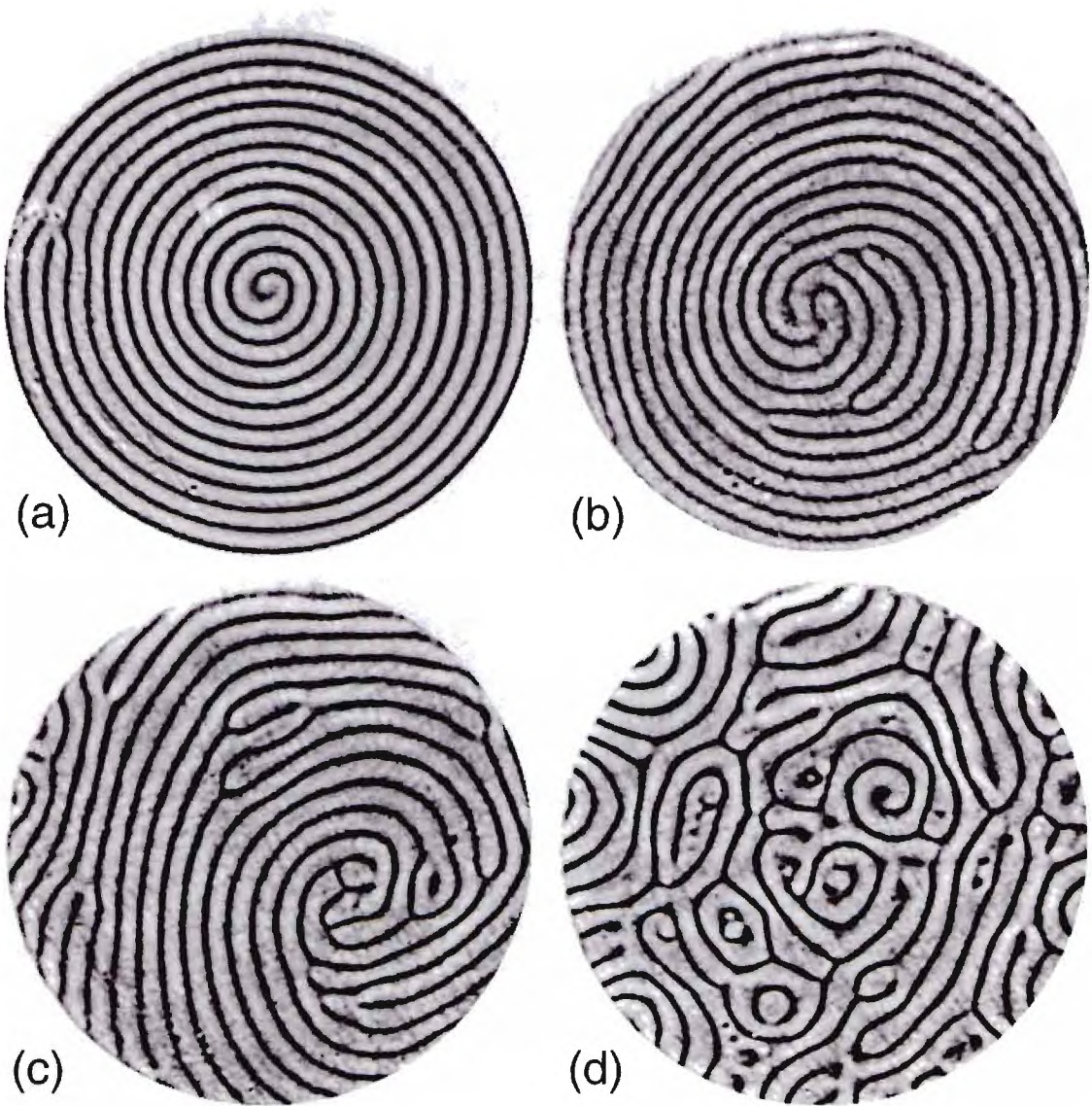


Figure 35: Examples of typical patterns observed moving away from onset target: (a) one arm spiral ( $\delta Fr = 1.74 \times 10^{-4}$ ,  $\omega = 98.4$ , &  $R = 2480$ ), (b) multi-arm spiral ( $\delta Fr = 1.95 \times 10^{-4}$ ,  $\omega = 99.4$ , &  $R = 2420$ ), (c) off-center multi-arm spiral ( $\delta Fr = 2.26 \times 10^{-4}$ ,  $\omega = 99.0$ , &  $R = 2940$ ), and (d) spiral defect chaos ( $\delta Fr = 2.30 \times 10^{-4}$ ,  $\omega = 98.5$ , &  $R = 3660$ .)

classical Rayleigh-Bénard convection studies [70].

### 5.1.2 Subharmonic Patterns

Moving away from subharmonic onset (Sec. 4.4.2) patterns always form a parallel stripe state. Point defects that cause convex disclinations or spirals may persist near onset but will not be stable far from onset due to dislocations or an off-center instability. Away from onset, stripe states include dislocations and cross-roll defects. As a convex disclination becomes unstable dislocations propagate from the side walls to the core where the dislocations annihilate with a stripe in the core, often resulting in an adjustment in local wave number by a series of cross-roll defects on the stripes emanating from the core. Further away from onset, subharmonic stripe ends begin to align perpendicular to the side walls; a characteristic similar to the harmonic stripes. These states [Fig. 31(a)] may contain several dislocations and focal singularities. While subharmonic patterns may display several side wall foci and numerous defects, spirals or something similar to spiral defect chaos is not observed. Patterns of these types lie in the parameter region labeled subharmonic stripes in Fig. 32.

As  $\delta Fr$  and  $R$  increase stripes become more complex. Moving away from onset striped patterns, which typically contain two or three foci, transverse modulation [Fig. 36(b)] abruptly (Fig. 32) occurs throughout the patterns. These modulations appear as waves which propagate down the length of the stripes. Modulations on the individual stripes are correlated with distinguishable wave fronts observed to propagate across the pattern. Prior to the emergence of transverse modulations the pattern in Fig. 36(b) is stripes with three side wall foci. That striped pattern remains in Fig. 36(b) as the base state. At the intersection of stripes about the three foci

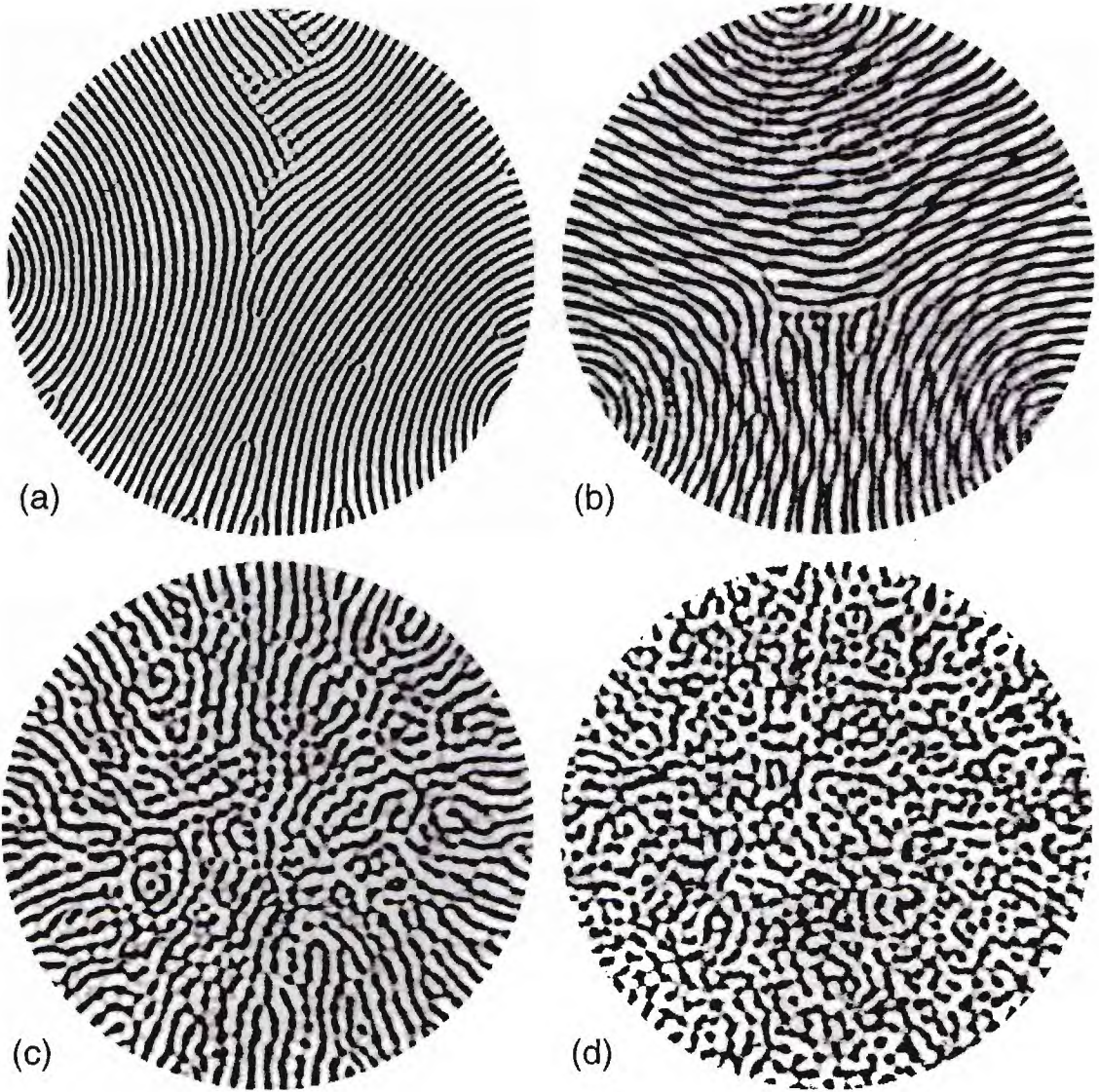


Figure 36: Examples of typical subharmonic patterns observed away from onset: (a) two foci stripes with defects ( $\delta Fr = 4.17 \times 10^{-4}$ ,  $\omega = 98.1$ , &  $R = 4888$ ), (b) three foci transverse modulated stripes ( $\delta Fr = 4.01 \times 10^{-4}$ ,  $\omega = 98.0$ , &  $R = 6552$ ), radial stripes - onset of subharmonic disorder ( $\delta Fr = 4.83 \times 10^{-4}$ ,  $\omega = 95.0$ , &  $R = 6120$ ), and (d) subharmonic disorder ( $\delta Fr = 4.60 \times 10^{-4}$ ,  $\omega = 95.0$ , &  $R = 7670$ .)

is an amplitude grain boundary; stripes about the lower two foci in this pattern terminate perpendicular to the stripes about the upper foci near the pattern center. Along the boundary between transverse modulated and disordered flows (Fig. 32) the subharmonic striped base state breaks down and stripes stretch radially from the center to the lateral side walls [Fig. 36(c)]. Near the center of these patterns coherent structure breaks down. Sufficiently far from onset the fragmented state nucleated in the interior occurs throughout the convection cell as a state like Fig. 36(d) forms.

## 5.2 Direct Harmonic-Subharmonic Transition

Considering the direct transition from purely harmonic convection to purely subharmonic convection which can occur when  $R$  is sufficiently large that conduction is no longer expected to be stable for any  $\delta Fr$  (Fig. 32) reveals several novel aspects of acceleration modulated Rayleigh-Bénard convection. First, the transition between pure harmonic and pure subharmonic flows is not abrupt, but occurs through a parameter regime where both responses coexist. Second, conduction marginal stability predictions roughly define the parameter range of harmonic-subharmonic coexistence, despite the system being well into the convection regime and away from the expected validity of linear stability predictions. Third, the transition between pure harmonic and coexistence is qualitatively different from the transition between pure subharmonic and coexistence. Lastly, several novel two scale patterns composed of harmonic and subharmonic components are found. Numerical solutions of the equations of motion in the Boussinesq approximation reproduce experimental observations.

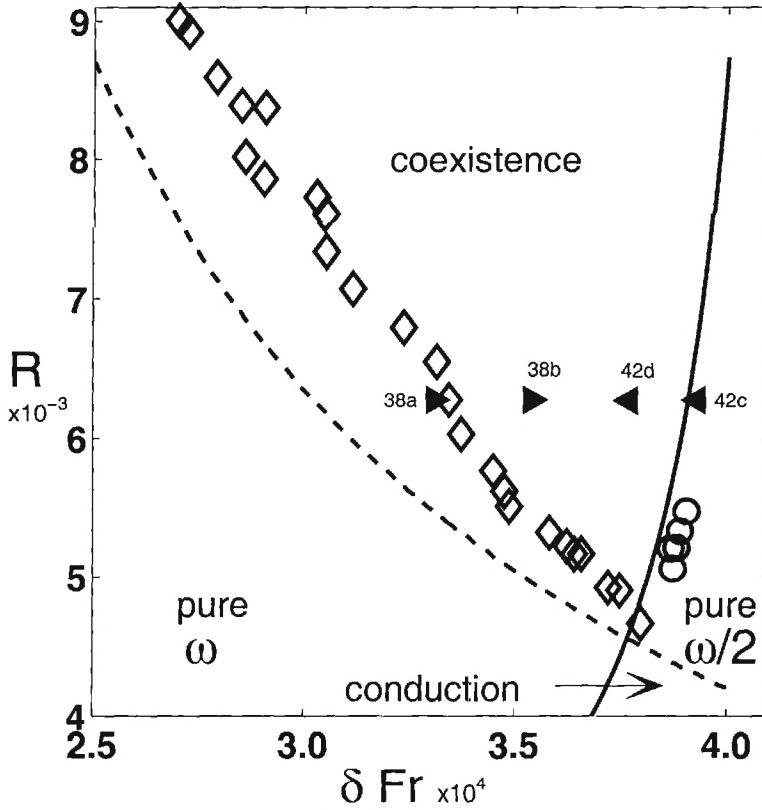


Figure 37: Phase plane comparing the experimentally measured coexistence onset to the marginal stability curves for conduction. Boundary between coexistent and purely harmonic flows ( $\diamond$ ) follows the marginal subharmonic ( $\omega/2$ ) curve (dashed line), while the boundary between coexistent and purely subharmonic patterns ( $\circ$ ) tracks the marginal harmonic ( $\omega$ ) curve as far as the boundary can be reliably determined. Filled in triangles are the locations of patterns in Figs. 38 & 42.

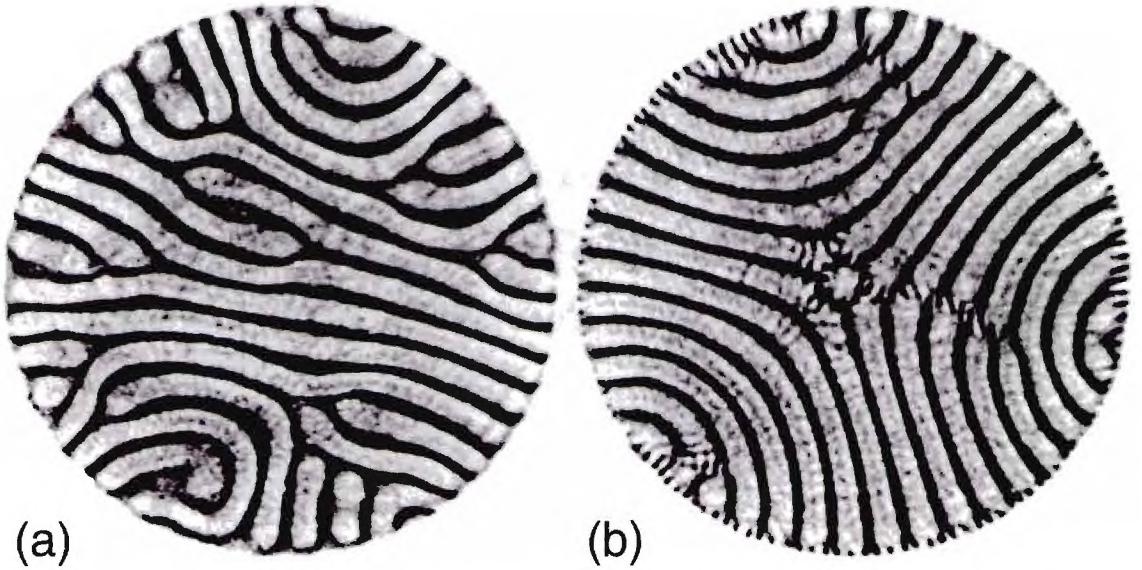


Figure 38: Patterns (*experiments*) on either side of the purely harmonic-coexistence boundary. Pure harmonic stripes (a) with defects ( $\delta Fr = 3.31 \times 10^{-4}$ ,  $\omega = 98.0$ , &  $R = 6280$ ). Coexistence state (b) with 3-foci harmonic stripes and subharmonic stripe patches ( $\delta Fr = 3.54 \times 10^{-4}$ ,  $\omega = 98.0$ , &  $R = 6280$ ).

### 5.2.1 Transition Between Pure Harmonic and Coexistence Patterns

Purely harmonic patterns lose stability to coexisting states with localized regions of subharmonic stripes (Fig. 37). Prior to the boundary with coexistence, the harmonic pattern typically consists of parallel stripes with defects [Fig. 38(a)] or a more irregular cellular pattern [Fig. 33(d)]. With increasing  $\delta Fr$  at constant  $R$ , localized domains of subharmonic stripes emerge with a characteristic wavenumber  $q^S \approx 3q^H$ . These subharmonic domains are typically either centered about defects in the harmonic pattern or aligned perpendicular to the lateral boundaries [Fig. 38(b)]. Subharmonic stripes at the lateral boundary remain pinned to the boundary and do

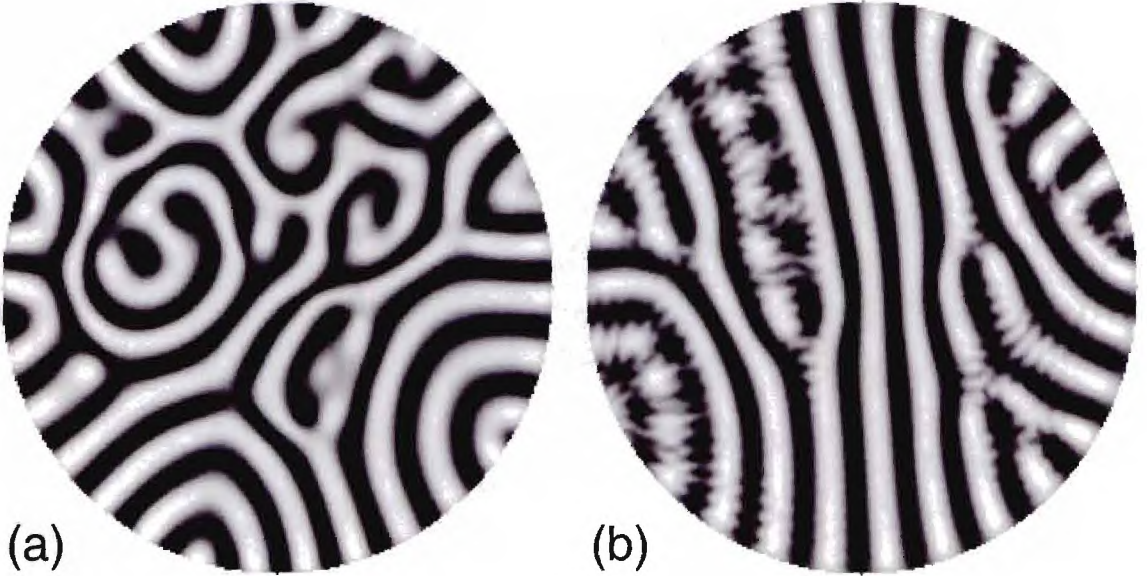


Figure 39: Patterns (*simulations*) on either side pure harmonic-coexistence boundary displaying (a) multiple side-wall singularities ( $\delta Fr = 3.28 \times 10^{-4}$ ,  $\omega = 98.0$ , &  $R = 6600$ ) and (b) the same kind of localized subharmonic patches as observed in the experiments [Fig. 38(b)].

not advect into the interior. In the pattern interior harmonic defects continually nucleate, advect and annihilate. Associated with the harmonic defects are subharmonic patches, which continually appear, move and disappear. Although harmonic defects are virtually always present for parameter values near the pure harmonic-coexistence boundary, not all harmonic defects have associated subharmonics. As a result, near onset, the subharmonic stripe patches are intermittent in time as well as space. Because of this intermittency, the onset of subharmonics is difficult to detect in spatial power spectra [Fig. 40(a-b)]. Detection of the onset of these intermittent states is most reliably performed using the real space images of the patterns. The onset value of  $\delta Fr$  for a given  $R$  corresponds to the presence of subharmonic patches in the pattern interior for 10% of the observation time (Fig. 37).

Our results provide evidence that harmonic patterns have an inhibitory effect on the emergence of subharmonic patterns. In the first place, the boundary for convective onset in the experiments lies above the subharmonic marginal stability curve over the entire experimentally accessible range of parameters (Fig. 37). In other words, the subharmonic onset is delayed relative to the linear theory predictions of onset from the conduction state. Furthermore, subharmonics always appear in regions of where the harmonic flows are weaker, namely in the cores of defects amplitude of convection flow is reduced [71].

The subharmonic component of coexisting convection remains localized and spatially intermittent even as  $\delta Fr$  is increased (with  $R$  fixed) to move the system well away from onset (Fig. 41). This type of behavior is confirmed in the simulations. The subharmonic component is spectrally indistinguishable from the background noise and the second harmonic of  $q^H$  over a wide range of  $\delta Fr$  [Figs. 41 & 40(a-b)]. The wavenumber of the harmonic modes  $q^H$  remains relatively fixed [Fig. 41(b)]. The spectral width  $\sigma^H$  decreases [Fig. 41(c)] due to the harmonic pattern becoming more ordered as the number of harmonic defects present near the onset of coexistence [Fig. 38(a)] reduces significantly as the system moves further from onset into the coexistence regime [Fig. 38(b)]. Simulations reproduce the qualitative features and  $\delta Fr$  dependence (Fig. 39). In the coexistence region the subharmonic pattern component will gradually increase with  $\delta Fr$ , although it will not become distinguishable from background noise till the subharmonic contribution abruptly grows towards the coexistence region mid point in  $\delta Fr$  (Sec. 5.4).

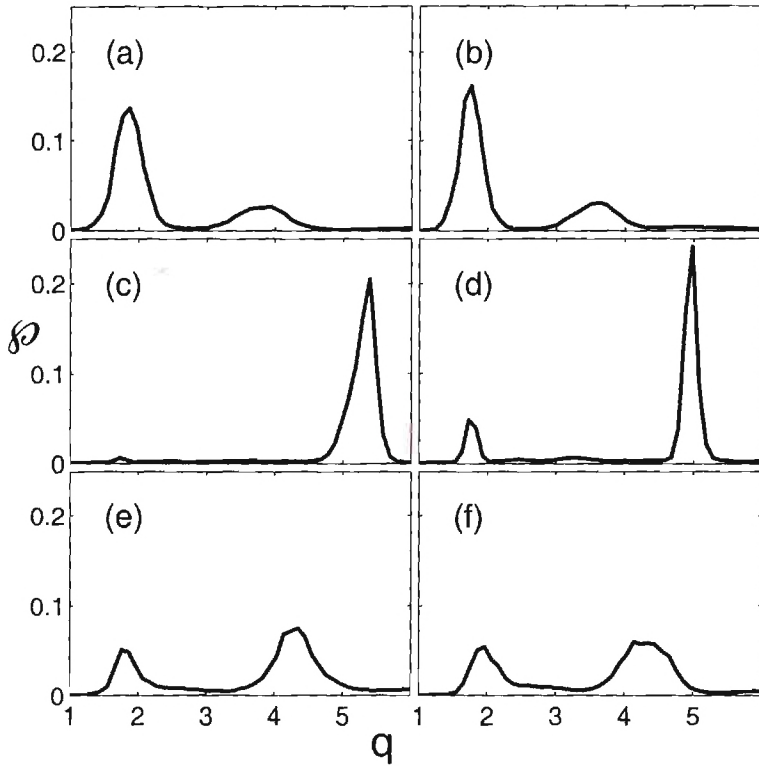


Figure 40: Azimuthally averaged power spectra for six different experimental conditions from the transition between pure harmonic convection and pure subharmonic convection, passing through a region of coexisting harmonic-subharmonic convection. Representative images from each data point are shown in other figures: (a) in Fig. 38(a), (b) in Fig. 38(b), (c) in Fig. 42(a), (d) in Fig. 42(b), (e) in Fig. 42(c), and (f) in Fig. 42(d).

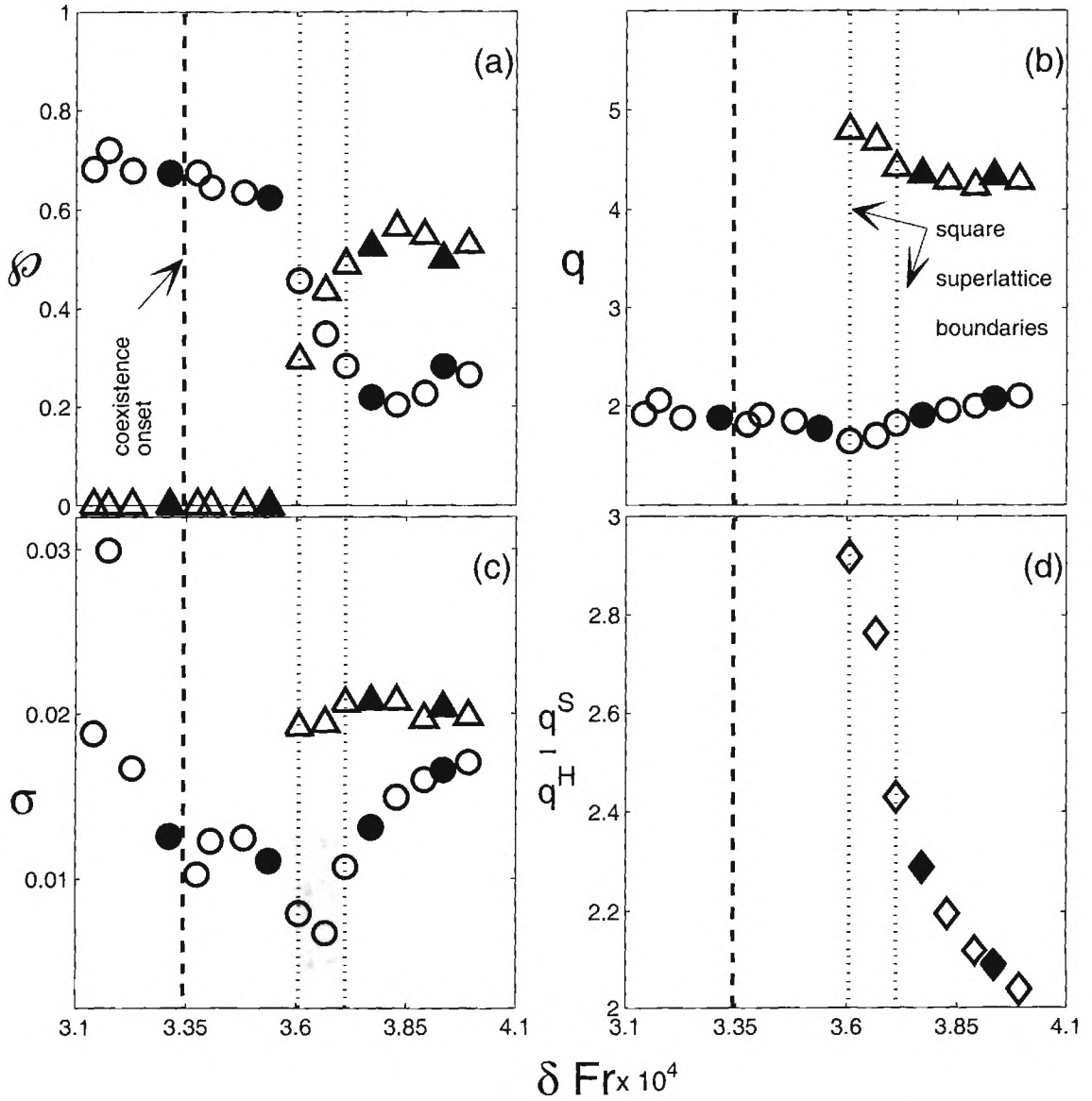


Figure 41: Spatial spectral analysis of the transition from pure harmonic convection to pure subharmonic convection, passing through a region of coexisting harmonic-subharmonic convection with increasing  $\delta Fr$  at  $R = 6280 \pm 10$ . The azimuthally averaged spectra for both the harmonic and subharmonic modes are characterized by (a) the spectral power in each mode  $\phi^H$  &  $\phi^S$ , (b) the mode wave numbers  $q^H$  &  $q^S$ , (c) the widths of the spectral peaks  $\sigma^H$  &  $\sigma^S$ , and (d) the wavenumber ratio  $\frac{q^H}{q^S}$ . Throughout,  $\circ$  indicates harmonic pattern component and  $\triangle$  the subharmonic pattern component. Filled in symbols correspond to patterns shown in Figs. 38 & 42.

## 5.2.2 Transition Between Pure Subharmonics and Coexistence Patterns

The transition between purely subharmonic states and coexisting patterns is qualitatively different from the transition between pure harmonic and coexistence states. Pure subharmonic patterns lose stability to coexisting states where the harmonic component emerges globally; no localized states are observed. For  $\omega = 98$ , we consider two cases: (1)  $R_{2c} < R < 5500$  and (2)  $R > 5500$

For  $R_{2c} < R \lesssim 5500$  the coexistence regime competes with pure subharmonic parallel stripes [Fig. 42(a)]. Slowly decreasing  $\delta Fr$  at constant  $R$  a harmonic pattern component emerges at a well-defined location in parameter and begins to be present throughout the pattern [Fig. 42(b)]. Although the harmonic component is weak at onset, the transition is well-defined and readily detectable in Fourier space by looking for the initial presence of power at  $q^H$  [Figs. 40(c-d)]. Typically, the emerging harmonic component is parallel stripes [Fig. 42(b)] which may display domains with several orientations. In this parameter range, the transition is well-predicted by the *conduction* marginal stability curve (Fig. 37), suggesting that the onset of large length scale harmonic convection is neither enhanced nor suppressed by the presence of short length scale subharmonic flows. Hysteresis is not experimentally observed in the transition between pure subharmonic flows and the coexistence regime.

For  $R_{2c} < R \lesssim 5500$  the coexistence states compete with more complex pure subharmonic flows. For  $5500 \lesssim R \lesssim 7000$ , subharmonics with transverse modulations are found when  $\delta Fr$  is large [Fig. 42(c)]. For  $R \gtrsim 7000$ , the subharmonic flows are more disordered. As  $\delta Fr$  is decreased at constant  $R$  and crosses the conduction marginal

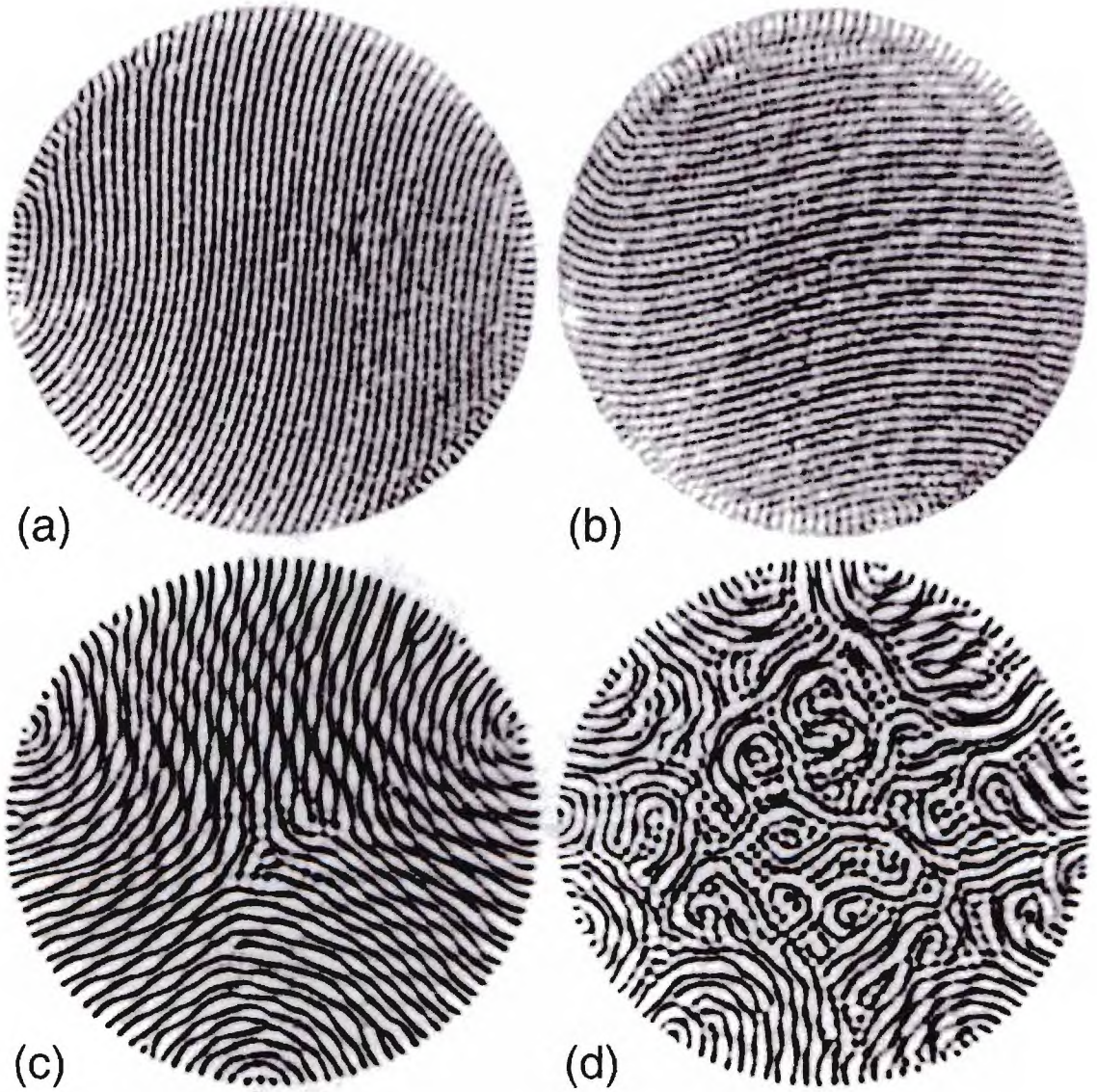


Figure 42: Patterns (*experiments*) on either side of the harmonic-coexistence marginal stability curve ( $Pr = 0.930$ ,  $\omega = 98.0$ ) for  $R = 4982$  [ $\delta Fr = 3.80 \times 10^{-4}$  (a) &  $\delta Fr = 3.69 \times 10^{-4}$ (b)] and  $R = 6275$  [ $\delta Fr = 3.93 \times 10^{-4}$ (c) &  $\delta Fr = 3.77 \times 10^{-4}$  (d)].

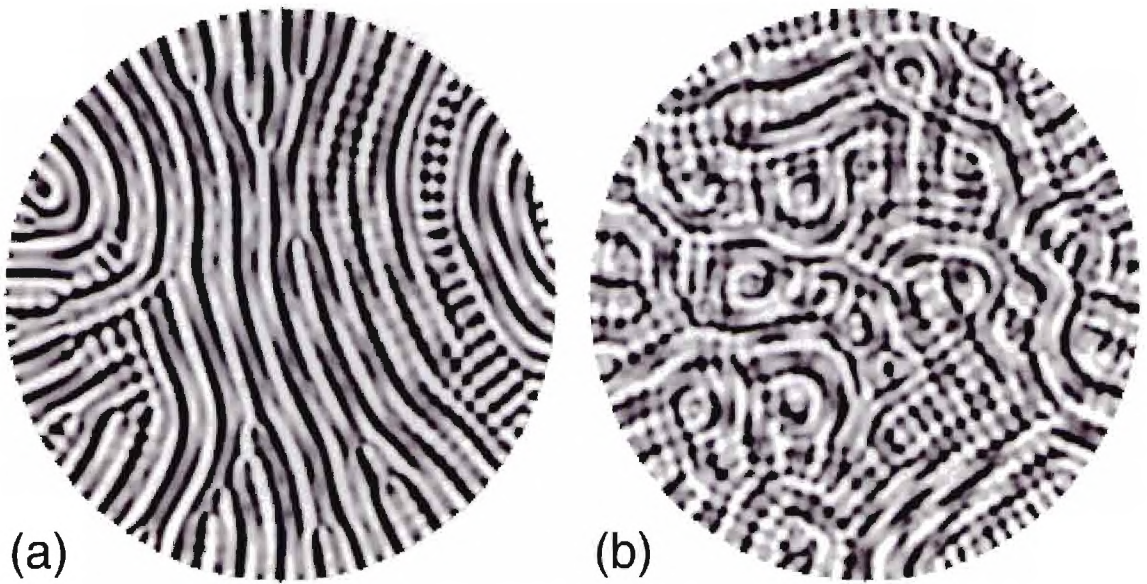


Figure 43: Patterns (*simulations*) on either side pure subharmonic-coexistence boundary displaying (a) transverse modulated subharmonic stripes & cross-rolls ( $\delta Fr = 4.373 \times 10^{-4}$ ,  $\omega = 98$ , &  $R = 6800$ ) and (b) a similar state broken into domains ( $\delta Fr = 3.957 \times 10^{-4}$ ,  $\omega = 98$ , &  $R = 6800$ ).

stability boundary, the flow structure changes gradually to patterns like that shown in Fig. 42(d). In all cases, these states are difficult to distinguish spectrally because patterns contain spectral peaks with similar power content at wave numbers corresponding to both  $q^S$  and  $q^H$  [Figs. 40(e-f)]. As a result, the onset of the coexistence regime from pure subharmonics is ill-defined for this range of  $R$ .

Spectral analysis demonstrates that the gradual nature of the transition from pure subharmonics to coexisting patterns continues as  $\delta Fr$  is further decreased. For  $R \lesssim 5500$  the growing harmonic stripes have little effect on the subharmonic stripes as the two components are simply superimposed. For  $5500 \lesssim R \lesssim 7000$  the subharmonic striped base state that supports the transverse modulations gradually breaks down as numerous domains form [Figs. 42(c-d)]. Typically, these domains nucleate in the pattern interior and spread to fill the pattern with decreasing  $\delta Fr$ . These patterns are reproduced in simulations [Fig. 43(b)]. For  $R \gtrsim 7000$  the structurally disordered state [Fig. 36(d)] becomes more ordered with decreasing  $\delta Fr$ . Regardless of the  $R$  value the spectral measures display similar trends. First, relative power in  $\wp^S$  gradually decreases and  $\wp^H$  slowly increases as the harmonic pattern becomes more significant [Fig. 41(a)]; eventually reaching the point where  $\wp^S$  contributes  $\lesssim 60\%$ . Second,  $q^H$  [Fig. 41(b)] remains relatively fixed while  $\sigma^H$  decreases [Fig. 41(c)]. Simultaneously,  $q^S$  slowly increases while  $\sigma^S$  remains relatively fixed. These similarities indicate that as the pattern passes further into coexistence by decreasing  $\delta Fr$  the harmonic pattern slowly grows and becomes more regular while the subharmonic component slowly loses power and increases  $q^S$ .

### 5.3 Pattern Rotation

Patterns may display solid-body constant rate rotations with the property that harmonic and subharmonic modes always rotate in opposite directions (Fig. 59 - App. A). As reported with the initial experimental results for acceleration modulated Rayleigh-Bénard convection [66], patterns possess solid-body rotations for sufficiently large  $\delta Fr$ . Pure harmonic and pure subharmonic patterns can rotate in either direction at rates which slowly increase in magnitude with  $\delta Fr$  [Fig. 59(c)], except very near to conduction where rotations abruptly slow as patterns weaken. Also, pure harmonic and pure subharmonic patterns always rotate in opposite directions during any given experimental trial [Figs. 59(a) & 59(b)]. Pure patterns are found to rotate in either direction, but once a rotation direction is selected by a pure pattern it is usually maintained by modes displaying the same temporal response, while modes of the other temporal response will rotate in the opposite direction. The rotation direction displayed by pure patterns is not found to be evenly distributed between the two possible directions during distinct experiments. Instead, harmonic modes prefer the counterclockwise direction. In 84% of the 62 previously reported [66] experiments harmonic patterns rotated in the counterclockwise direction. Subsequent experiments confirm the initial observations and additionally indicate the reverse symmetry in rotation directions between harmonic and subharmonic modes is maintained in coexisting patterns. Rotation directions and rates of both pure and coexisting patterns are determined in the spectral domain by comparing power spectra from successive patterns separated by a time interval. The rotation angle is the relative rotation between successive spectra which maximizes the correlation between the spectra. For

the case of coexisting patterns the harmonic and subharmonic components are treated separately by filtering out the other temporal response in the frequency domain.

Experiments suggest pattern rotation is driven by weak horizontal vibration. As previously reported [66] various minor modifications to the first shaking configuration (Sec. 3.2), including tilting the apparatus  $\approx 5^\circ$  off the vertical, changing the side wall symmetry from circular to square as well as asymmetric cooling of the top plate have little effect on pattern rotations. However, when the lateral vibration is on the order of 2% of the displacement amplitude, patterns display global rotations at dimensionless rates of  $\approx 0.1$  [Fig. 59(c)]. These lateral vibrations cause maximum horizontal acceleration magnitudes of  $\approx 0.1g$ , where  $g$  is the gravitational acceleration. By including a rectangular drive shaft and air-bearing in the second shaker configuration (Sec. 3.2) the magnitude of lateral vibrations is reduced to less than 0.2% of the displacement amplitude and mechanical rotations of the drive shaft are eliminated. Correspondingly, the maximum horizontal accelerations are reduced to no more than about  $0.02g$ . Sequences of images recorded over 40,000 drive oscillation cycles indicate that patterns present when using the second shaker do rotate and maintain the reverse direction symmetry between harmonic and subharmonic modes. However, the dimensionless rotation rate is less than 0.001 and rotations are not discernible on the typical laboratory observation time scale.

The observed patterns do not vary significantly with rotation rate. Examining patterns present when using both shakers indicates a dramatic reduction in the rate of the solid-body rotations obvious on typical laboratory time scales when using the first shaker does not alter any of the harmonic states. The subharmonic patterns are also unaffected, with the exception of the long wavelength distortion (Fig. 44)

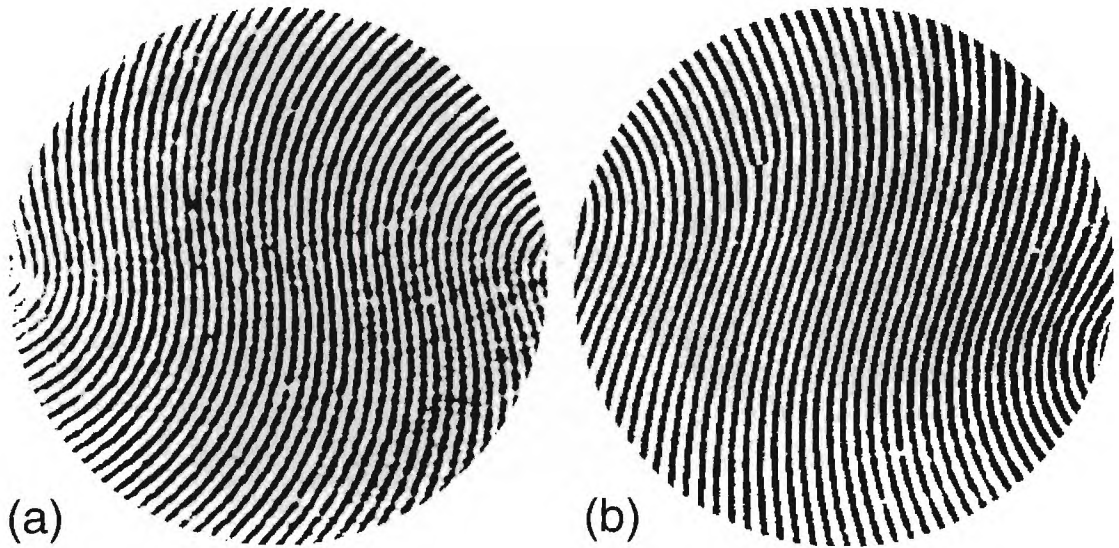


Figure 44: Rotating subharmonic stripes (*experiments*) with a long wave length distortion. Stripes in (a) rotate clockwise ( $\delta Fr = 3.99 \times 10^{-4}$ ,  $\omega = 97.7$ , &  $R = 5195$ ), while the stripes in (b) rotate counter-clockwise ( $\delta Fr = 3.98 \times 10^{-4}$ ,  $\omega = 98.0$ , &  $R = 5317$ ).

present in subharmonic parallel stripes when using the first shaker. The orientation of the distortion is found to change with the rotation direction (Fig. 44). When using the second shaker subharmonic parallel stripes [Fig. 31(b)] do not possess a long wavelength distortion. Similarly, the only changes to coexisting states is the loss of any long wavelength distortion [Fig. 42(b)], if a parallel subharmonic stripe component is present.

## 5.4 Superlattices

When the two wave numbers ( $q^H$  &  $q^S$ ) present in a coexistence pattern make relatively equal contributions, complex-ordered patterns may form. Recall from Sec. 1.1.3

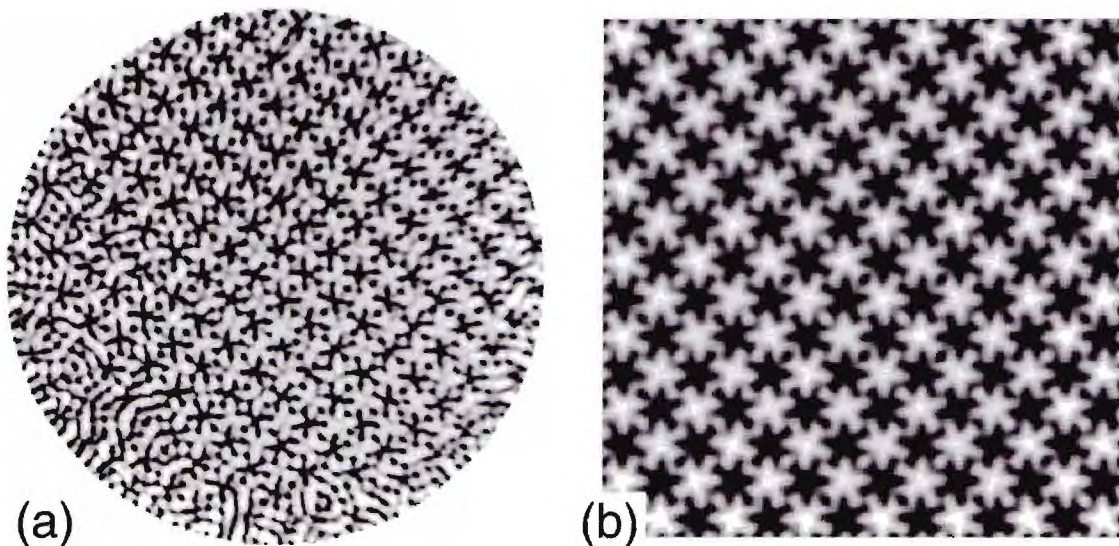


Figure 45: Square superlattices observed in experiments (a) and in numerical simulations (b); both at  $Pr = 0.930$ . In (a)  $\delta Fr = 3.88 \times 10^{-4}$ ,  $\omega = 95.3$ , &  $R = 7028$ , while in (b)  $\delta Fr = 3.75 \times 10^{-4}$ ,  $\omega = 98$ , &  $R = 4750$ .

that complex-ordered states in pattern forming systems have complex spatial structure described by relatively few spectral modes on interacting sublattices. Borrowing from condensed matter terminology complex-ordered patterns in other hydrodynamic and optical pattern forming systems have been designated as quasipatterns or superlattices. If the complex-ordered pattern has a unit cell which covers the plane it is a superlattice, while if it has a unit cell which does not fill the plane it is a quasicrystal. Complex-ordered patterns in acceleration modulated Rayleigh-Bénard share many qualitative features with superlattices. In thermal convection the harmonic lattice typically forms a regular structure that is suggestive of a unit cell. These unit cells are either square (Fig. 45), stripe, rhombic, or hexagonal, all of which would ideally tile the plane. However, the small scale subharmonic components of these patterns remain dynamic and thereby the unit cells do not really repeat. Neither do the unit cells

generally display orientational order with their neighbors, as is the case in quasicrystals. Thereby, in a strict sense complex-ordered patterns in acceleration modulated Rayleigh-Bénard are not the same as the analogous cases in condensed matter, nor in order pattern forming systems. However, the designation of a superlattice does capture many of the complex-ordered patterns features in thermal convection and these patterns will be called superlattices when the underlying harmonic unit cell can tile the plane and the complex-ordered pattern is due to interacting sublattices. Perhaps a more appropriate name would be dynamic superlattices.

Since the unit cell in Fig. 45 is square and spectral analysis to be presented in Sec. 5.4.3 finds these patterns are produced by two interacting sublattices, they will be referred to as *square superlattices*. To the best of my knowledge, the complex-ordered patterns found in this investigation are the first to be reported in convection.

In the remainder of this section experiments and numerics are used to investigate the onset of superlattices, map the superlattice region in the phase plane, identify the role of inversion symmetry in superlattice structure, and propose a mechanism for the formation of these complex-ordered states. The effect of varying the relative wave numbers  $q^S/q^H$ , by changing  $\omega$ , on superlattice structure is also considered briefly.

### 5.4.1 Observations Near Bicriticality

We first consider the transition to superlattices in the experiment beginning from the conduction state at parameter values near bicriticality and increasing  $R$  slowly (Fig. 46). At  $\delta Fr$  slightly less than the experimentally determined bicritical point of  $Pr = 0.930$ ,  $\omega = 94.9$ ,  $\delta Fr_{2c} = 3.91 \times 10^{-4}$ , &  $R = 4640$ , onset occurs to pure regular harmonic hexagons. Slowly increasing  $R$  small localized regions of subharmonic

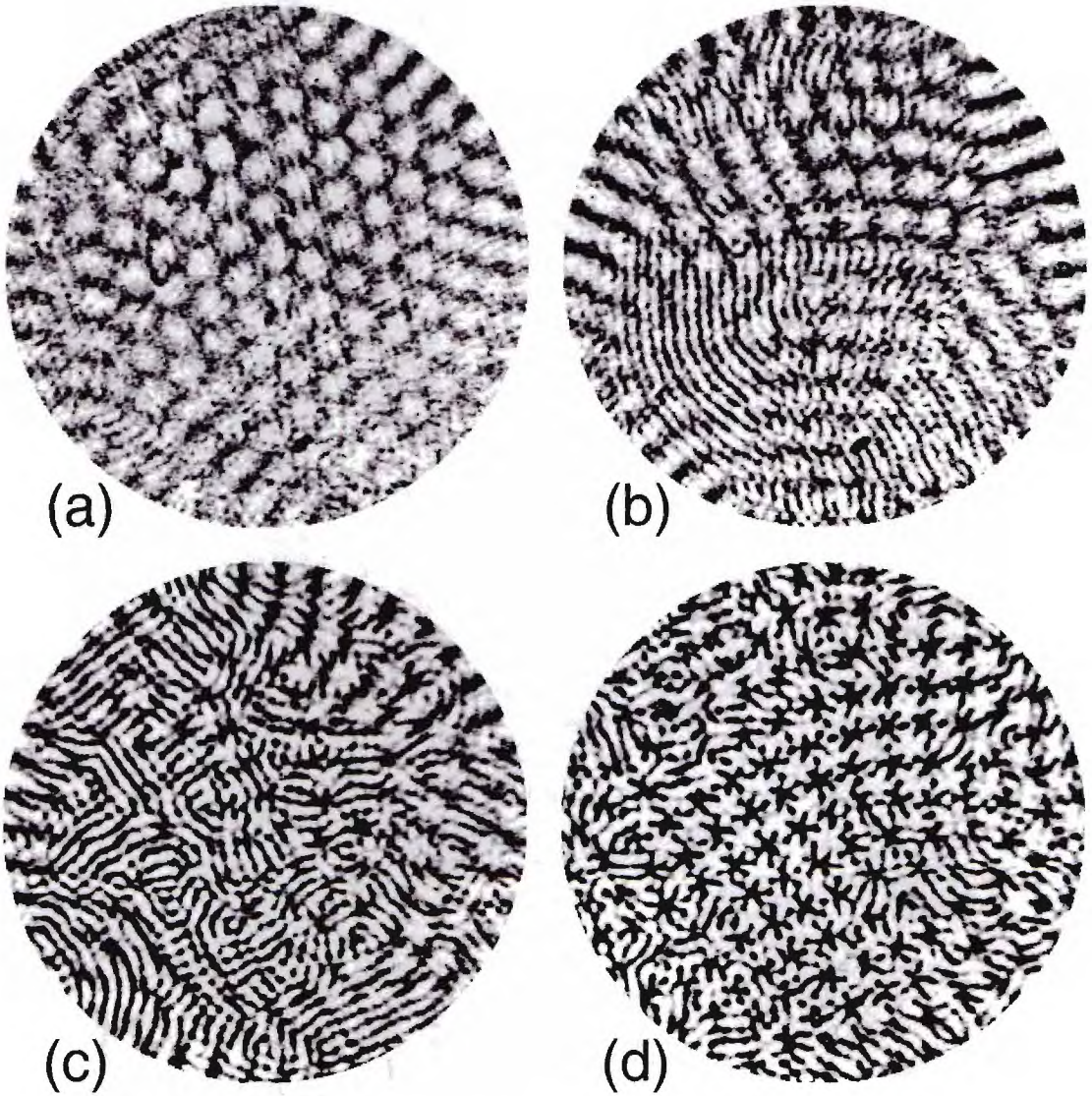


Figure 46: Patterns observed passing from conduction by slowly increasing  $R$  at  $\delta Fr \lesssim \delta Fr_{2c}$ . Corresponding parameters are: (a)  $\delta Fr = 3.89 \times 10^{-4}$ ,  $\omega = 95.0$ , &  $R = 4780$ , (b)  $\delta Fr = 3.88 \times 10^{-4}$ ,  $\omega = 95.1$ , &  $R = 4910$ , (c)  $\delta Fr = 3.88 \times 10^{-4}$ ,  $\omega = 95.0$ , &  $R = 5390$ , and (d)  $\delta Fr = 3.73 \times 10^{-4}$ ,  $\omega = 96.7$ , &  $R = 6270$ .

stripes ( $R \approx 4780$ ) occur on the harmonic hexagons [Fig. 46(a)]. With increasing  $R$ , the localized patches of subharmonic stripes begin to appear throughout the pattern ( $R \approx 4910$ ) superimposed on a mixed harmonic hexagon-stripe state [Fig. 46(b)]. Moving further into the coexistence parameter region, harmonic hexagons become less pronounced as domains of locally hexagonal, square and rhombic symmetries begin to form [Fig. 46(c)] [66]. Eventually ( $R \gtrsim 6280$ ), the harmonic component displays only domains of locally square symmetry and square superlattices begin to form [Fig. 46(d)].

Numerical simulations of the Oberbeck-Boussinesq equations demonstrate that the superlattice patterns can arise very near the bicritical point. With  $\delta Fr = \delta Fr_{2c}$ , square superlattices are found to bifurcate directly from the conduction state at  $R = R_{2c}$ . Both harmonic and subharmonic modes contain equal spectral power, which increases continuously from zero as  $\sqrt{R - R_{2c}}$ , *i.e.*, the square superlattices bifurcate supercritically from conduction. As  $R$  increases, the range of  $\delta Fr$  where square superlattices are attracting becomes wider [Fig. 47(b)]. These numerical solutions find parallel stripe patterns at both pure harmonic and pure subharmonic onset in the vicinity of the bicritical point. A second type of superlattice (stripe superlattices - Fig. 48) arises for increasing  $R$  near the bicritical point with  $\delta Fr < \delta Fr_{2c}$  [Fig. 47(b)]. The stripe superlattices also result from a supercritical bifurcation of subharmonics, this time from the base state of parallel harmonic stripes. Stripe superlattices are composed of a harmonic sublattice of parallel stripes and subharmonic stripes of two orientations. Stripe superlattices are found to be bistable with square superlattices over a relatively narrow parameter range [Fig. 47(b)].

Breaking of the Boussinesq symmetry in the experiments precludes the observation of square superlattices near the bicritical point in the laboratory. Physically, the significant variation of fluid properties due to large  $\Delta T \approx 17^\circ\text{C}$  near bicriticality is expected to lead to observable non-Boussinesq effects such as the appearance of hexagons near onset [Fig. 49(a)]. Experiments relatively close to bicriticality find domains of hexagons coexisting with domains of squares and rhombuses. Numerics that account for temperature dependent non-Boussinesq effects confirm experimental observations and indicate hexagons form throughout the harmonic component sufficiently near to bicriticality [Fig. 49(b)]. The hexagonal superlattices [Fig. 49(b)] are only observed numerically. In the experiments either the harmonic domain contains square and rhombic regions or the subharmonics remain localized on a regular harmonic hexagonal lattice. The difference seems due to experimental resolution and the hexagon superlattices, as well as the stripe superlattices, existing over relatively narrow parameter ranges.

Interestingly, hexagons in coexistence patterns may contain cold and warm centers simultaneously [Fig. 49(b)]. This unexpected hexagon characteristic is also experimentally observed near pure harmonic onset in the vicinity of the bicritical point. Since the understanding of hexagons in classical Rayleigh-Bénard predicts onset hexagons have a flow direction determined by the fluid properties through the sign of Busse's non-Boussinesq parameter [72] it is certainly surprising to find hexagons of both directions mixed together. This may be an effect of modulation, where the velocity fields slow down during a part of each drive cycle. The current experiments showing both up and down hexagons tend to be dominated by flows in one direction with the hexagons of the other orientation occurring at the domain boundaries or

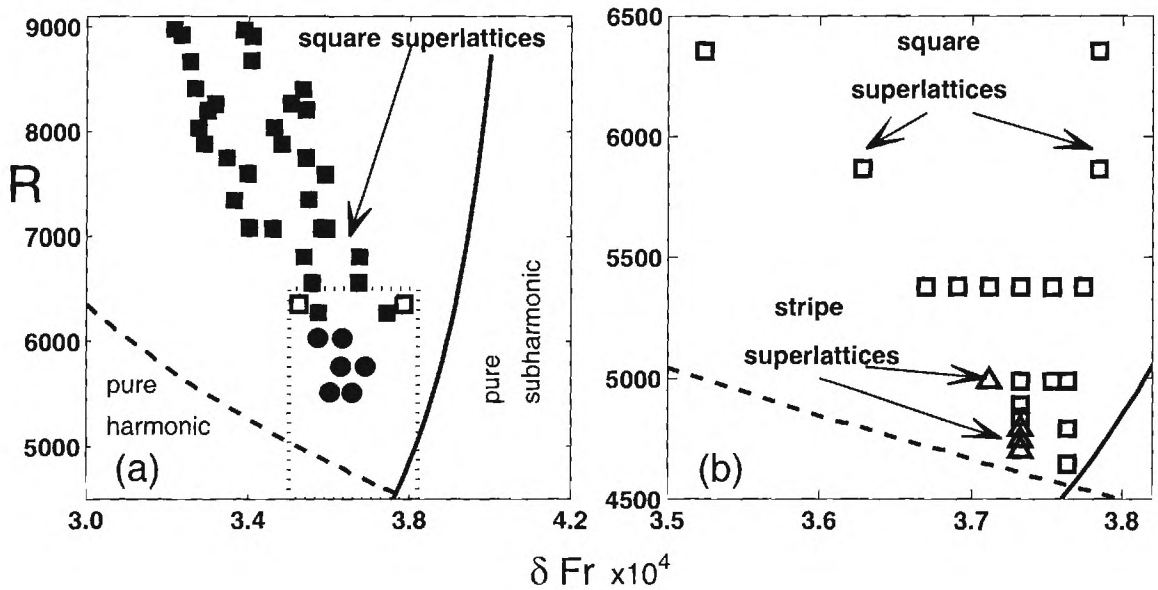


Figure 47: Phase planes mapped (a) experimentally and by (b) Boussinesq numerics. The dotted region in (a) is the parameter range shown in (b). Experimentally determined square superlattice (■) and mixed harmonic cellular symmetry patterns (●) boundaries are shown in (a). Locations of square superlattices (□) and stripe superlattices (△) in Boussinesq numerics are shown in (b). Square superlattice boundaries from non-Boussinesq experiments are compared (a) with boundaries found in Boussinesq numerics at  $R \approx 6300$ .

near the side walls.

### 5.4.2 Observations Away From Bicriticality

Violations of the Boussinesq symmetry have a decreasing influence on the coexistence planform as the experiment moves further into the coexistence regime. Increasing  $R$  while slowly decreasing  $\delta Fr$  to remain in patterns with relatively equal amounts of power in both harmonic and subharmonic modes ( $\varphi^H \approx \varphi^S$ ) experiments indicate the hexagonal domains decrease in size. For  $R \gtrsim 6280$  harmonic hexagonal domains

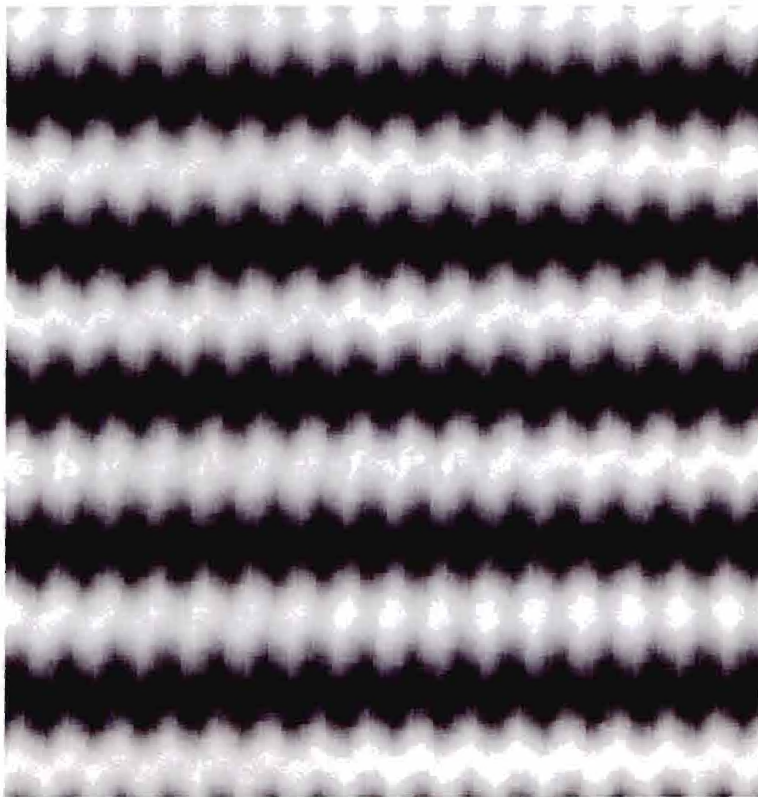


Figure 48: Numerical solutions find stripe superlattices ( $\delta Fr = 3.732 \times 10^{-4}$ ,  $\omega = 98$ , &  $R = 4794$ ) near the bicritical point.

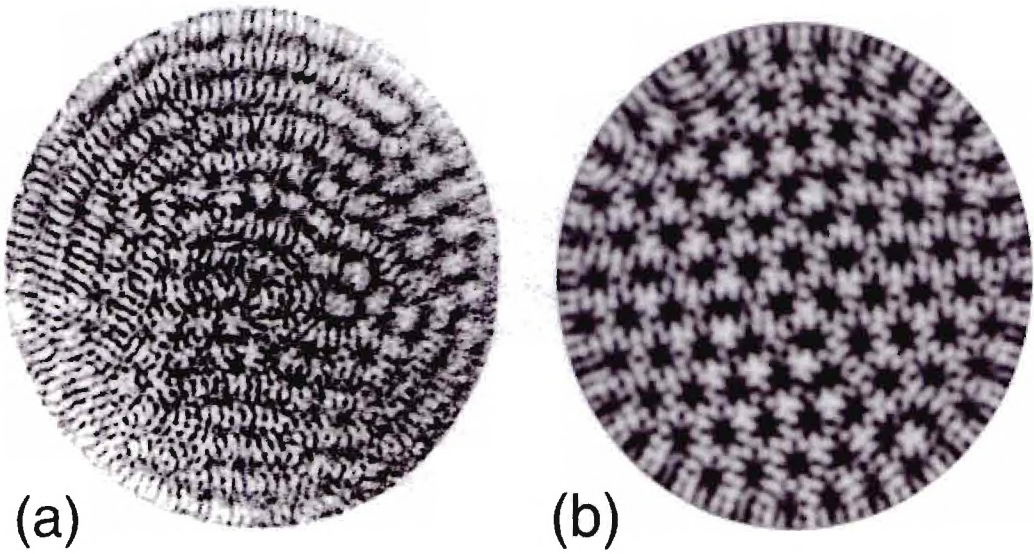


Figure 49: Coexistence patterns close to bicriticality display hexagons in the harmonic component due to non-Boussinesq effects in both (a) experiments ( $\delta Fr = 3.64 \times 10^{-4}$ ,  $\omega = 98.1$ , &  $R = 4983$ ) and (b) numerics ( $\delta Fr = 3.75 \times 10^{-4}$ ,  $\omega = 98$ , &  $R = 4750$ )

in the experiments are no longer present, as the harmonic component becomes dominated by locally square domains [Fig. 46(d)]. Continuing to increase  $R$  the domains of squares will form a single domain as regular square superlattices [Fig. 45(a)] appear. Square superlattices persist over the  $\delta Fr$  range [Fig. 47(a)] where  $\varphi^H \approx \varphi^S$  [Fig. 41(a)] for the entire experimentally accessible range in  $R$  ( $R \lesssim 9300$ ). Inversion symmetric numerical simulations find square superlattices are attracting over a widening range of  $\delta Fr$  moving away from bicriticality by increasing  $R$  [Fig. 47(b)]. For  $R \gtrsim 6280$  Boussinesq numerics agree with non-Boussinesq experiments for the parameter range of attracting square superlattices [Fig. 47(a)]. Experiments also indicate the relaxation time for a single domain to form is larger near the borders of the square superlattice parameter region.

Experiments varying  $\delta Fr$  (both increasing and decreasing) at fixed  $R$  are used to investigate the coexistence region. These experiments indicate the coexistence patterns may be divided into three distinct classes based on the magnitudes of  $\varphi^H$  and  $\varphi^S$ . The first class, already discussed in Sec. 5.2.1, is dominated by the harmonic component ( $\varphi^H \gtrsim 60\%$ ) and is found at smaller  $\delta Fr$  in the coexistence region. The second class of coexistence patterns, introduced in Sec. 5.2.2, is dominated by the subharmonic component ( $\varphi^S \gtrsim 60\%$ ) and occur at relatively large  $\delta Fr$ . For both classes of states dominated by a single temporal response patterns change slowly as  $\delta Fr$  is varied. Correspondingly, the spectral quantities of these patterns (Fig. 41) remain relatively constant. The third class of patterns have  $\varphi^H \approx \varphi^S$  and are found between the first two classes in parameter space near the middle in  $\delta Fr$  of the coexistence region. The third class of patterns are complex-ordered and the transitions between the first two classes and the third are abrupt. Increasing  $\delta Fr$  at

fixed  $R$  harmonic dominated patterns (first class) abruptly begin to show significant subharmonic contribution. Correspondingly, the harmonic planform separates into domains as  $q^H$  and  $\sigma^H$  become smaller. The emerging subharmonics display the largest  $q^S$  value for a given  $R$  within the coexistence region. With a small increase in  $\delta Fr$  square superlattices begin to form. Comparing to other coexistence patterns observed at a given  $R$  the square superlattices have the characteristics the  $q^H$  and  $\sigma^H$  reach minimal values and  $q^S$  is near its maximum value. The wave number characteristics can be described by  $q^S/q^H$  [Fig. 41(d)], which is significantly larger for square superlattices than for patterns dominated by the subharmonic component. Increasing  $\delta Fr$  at fixed  $R$  to pass out of the square superlattice region there is again an abrupt boundary after which the subharmonic component is dominant. The boundary between superlattices and class 2 coexistence patterns is characterized by an increase in  $\wp^S$ , increase in  $q^H$ , decrease in  $q^S$  and an increase in  $\sigma^H$  (Fig. 41). For the particular experiment shown in Fig. 41 the increase in  $\wp^S$  is somewhat masked by the emergence of transverse modulations with  $q \approx q^H$  (Sec. 5.2.2). Thereby,  $\wp^H$  has a contribution for subharmonic transverse modulations that increases the magnitude of  $\wp^H$ . For smaller  $R$ , where the transverse modulations do not arise (Fig. 32), the change in the magnitudes of  $\wp^H$  &  $\wp^S$  is more substantial (Fig. 60(e) - App. A). Hysteresis is not observed at any of the coexistence boundaries while varying  $\delta Fr$  at constant  $R$ .

Numerical solutions augment experimental information about the square superlattices. The imaging technique employed in these experiments (shadowgraphy) yields qualitative temperature field information. While techniques have been developed to gain quantitative temperature field information from a shadowgraph, the qualitative

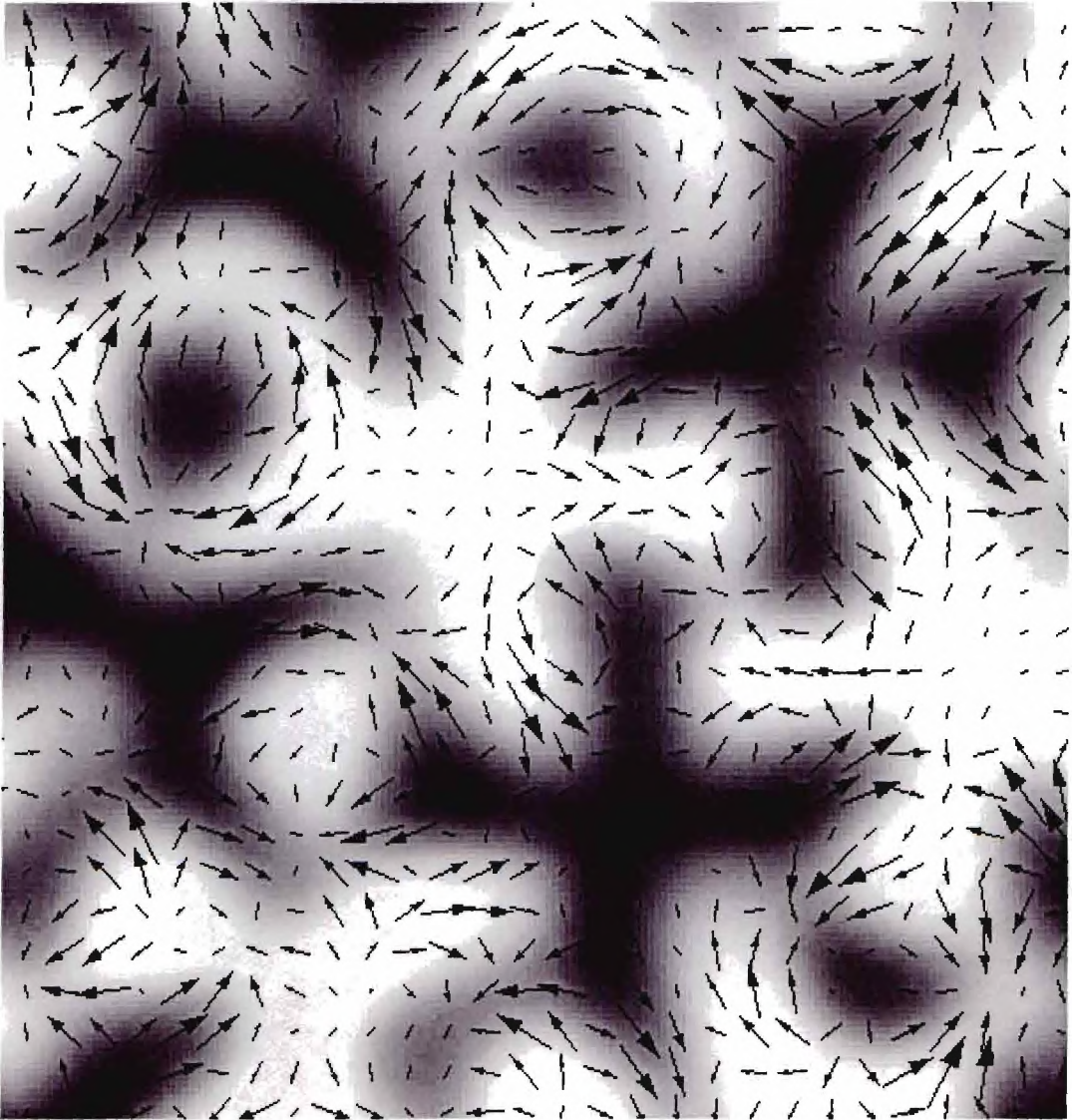


Figure 50: Temperature field (grayscale) and planar velocity field (arrows) in a square superlattice mid plane at  $\omega = 98$  observed in simulations.

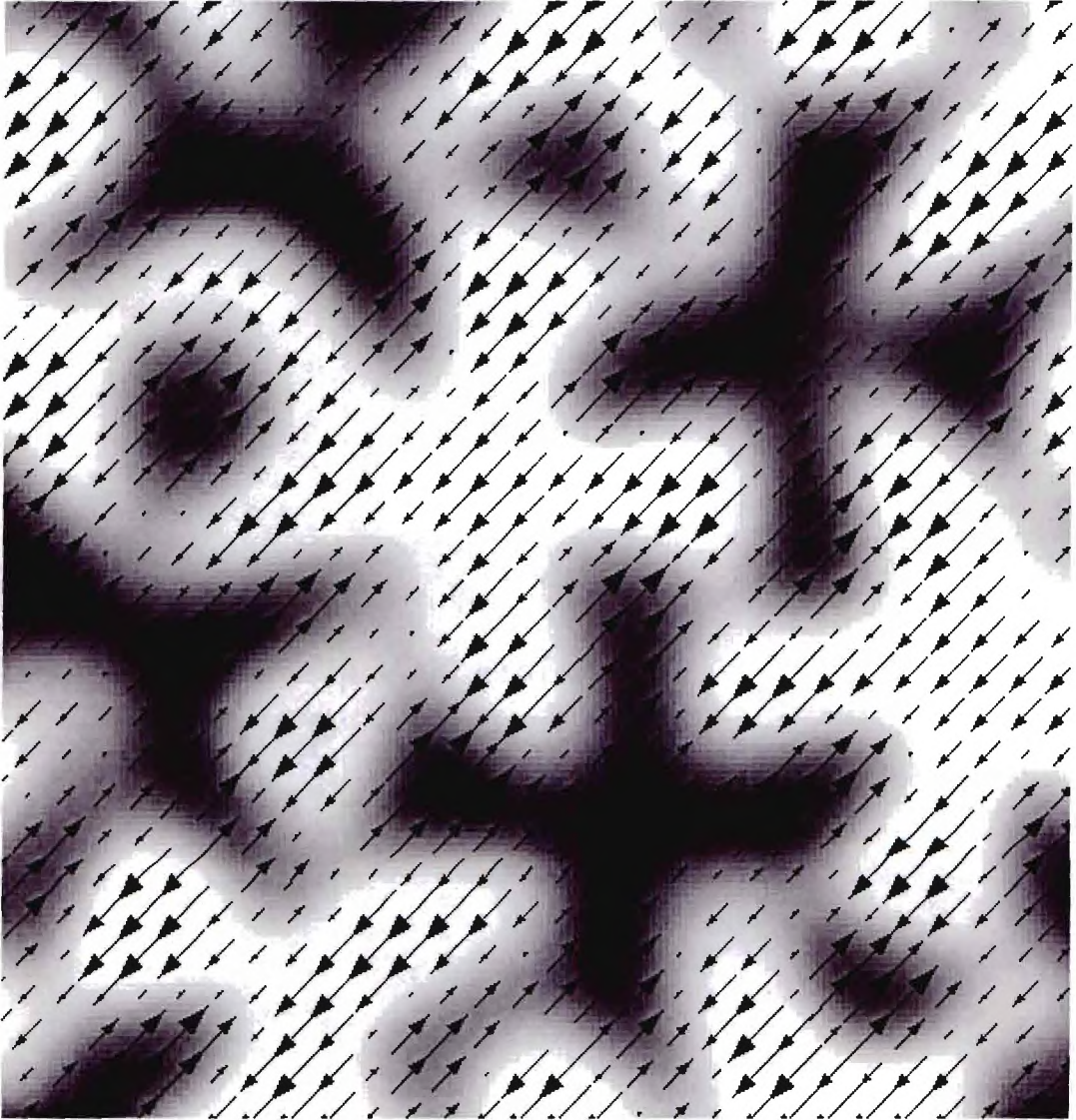


Figure 51: Temperature field (grayscale) and vertical velocity field (arrows) component corresponding to the planar field shown in Fig. 50.

description is sufficient for these purposes. However, experiments cannot yield any information about the velocity fields since no techniques for visualizing velocity fields in compressed gases currently exist. Since the agreement between experiments and simulations is so good, it seems reasonable to use simulations to gain information about the velocity fields in these square superlattices.

Simulations indicate the spatial temperature field complexities, not surprisingly, correspond to a complex velocity field. To demonstrate this, the temperature field at the mid-plane in height ( $z = 0$ ) is presented as a grayscale overlaid with the planar velocity field ( $v_x$  &  $v_y$ ) in Fig. 50 while the vertical component of the velocity field ( $v_z$ ) overlays the same temperature field in Fig. 51. In both figures the velocity field *and direction* is shown by arrows. Pattern segments approximately two harmonic wave lengths on a side taken from the bulk of the pattern (away from the side-walls) are shown in these figures. Warmer fluid is dark, while cooler fluid is white in Figs. 50 and 51. The square superlattice temperature and velocity fields on this scale support the notion that these are really a sort of dynamical superlattice.

### 5.4.3 Resonant Tetrads

Power spectra for the superlattice patterns demonstrate that the complex spatial structure of these states are described by a few spectral modes. Square superlattices (Fig. 45) have spectra with twelve dominant peaks at two distinct wave numbers ( $q^H$  &  $q^S$ ). The spatial backbone square sublattice corresponds to the four peaks  $\pm(\mathbf{q}_1^H, \mathbf{q}_2^H)$  [Fig. 52(a)], each separated by  $90^\circ$  at  $q = q^H$ . These peaks display a harmonic temporal response. The eight peaks at the larger  $q = q^S$ ,  $[\pm(\mathbf{q}_1^S, \mathbf{q}_2^S, \mathbf{q}_3^S, \mathbf{q}_4^S)]$  are due to the spatial stars in Fig. 45(a) and lie on a centered square in the spectral

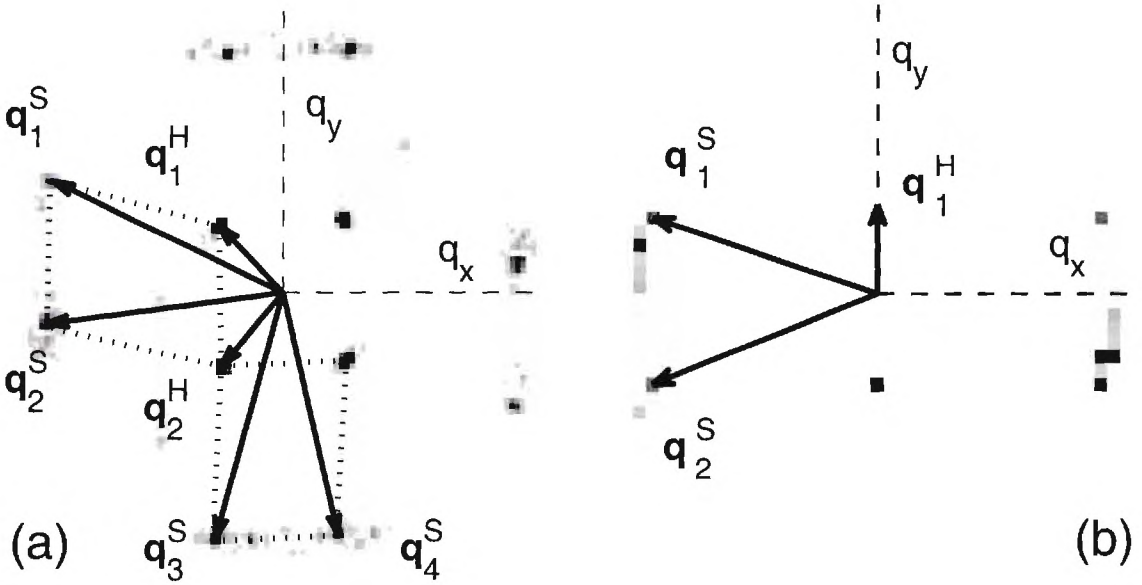


Figure 52: Power spectra for (a) the square superlattice in Fig. 45(a) (*experiment*) and (b) the stripe superlattice shown in Fig. 48 (*simulation*).

domain. These peaks display a subharmonic temporal response and form the subharmonic sublattice. Subharmonic peaks may translate dynamically a slight distance along the spectral square which they form under the constraint that the separation between a pair of peaks remains constant. In contrast, for the stripe superlattices the power spectra have only six dominant peaks [Fig. 52(b)]. The backbone spatial stripes correspond to the two peaks at  $\pm \mathbf{q}_1^H$  at the smaller  $q = q^H$ . The other four peaks [ $\pm(\mathbf{q}_1^S, \mathbf{q}_2^S)$ ] occur in pairs, display subharmonic temporal response and represent the subharmonic sublattice.

Interactions between the modes from the harmonic and subharmonic sublattices are found to always satisfy resonance conditions. Spectral changes made as the experiment passes into the square superlattice parameter regime are suggestive of interactions between the harmonic and subharmonic sublattices. In Sec. 5.4.2 it was shown

that power abruptly moves between the sublattices such that  $\wp^H \approx \wp^S$ , as well as  $q^S$  &  $q^H$  reaching maximal separation (Fig. 41) as square superlattices form. During the transition to square superlattices the power, which is typically distributed in bands about  $q^H$  and  $q^S$ , moves to a few discrete spectral peaks on the two sublattices. These peaks will form the vertices of parallelograms between two of the harmonic and two of the subharmonic peaks [Fig. 52(a)]. Existence of these parallelograms suggests the four wave resonance (*resonant tetrad*) conditions:

$$\begin{aligned} \pm(\mathbf{q}_1^H - \mathbf{q}_2^H) &= \pm(\mathbf{q}_1^S - \mathbf{q}_2^S) \quad \text{and} \\ \pm(\mathbf{q}_1^H + \mathbf{q}_2^H) &= \pm(\mathbf{q}_3^S - \mathbf{q}_4^S). \end{aligned} \quad (37)$$

Square superlattices in both experiments and numerics always satisfy these resonant tetrad [Eqs. (37)] conditions. In the vicinity of the bicritical point the parallelograms formed by the modes become rectangles. Further from onset, translations of the subharmonic peaks along the straight lines allows the  $|\mathbf{q}_i^S|$  ( $i = 1..4$ ) to take on different values for all  $i$ , while always satisfying Eqs. (37). Experiments indicate that with increasing  $R$  square superlattices are composed of relatively constant  $q^H$  ( $0.91q_{2c}^H \lesssim q^H \lesssim 0.94q_{2c}^H$ ) and that  $q^S$  decreases monotonically from  $0.92q_{2c}^S$  at  $R = 6280$  to  $0.77q_{2c}^S$  at  $R = 8920$ . A four wave resonance condition also applies for the stripe superlattices. For the stripe superlattices the condition is again between four modes and given by

$$\pm 2\mathbf{q}_1^H = \pm(\mathbf{q}_1^S - \mathbf{q}_2^S). \quad (38)$$

The resonance condition for stripe superlattices is a resonant tetrad between between modes of two different wave numbers and it contains a 'self-interaction' term for the harmonic mode ( $2\mathbf{q}_1^H$ ).

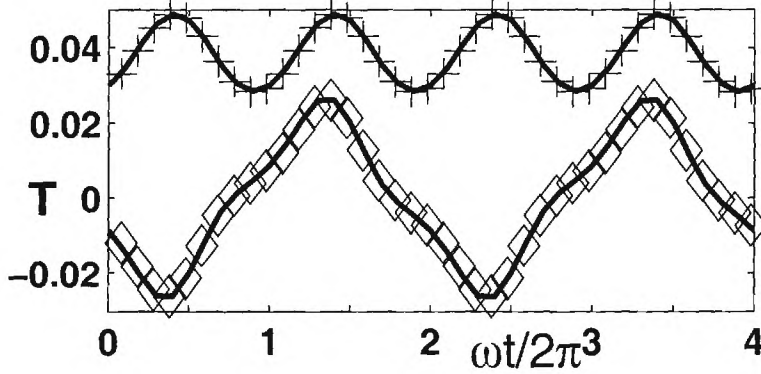


Figure 53: The temporal variation of linear eigenvectors multiplied with adjusted amplitude factors  $A = 0.0382$ ,  $B = 0.0108$  (see text) at  $\delta Fr = 3.732 \times 10^{-4}$ ,  $R = 4790$  for the harmonic (upper curve) and subharmonic (lower curve) modes, respectively. Comparison is made with the numerical amplitudes of the Fourier modes at  $\mathbf{q}_1^H$  (+) and  $\mathbf{q}_1^S$  ( $\diamond$ ), respectively, for the square superlattice mid plane temperature field  $T(\mathbf{x}, t)$  in units of  $\Delta T$ .

The noted prominence of the twelve modes satisfying resonant tetrad conditions [Eq. (37)] suggests the square superlattice patterns may be represented using the ansatz of an eigenmode expansion in the spirit of a weakly nonlinear analysis. The pattern field  $T(\mathbf{x}, t)$ , which is the shadowgraph intensity or mid plane temperature, may be defined as

$$T(\mathbf{x}, t) = \Re\{V^H(t) \sum_{j=1}^2 A_j^H \exp(i\mathbf{q}_j^H \cdot \mathbf{x})\} + \Re\{V^S(t) \sum_{j=1}^4 A_j^S \exp(i\mathbf{q}_j^S \cdot \mathbf{x})\}, \quad (39)$$

where  $\mathbf{x}$  is the horizontal coordinate parallel to the plane of the fluid layer. The time dependence of the harmonic and subharmonic eigenmodes  $\{V^H(t) \& V^S(t)\}$  is given by Floquet's theorem –  $V^{H,S} = \Re\{\exp(\mu^{H,S}t) \sum_{n=0}^{\infty} c_n^{H,S} \exp(in\omega t)\}$ , normalized such that  $|c_0^{H,S}| = 1$  – with Floquet exponents  $\mu^H = 0$  for harmonic modes and  $\mu^S = i\omega/2$  for subharmonic modes. Since the mode  $V^H$  is essentially sinusoidal about nonzero

mean (Fig. 53), only the first two terms ( $n = 0$  &  $n = 1$ ) need to be retained. In contrast,  $V^S$  requires several higher harmonics. To represent the snapshot of a regular square superlattice [Fig. 45(b)], where the spectral peaks form rectangles, only two constant real amplitudes  $A$  and  $B$  with  $A = A_1^H = -A_2^H$ ,  $B = A_1^S = A_2^S = A_3^S = A_4^S$  are needed in Eq. (39). The amplitudes of the dominant Fourier modes in Eq. (39), which are directly available from the numerical temperature field, exhibit time dependence that is very well represented by  $AV^H(t)$  and  $BV^S(t)$  with adjusted amplitudes  $A, B$  (Fig. 53). The stripe superlattice pattern (Fig. 48) can be described analogously by Eq. (39) with one harmonic amplitude  $A^H$  and two subharmonic amplitudes  $A_{1,2}^S$ , where  $A_1^S = A_2^S = iB$ .

Inversion symmetry (both Boussinesq and subharmonic time translation) plays an essential role in both the temporal dependence of the eigenmodes and the magnitudes of amplitudes in Eq. (39). The subharmonic eigenmodes ( $V^S$ ), regardless of the presence of Boussinesq symmetry, are subject to the temporal inversion symmetry of time translation. Higher harmonics of  $V^S$  must satisfy  $V^S(t+2\pi/\omega) = -V^S(t)$ . In the non-Boussinesq experiments and numerics quadratic couplings between the harmonic modes are allowed. Resonant triads in the harmonic component are responsible for the harmonic hexagons observed in the vicinity of the bicritical point and for delaying the onset of square superlattices. In the Boussinesq numerics inversion symmetry rules out quadratic couplings and requires those amplitudes to be zero. At cubic order the equation describing  $A_1^H$  has the common terms  $\sim A_1^H |A_j^H|^2$  ( $j = 1, 2$ ) and  $\sim A_1^H |A_j^S|^2$  ( $j = 1 \dots 4$ ) existing with different coupling constants. However, according to Eq. (37) additional resonant coupling terms  $\sim A_2^H A_1^S (A_2^S)^*$ ,  $(A_2^H)^* A_3^S (A_4^S)^*$  play a crucial role. It should be noted that two phases for the four subharmonic amplitudes remain

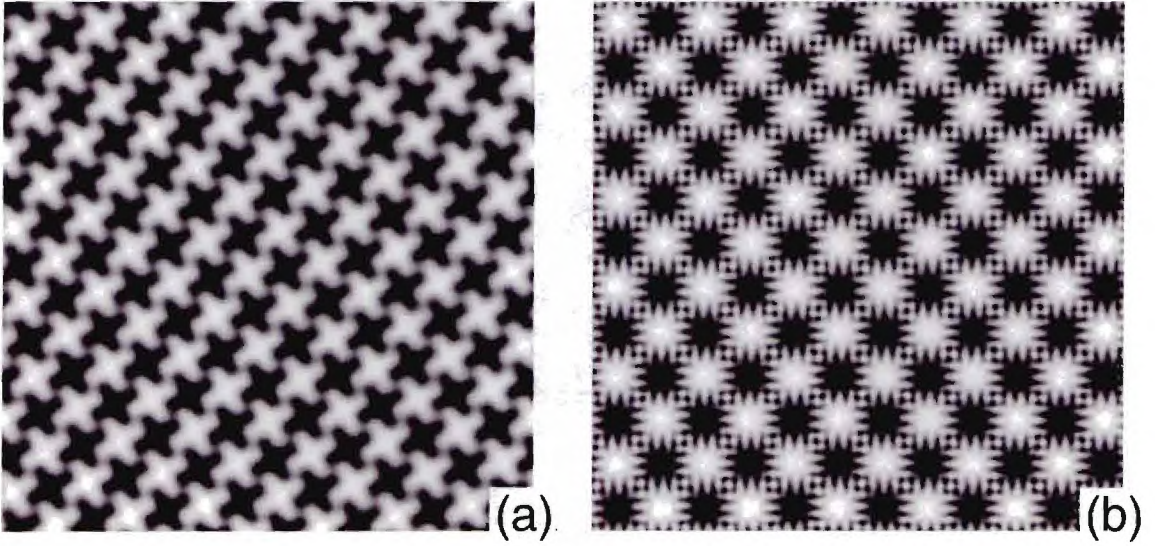


Figure 54: Superlattices (*numerical*) in the vicinity of the bicritical points at other  $\omega$  values: (a)  $\omega = 50$  and (b)  $\omega = 300$ .

arbitrary within the amplitude equations up to cubic order. To fix them, higher order resonances, which are automatically included in the full Oberbeck-Boussinesq equations [Eqs. (13)], come into play. The analogous coupled amplitude equations for the stripe superlattice pattern contain a resonant coupling  $\sim (A^H)^* A_1^S (A_2^S)^*$ .

#### 5.4.4 Other Frequencies

Interactions between modes at distinct wave numbers ( $q^H$  &  $q^S$ ) determine the spatial structure of the superlattices. As shown experimentally and numerically the superlattices in acceleration modulated Rayleigh-Bénard convection must satisfy resonant tetrad conditions (Sec. 5.4.3). These conditions exist between harmonic and sub-harmonic modes which are at distinct wave numbers,  $q^H$  and  $q^S$ , respectively. By

changing one of the characteristic wave numbers the modes will have to adjust locations to satisfy the appropriate resonance condition. As the modes move in Fourier space the structure of the corresponding sublattice and hence the composite superlattice will change. The wave number ratio  $q^S/q^H$  serves as a convenient description for the relative separation between harmonic and subharmonic modes. For square superlattices at  $\omega = 98.0$ ,  $q^S/q^H \lesssim 2.9$  [Fig. 41(d)].

Since  $q^H$  is relatively independent of  $\omega$  and  $q^S$  is strongly dependent on  $\omega$ , if superlattices exist at other  $\omega$  values (besides the considered  $\omega \approx 100$ ) they should display different structure than superlattices reported to this point. To look for superlattices at other  $\omega$ , simulations are performed at several  $\omega$  values and appropriately chosen  $\delta Fr = \delta Fr_{2c}$ ,  $R > R_{2c}$ . Superlattices are found at  $\omega = 50$  composed of a harmonic square sublattice and a subharmonic sublattice that is described by eight subharmonic peaks qualitatively similar to the square superlattice power spectrum at  $\omega = 98.0$ . In this case, the wave number ratio is  $q^S/q^H = 2.24$ . At  $\omega = 300$  numerics again find superlattices [Fig. 54(b)], this time with a much larger  $q^S/q^H = 5.42$ . Again, the harmonic sublattice displays regular square symmetry. At this larger  $\omega$  the subharmonic sublattice is composed of stripes which spatially are present along the harmonic square edges.

For verification of numerical predictions of changes to superlattice structure with  $\omega$ , preliminary experiments are performed at  $\omega = 50.4$ . Fig. 55(a) displays the *rhombic* superlattice found in experiments. The harmonic sublattice is rhombic and well-defined by four spectral peaks [Fig. 55(b)] at the smaller populated wave number ( $q^H$ ). For this superlattice the subharmonic sublattice is also defined by four spectral peaks with power spread along linear structures in a manner similar to the

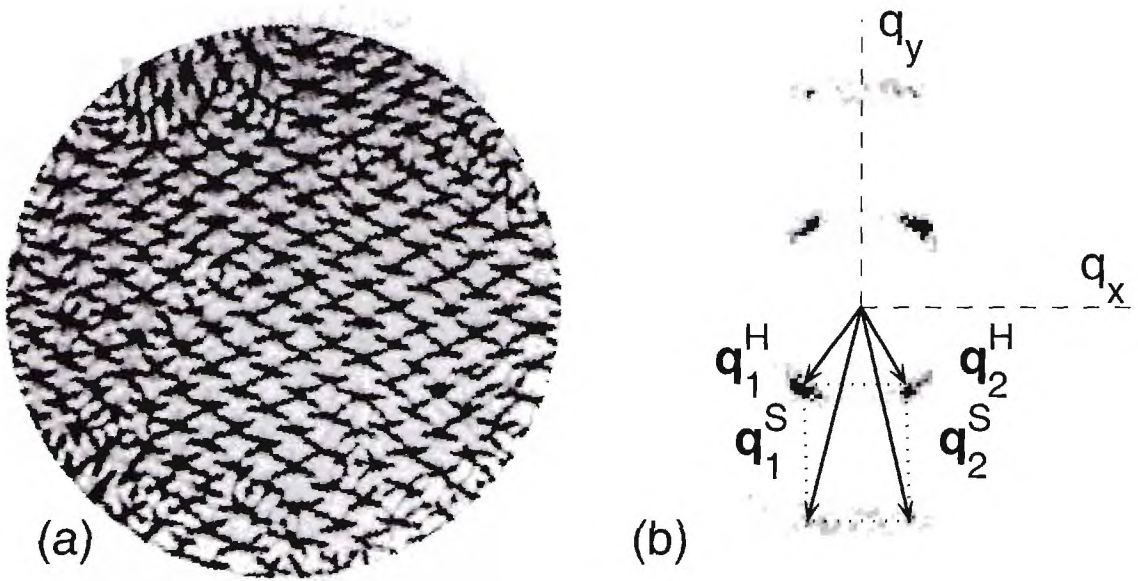


Figure 55: Superlattice (*experiment*) at  $\omega = 50$  (a) and its power spectrum (b).

experimental observations for square superlattices. However, the superlattices found in experiments at  $\omega = 50.4$  are not the ones predicted by numerics for  $\omega = 50$  [Fig. 54(a)]. The harmonic sublattice in simulations is square, while that in experiments is rhombic. More substantially, the numerical pattern is described by four pairs of Fourier peaks, while the experimental pattern has only two pairs of stimulated subharmonic modes. Both experimental and numerical superlattices satisfy the appropriate resonant tetrad conditions. Due to the relatively large displacement amplitude required to reach the vicinity of the bicritical point at  $\omega \approx 50$  ( $\delta Fr \approx 8.9 \times 10^{-4}$ ) these experiments require the enhanced range of the second experimental apparatus to be performed.

Initial experiments indicate the essential aspects of purely harmonic and purely subharmonic flows at  $\omega \approx 50$  are similar to those at  $\omega \lesssim 100$ . Shown in Fig. 56(a) is an example of spiral defect chaos in a purely harmonic flow at  $\omega = 50.4$ . It is quite

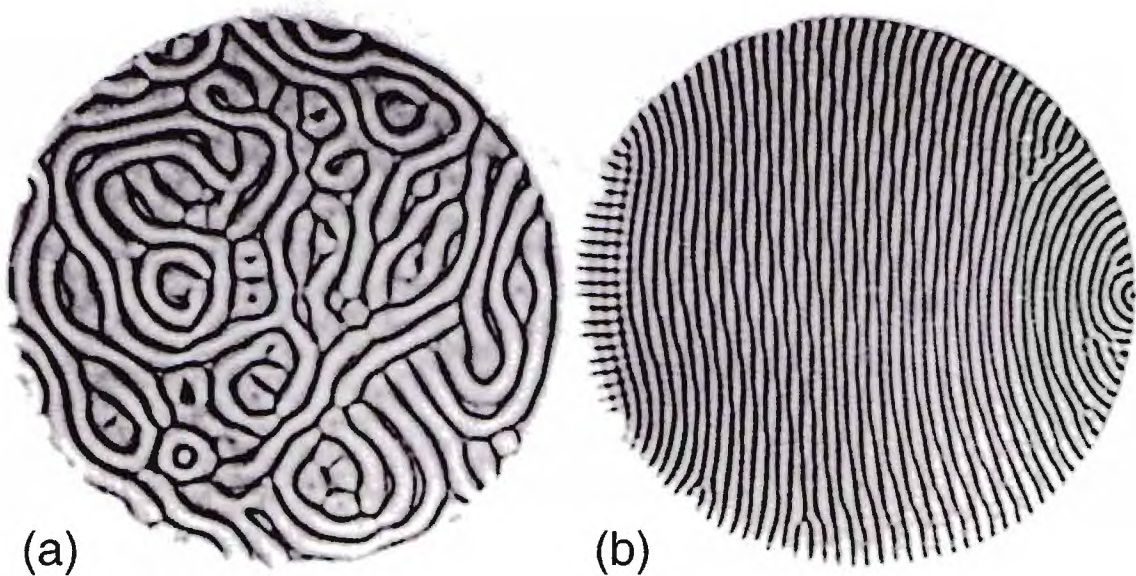


Figure 56: Patterns (*experiment*) at  $Pr = 0.928$ ,  $R = 5180$ ,  $\omega = 50.4$  of (a) purely harmonic spiral defect chaos ( $\delta Fr = 8.08 \times 10^{-4}$ ) and (b) purely subharmonic stripes with transverse modulation ( $\delta Fr = 9.27 \times 10^{-4}$ ).

similar in nature to the spiral defect chaos patterns found at  $\omega \approx 100$  [Figs. 33(c), 35(d) & 57(a)]. Similarly, the example of transversely modulated purely subharmonic stripes in Fig. 56(b) can be compared to those observed at  $\omega \approx 100$  [Fig. 36(c)].

## 5.5 Discussion

Moving away from onset into the harmonic parameter regime experiments were used to investigate stable patterns and transitions between these states. Pure harmonic patterns were found to closely resemble those known to exist in classical Rayleigh-Bénard convection. These states include the complex single  $q$  patterns typical of spiral defect chaos. As discussed, the harmonic pattern transition from an ordered state to spiral defect chaos as  $\delta Fr$  is decreased is remarkably similar to the transition

which occurs as  $R$  is increased in classical Rayleigh-Bénard convection. In both cases, the fluid is moving away from the conduction stability curve, so it seems reasonable that the transitions are similar. Thereby, acceleration modulated Rayleigh-Bénard convection allows this transition to be examined through two distinct tuning parameters ( $\delta Fr$  &  $R$ ). In cases when the side wall influence was relatively small, transitions from stripes and targets to spiral defect chaos were found to be qualitatively the same as those described in the initial report of spiral defect chaos [69]. For large  $R$  standard spiral defect chaos gives way to patterns with numerous disconnected islands without spirals, these too become more ordered with increasing  $\delta Fr$ .

Experimental observations made as the fluid moves away from subharmonic onset at relatively larger  $\delta Fr$  were discussed. Moving into purely subharmonic parameter regime the typical types of defects emerging on the base stripes were presented. Over a parameter range, subharmonic stripes were found to possess a transverse modulation propagating down the stripes. Spatial periodicity of these modulations was shown to be close to that displayed by harmonic patterns  $q^H$ . For sufficiently large  $\delta Fr$  and  $R$  subharmonic patterns were found to display no discernible spatial structure. Approximate phase-plane boundaries for onset of both transverse modulation and the loss of structure were presented.

Next, the transition from pure harmonic to pure subharmonic convection was considered for  $R > R_{2c}$ . This transition was found to be gradual as the experiment passed through a parameter region where harmonic and subharmonic patterns coexist, except near the midpoint in  $\delta Fr$  where values of  $\wp^H$  &  $\wp^S$  abruptly change as the contributions to the composite pattern from harmonic and subharmonic components quickly vary. Coexistence region parameter boundaries were experimentally

determined and found to track the marginal stability curves for conduction. The transition from pure harmonic flows to coexistence occurs as small, localized patches of subharmonic stripes emerge centered about harmonic defects. In contrast, the transition from pure subharmonic flow to coexistence (for  $R \lesssim 5500$ ) occurs as harmonic stripes gradually emerge throughout the convection cell. Several interesting two scale coexistence patterns were presented. Decomposing coexistence patterns showed that even in coexistence the harmonic and subharmonic components rotate in opposite directions.

Towards the coexistence region mid point in  $\delta Fr$ , experiments found complex-ordered patterns for the first time in a convection system. Planforms present in both harmonic and subharmonic components of the complex-ordered states are not found in pure harmonic or subharmonic patterns, indicating interactions between the stimulated wave numbers are the mechanism for superlattice formation. As superlattices form the power present in harmonic and subharmonic sublattices is nearly equal ( $\wp^H \approx \wp^S$ ), the values of  $q^H$  &  $q^S$  shift apart so  $q^S/q^H \approx 2.9$  and  $q^H$  &  $q^S$  become well-defined (minimal  $\sigma$ ).

Structure in the stimulated spectral modes of square superlattices suggested resonant tetrads between constituent sublattices were responsible for superlattice formation. This resonance mechanism is qualitatively different than resonant triads used to explain the recent observations of quasipatterns and superlattices in other pattern forming systems. All the observed superlattices were found to satisfy four wave conditions involving two harmonic and two subharmonic spectral modes. Resonant tetrads were found to be consistent with system symmetries of mid plane reflection (Boussinesq) and subharmonic time translation.

Numerical solutions of the Oberbeck-Boussinesq Equations [Eqs. (13)] were found to quantitatively reproduce experimental results except in the vicinity of the bicritical point, where non-Boussinesq effects are important. Both the structure and parameter range of square superlattices were found to quantitatively agree with experiments for  $R \gtrsim 6280$ . Numerics also found square superlattices persisted over a narrowing range in  $\delta Fr$  with decreasing  $R$  for  $R \lesssim 6280$ . In contrast, experiments found coexistence patterns whose harmonic sublattice was composed of domains of hexagons, rhombuses and squares [Fig. 60(a) – App. A].

This disagreement between experiments and numerics was addressed by slowly increasing  $R$  at  $\delta Fr \lesssim \delta Fr_{2c}$  in the laboratory. Regular harmonic hexagons observed near the bicritical point for  $\delta Fr < \delta Fr_{2c}$  indicated the Boussinesq symmetry is not valid for the experimental conditions used. While Boussinesq hexagons do exist, only harmonic stripes were observed over these parameters in simulations. Together these observations indicate the mid plane reflection symmetry is not present, allowing for resonant triads between harmonic modes. Time translation symmetry still excludes resonant triads among the subharmonic modes. Resonant triads correspond to second order terms, while resonant tetrads correspond to third order terms in an amplitude equation. The disagreement between experiments and numerics in the vicinity of bicriticality is due to the Boussinesq symmetry, which is present in the numerics and not in the experiments. This lack of reflection symmetry also explains the domains of hexagons that were observed coexisting with stripes or targets near harmonic onset. However, the observations of mixed up and down hexagons simultaneously present in pure harmonic and coexistence patterns in experiments and simulations is potentially a fruitful line of investigation. It is worth noting that mixed hexagonal states have not

been reported in thermally modulated Rayleigh-Bénard, although Meyers, Cannell, & Ahlers [39] did discuss the effects of reversing velocity fields on hexagons in thermally modulated convection in terms of the effects of fluctuations when the velocity is suppressed. It is also possible that the mixed up and down hexagons are due to the imaging technique itself. Numerical investigations of this point are currently underway. However, the simulations are time consuming, the system is very close to onset, and to this point there is no conclusive evidence either way from the numerics.

Numerical solutions augment experimental findings by allowing the investigation of  $R \lesssim 6280$  in the presence of Boussinesq symmetry. These simulations indicate square superlattices persist over a narrowing  $\delta Fr$  range with decreasing  $R_{2c}$  all the way down to  $R_{2c} \approx 0$ . At the bicritical point square superlattices were found to emerge from conduction due to a supercritical bifurcation. Numerics found an additional superlattice with different spectral structure over a narrow parameter range near the bicritical point. This stripe superlattice was not observed in experiments, although it is predicted to exist in the presence of Boussinesq symmetry over a parameter range where this symmetry is violated in the experiments. Numerics indicate stripe superlattices bifurcate supercritically from a harmonic parallel stripe base state. The appropriate resonant tetrad condition for stripe superlattices included a self-interaction term.

The dependence of  $q^H$  and  $q^S$  on modulation parameters ( $\omega$ , in particular) indicates the modulation parameters may be used to tune the superlattice structure by changing  $q^S/q^H$ . Preliminary experimental and numerical results for  $\omega \approx 50$  and numerical results for  $\omega = 300$  confirmed these expectations. Superlattices found at these  $\omega$  values were presented. Disagreements between numerics and experiments

about superlattice structure at  $\omega \approx 50$  are not disappointing, rather seem minor and indicate a rich diversity of complex-ordered patterns are present. Below  $\omega \approx 36$  simulations indicate superlattices are no longer attractors.

Numerous expected and unexpected results have been found in this first experimental investigation of acceleration modulated Rayleigh-Bénard convection. With the improved dynamical range of the second experimental apparatus a much wider range of parameters are now accessible. Additionally, the unexpected rotations present in the first experimental device are reduced by at least an order of magnitude when using the second device. Patterns and transitions in purely subharmonic flows present several interesting questions: what is the nature of the transverse modulations, what is the nature of and temporal components of flows when the spatial structure breaks down and do other temporal resonances become accessible? Additionally, how do these patterns change with  $\omega$ ? Is there something like a dispersion relation in Faraday wave experiments for  $q^S$  for  $Pr \approx 1$ ? Investigating the various types of superlattices at different  $\omega$  seems fruitful and remains to be well explored. Particularly, for  $\omega \lesssim 36$  numerics indicate superlattices are not found. Is there some type of transition as  $\omega$  passes through  $\omega \approx 36$  that allows superlattices to form? Do experiments confirm numerical results for superlattices bifurcating supercritically from conduction in the presence of Boussinesq symmetry? While not covered here, many interesting dynamics might be expected for this system with heating from above ( $T_1 > T_2$ ), where again bicritical points have been predicted. This case is treated numerically in the dissertation of Oliver Brausch [28]. Prior to the experiments finding coexistence and superlattices, numerical investigations never knew to look for complex-ordered states. It seems quite reasonable that these experiments may encourage a reexamination of

acceleration modulated Rayleigh-Bénard convection as a vehicle for investigating the effects of modulation on hydrodynamics and that future investigations will make unexpected discoveries.

# APPENDIX A

## First Reprint

Appendix A is a reprint of the first published Letter describing initial experimental results for acceleration modulated Rayleigh-Bénard convection. The experimental apparatus without an air-bearing was used in attaining all of these results. Notably, pattern rotations are reported which were later (see 5.3) found to be sensitive to the magnitude of the lateral vibrations present in shaking. This Letter appeared in *Physical Review Letters*, volume **84** on pages 87-90 in 2000.

### **Rayleigh-Bénard Convection in a Vertically Oscillated Fluid Layer**

Jeffrey L. Rogers and Michael F. Schatz

*School of Physics, Georgia Institute of Technology, Atlanta, Georgia 30332-0430*

Jonathan L. Bougie and Jack B. Swift

*Department of Physics and Center for Nonlinear Dynamics, University of Texas, Austin,  
Texas 78712*

We report on the first quantitative observations of convection in a fluid layer driven by both heating from below and vertical sinusoidal oscillation. Just above onset, convection patterns are modulated either harmonically or subharmonically to the drive frequency. Single-frequency patterns exhibit nearly solid-body rotations

with harmonic and subharmonic states always rotating in opposite directions. Flows with both harmonic and subharmonic responses are found near a codimension two point, yielding novel coexisting patterns with symmetries not found in either single-frequency states. Predictions from linear stability analysis of the onset Rayleigh and wave numbers compare well with experiment and phase boundaries for coexisting patterns track single-frequency marginal stability curves.

PACS numbers: 47.54.+r, 47.20.-k, 47.20.Lz, 47.20.Bp

Characterizing pattern formation is a fundamental problem in the study of nonequilibrium systems. Wavenumber selection mechanisms provide one useful means for identifying common pattern forming behaviors in diverse physical systems [73]. The pattern wavenumber  $q$  may be selected by geometrical constraints; a canonical example of *geometry-induced* patterns is found in Rayleigh-Bénard convection where the pattern length scale is governed by the fluid layer thickness  $d$  [7]. By contrast, the selected  $q$  may depend on an externally imposed frequency  $\omega$  in systems subjected to spatially uniform, time-periodic oscillation [73]; a common example of these *dispersion-induced* patterns is the parametric excitation of surface waves (Faraday waves) in an open container of fluid [7]. Pattern selection by these generic mechanisms also arises in nonhydrodynamic systems; geometry-induced patterns occur in the buckling instability of thin plates [74], while dispersion-induced patterns are generated by optical waves in a fiber laser [75] and crystallization waves in  $^4\text{He}$  [76].

We report the first experimental observations of both geometry-induced (onset  $q$  weakly dependent on  $\omega$ ) and dispersion-induced (onset  $q$  strongly dependent on  $\omega$ ) patterns in a single system: a fluid layer that is both heated from below and vertically

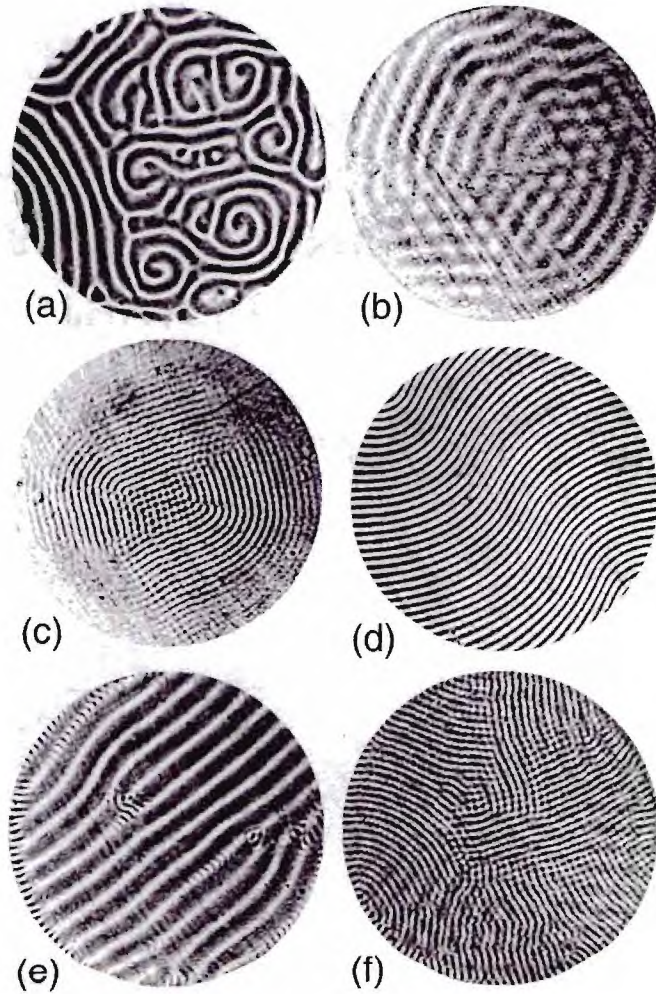


Figure 57: Convection patterns visualized using shadowgraphy and characterized by four dimensionless quantities: Prandtl number  $Pr = \frac{\nu}{\kappa} = 0.93$ , driving frequency  $\omega = \frac{d^2}{\kappa} 2\pi f = 98$ , displacement amplitude  $\delta = \frac{\kappa^2}{gd^4} \delta'$  and Rayleigh number  $R = \frac{\alpha g d^3 \Delta T}{\nu \kappa}$ , with the kinematic viscosity  $\nu$ , thermal diffusivity  $\kappa$ , thermal expansion coefficient  $\alpha$ , forcing frequency  $f$  (Hz), amplitude  $\delta'$  (cm) and gravitational acceleration  $g = 980$  ( $\frac{cm}{s^2}$ ). (a) H spiral defect chaos ( $\delta = 1.76 \times 10^{-4}$ ,  $R = 3198$ ). (b) coexisting H rolls and hexagons ( $\delta = 3.74 \times 10^{-4}$ ,  $R = 4216$ ). (c) S rolls near onset ( $\delta = 4.26 \times 10^{-4}$ ,  $R = 3958$ ). (d) S rolls ( $\delta = 4.05 \times 10^{-4}$ ,  $R = 4990$ ). (e) H rolls with localized domains of S rolls ( $\delta = 3.76 \times 10^{-4}$ ,  $R = 4962$ ). (f) S rolls containing grain boundaries overlaying a weak pattern of H rolls and cells ( $\delta = 3.64 \times 10^{-4}$ ,  $R = 5424$ ).

oscillated sinusoidally. Fluid motion in this system requires a thermally-induced density variation, as characterized by the Rayleigh number  $R$  (Fig. 57). When the drive amplitude  $\delta$  or oscillation frequency  $\omega$  are small, we observe fluid motion modulated at  $\omega$  [harmonic (H)] and geometry-induced spatial structure [Fig. 57(a)] reminiscent of standard Rayleigh-Bénard convection [69]. For sufficiently large  $\delta$  or  $\omega$ , flows arise with modulation at  $\omega/2$  [subharmonic (S)], characteristic of dispersion-induced Faraday wave patterns. Our measurements for the onset of these patterns quantitatively test both stability calculations and numerical simulations performed over the past thirty years [35, 77, 50, 38, 52, 53, 78]. Patterns exhibit nearly solid-body rotation over a wide parameter range with H and S patterns always rotating in opposite directions. In addition, we find and characterize a region of parameter space where the distinct spatial and temporal scales of H and S patterns interweave to form complex states [Figs. 57(e) and 57(f)], including localized domains of one pattern embedded in the other, mode-locking, and formation of pattern symmetries not found in either pure state.

Experiments are performed on a layer of  $\text{CO}_2$  gas bounded below by a 0.6 cm-thick gold-coated aluminum mirror, laterally by a  $(3.80 \pm 0.03)$  cm inner diameter ring of filter paper and above by a 2.54 cm-thick sapphire window. Two cell depths are studied:  $d = (6.50 \text{ and } 6.72 \pm 0.03) \times 10^{-2}$  cm, corresponding to a vertical diffusion time of  $\tau_v \equiv d^2/\kappa \approx 2$  s. Length is scaled by  $d$  and time by  $\tau_v$ . Thermal gradients are imposed across the fluid layer by heating the mirror from below and using circulating water to cool the window from above resulting in a vertical temperature difference ( $\Delta T$ ) controlled to within  $\pm 0.01^\circ$  C. The fluid layer is vertically vibrated sinusoidally by a hydraulic piston under closed-loop control rendering oscillations with less than 4% of

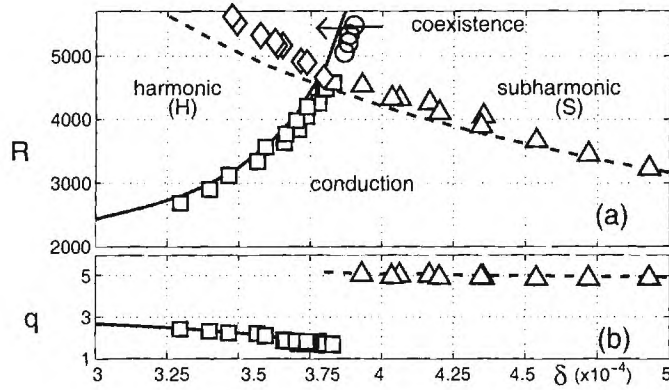


Figure 58: Phase diagram and comparison of linear stability predictions to experiments at  $\omega = 98$ . The phase diagram (a) contains regions of conduction, convection with H ( $\omega$ ) and S ( $\omega/2$ ) modulations as well as coexisting H-S patterns. Marginal stability curves computed for the conduction state subjected to H (solid line) and S (dashed) perturbations agree with the measured values of  $R_c$  (a) and  $q_c$  (b) at the onset of H ( $\square$ ) and S ( $\triangle$ ) convection. The measured transition to coexisting patterns from pure H ( $\diamond$ ) and S ( $\circ$ ) states is compared to the marginal stability predictions for *conduction*. The maximum displacement ( $\delta = 5 \times 10^{-4}$ ) corresponds to an acceleration of  $\sim 5g$ .

the total amplitude in higher harmonics. Patterns are visualized using shadowgraphy and recorded by a digital image acquisition system. To determine H or S amplitude modulation pattern images are captured at  $\sim 20$  Hz (twice the drive frequency) while long-time dynamics are recorded at  $\sim 0.5$  Hz using a shutter synchronized with the piston motion. For  $\delta = 0$  (no oscillations), the conductive state loses stability to roll patterns, suggesting that non-Boussinesq effects are weak and occur below the limit of our temperature resolution. These observations are consistent with our calculations using a variational model described by previous authors[72, 79, 62], which demonstrate rolls are the globally stable state for  $R$  only  $\sim 0.3\%$  larger than the unmodulated critical value,  $R_c^0 = 1708$ . Patterns are explored with  $\omega$  and  $Pr$  held constant (Fig. 57) while increasing and decreasing  $\delta$  at various fixed values of  $R$ .

H convection occurs for small  $\delta$  [Fig. 58(a)]. Without oscillations ( $\delta = 0$ ) spiral defect chaos arises for  $R \gtrsim 2500$  in agreement with previous experiments [69]. With oscillations ( $\delta > 0$  at fixed  $R$ ), spiral defect chaos modulated at  $\omega$  persists for a significant range in  $\delta$  (e.g.,  $\delta \lesssim 3.30 \times 10^{-4}$  at  $R = 4840$ ). With increasing  $\delta$  the number of spiral defects decrease as more regular states whose morphology depends on  $R$  emerge. For  $2500 \lesssim R \lesssim 3900$  these emerging patterns are typically multi-arm spirals which reduce in arm number, eventually becoming targets as the conduction state is approached. At larger  $R$  ( $3900 \lesssim R \lesssim 5500$ ) spiral defect chaos becomes a pattern of nearly parallel rolls tending to terminate perpendicular to the sidewalls and possessing several foci at the boundaries; the number of foci and curvature of the associated rolls decreases with increasing  $\delta$ . The transition with increasing  $\delta$  from spiral defect chaos to parallel rolls is reminiscent of the well-studied transition in unmodulated Rayleigh-Bénard convection for decreasing  $R$  [65]. For  $3100 \lesssim R < 4560$  uniform parallel rolls or targets lose stability with increasing  $\delta$  as domains of hexagons form [Fig. 1(b)]. These states of hexagons and rolls or targets occur only for a narrow range ( $\approx 6 \times 10^{-6}$ ) of  $\delta$  before losing stability to conduction with a small additional increase in  $\delta$ . Within the experimental resolution in  $\delta$  ( $\approx 2 \times 10^{-6}$ ) no hysteresis is observed in the transition between the hexagon-roll states and conduction. The nonhysteretic transition and morphology of these patterns are consistent with other modulated Rayleigh-Bénard experiments involving time-periodic driving of the bottom plate temperature [39].

S convection is observed for sufficiently large  $\delta$  [Fig. 58(a)]. The onset of S patterns occurs as a *uniform patch* of rolls; no hysteresis or hexagons are observed, consistent with the S temporal symmetry that excludes three wave interactions [7].

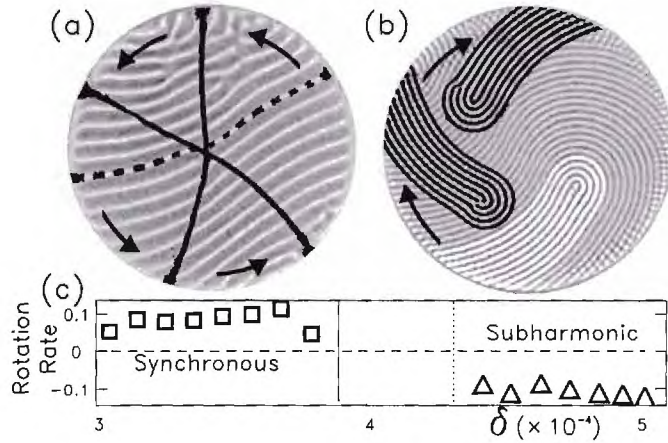


Figure 59: H ( $\square$ ) and S ( $\triangle$ ) patterns rotate in opposite directions. (a) At  $\delta = 3.47 \times 10^{-4}$  the motion of a single H roll (dashed line) is followed in time at intervals of  $11.3 \tau_v$ . (b) At  $\delta = 4.53 \times 10^{-4}$  the motion of a S disclination (bright white region) is followed in time at intervals of  $15.0 \tau_v$ . (c) The dimensionless rotation rate versus  $\delta$  for  $R = 3920$  and  $\omega = 98$ .

With increasing  $\delta$  other roll domains form with grain boundaries at the domain intersections. The roll domains merge with further increase in  $\delta$ , leading to the formation of disclinations that may interact [Fig. 57(c)]. For sufficiently large  $\delta$ , either a single convex disclination or, less frequently, a spiral arises centered within the convection cell. These patterns experience skew-varicose instabilities leading to repeated nucleation of dislocations, additionally the patterns may move off-center [Fig. 59(b)]. With increasing  $\delta$  a single roll domain forms with few dislocations and a long wavelength distortion [Fig. 57(d)]. Patterns qualitatively similar to Figure 57(d) have been previously observed in rotating Rayleigh-Bénard convection [80].

Following the method described by previous investigators [52, 53] we performed a linear stability analysis of the conductive state. The resulting predictions for both critical Rayleigh numbers  $R_c$  and critical wave numbers  $q_c$  are in good agreement with the experimentally observed values at onset of both H and S convection (Fig.

58). For H convection, modulation enhances the stability of conduction ( $R_c > R_c^0$ ) while decreasing  $q_c$  below its unmodulated value  $q_c^0=3.117$ ; consistent with previous modulated Rayleigh-Bénard experiments [39]. In addition, for S convection  $R_c > R_c^0$  and  $q_c$  decrease with increasing  $\delta$  (Fig. 58). For parameter values not studied here  $R_c$  is predicted to drop below  $R_c^0$  [52].

For  $R \gtrsim 2500$  patterns undergo nearly solid-body rotation where H and S states rotate opposite directions (Fig. 59). For fixed  $R$  ( $2500 \lesssim R \lesssim 4560$ ) and increasing  $\delta$  from zero, the onset of rotation occurs near  $\delta \approx 2 \times 10^{-4}$ . Patterns deviate somewhat from ideal solid-body rotation because point defects and grain boundaries continually propagate within the rotating patterns. Global rotation rate increases with  $\delta$  except near the conduction boundaries where rotation slows as patterns weaken [Fig. 59(c)]. A given rotation direction is selected and maintained by the patterns throughout the duration of an experimental trial. Patterns do not equally select clockwise and counter-clockwise directions; in 62 separate experiments H states rotated counter-clockwise in 84% of the trials. In all cases, H and S patterns rotate in opposite directions. Rotations are qualitatively robust against perturbations from tilting the apparatus  $\sim 5^\circ$  off the vertical, changing the sidewalls to square symmetry and asymmetric cooling of the top plate.

For  $R > 4560$  conduction is no longer stable; instead H and S patterns compete and coexist over a range of  $\delta$  between the pure states [Fig. 58(a)]. As  $\delta$  is increased, pure H states lose stability to mixed patterns where localized patches of S rolls form about H defects and are advected along as the defects propagate. At slightly larger  $\delta$  [*e.g.*,  $\delta = 3.67 \times 10^{-4}$  in Fig. 60(e)], S rolls begin to form perpendicular to H upflows throughout the pattern [Fig. 57(e)]. The wavenumber of emerging S rolls ( $q_S$ ) is

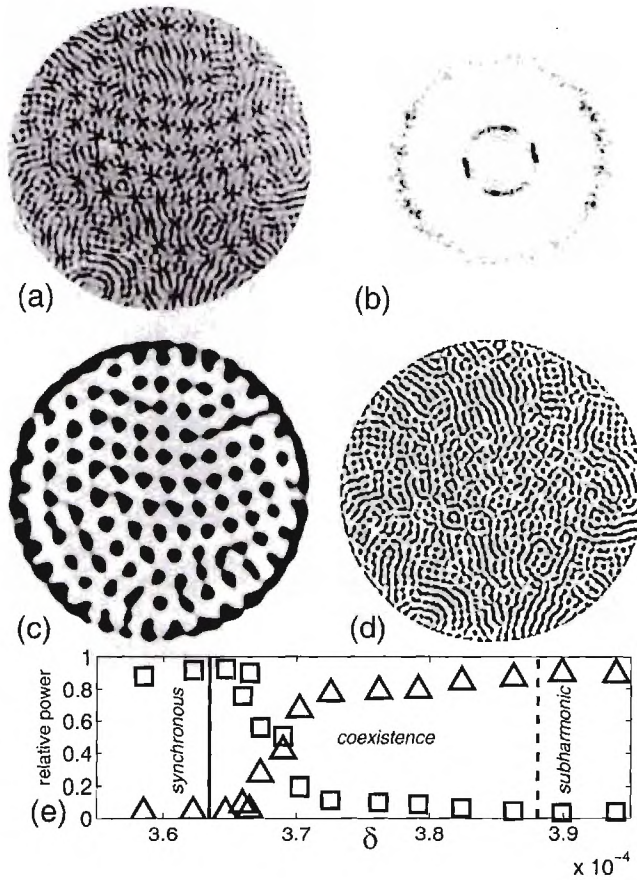


Figure 60: Coexisting H and S patterns (a) ( $\delta = 3.62 \times 10^{-4}$ ,  $\omega = 108$  and  $R = 5515$ ) may be decomposed by filtering in the wavenumber domain (b) to yield both H (c) and S (d) components; in this case, both components equal power to the wavenumber spectrum (b) and exhibit mode-locking of the wave numbers ( $\frac{q_S}{q_H} = \frac{5.02}{1.67} = 3.01$ ). (e) The relative power contributed by H ( $\square$ ) and S ( $\triangle$ ) components to wavenumber spectra changes abruptly as a function of  $\delta$  for constant  $\omega = 98$  and  $R = 5320$ . Vertical lines mark the measured coexistence boundaries.

close to the second harmonic of the H pattern wavenumber ( $q_H$ ). A small change in  $\delta$  [e.g.,  $\delta = 3.69 \times 10^{-4}$  in Fig. 60(e)] yields states where H patterns of local hexagonal, square and rhombic symmetries are mixed with rolls of the S component perpendicular to the cell faces [Fig. 60(a), 60(c) and 60(d)]. For these states, the H and S components contribute equal power to the wavenumber spectra and have mode-locked wave numbers ( $\frac{q_S}{q_H} = 3$ ). With further small increases in  $\delta$  [ $\delta \gtrsim 3.72 \times 10^{-4}$  in Fig. 60(e)], the S component dominates the power spectra and, concurrently, the wavenumber ratio unlocks ( $\frac{q_S}{q_H} < 2.8$ ) as  $q_H$  increases abruptly. The S component forms domains of increasingly larger size as the H component gradually weakens [Fig. 57(f)]. Upon crossing the phase boundary with purely S states [Fig. 58(a)] rolls with a long-wavelength distortion are typically observed [Fig. 57(d)].

The experimentally determined phase boundaries separating coexisting states from the pure patterns track the marginal stability curves for the *conduction* state [Fig. 58(a)]. For  $R > 4560$ , the H marginal stability curve is in nearly exact agreement with the phase boundary between coexisting and pure S states. This suggests the S base state from which H convection bifurcates differs little from conduction in a spatially averaged sense. Spatial Fourier spectra support this viewpoint since the higher modes of S patterns cannot overlap with the smaller wavenumber H fundamental. By contrast, the experimentally determined phase boundary between coexisting and pure H states lies above the S marginal stability curve, suggesting that H convection inhibits the onset of S convection due to wavenumber interaction. Evidence for this inhibitory effect is further bolstered by the observation that S convection first appears near H pattern defects. The amplitude of convective flow is generally suppressed in the cores of pattern defects [71] and, therefore, any inhibitory effect

of H convection on S patterns should be weaker near defects. Moreover, a previous stability analysis of the H base state suggests the onset of S convection is delayed by the presence of H convection [52].

These multiple length scale convection patterns differ qualitatively from coexisting wavelength states in spatially separate domains observed in optical systems [26] as well as quasiperiodic [81] and superlattice [82, 22, 21] states reported in Faraday experiments. Three wave interactions (resonant triads) are responsible for multi-scale Faraday patterns; it seems doubtful resonant triads are important in the convection patterns described here due to the S temporal symmetry and large difference between  $q_H$  and  $q_S$ . Resonant triads may be introduced in convection patterns by non-Boussinesq effects and for the current experiment with heating from above squares and quasiperiodic structures have been predicted [78].

This work is supported by the NASA Office of Life and Microgravity Sciences Grant NAG3-2006 (at the Georgia Institute of Technology) and NAG3-1839 (at the University of Texas-Austin).

# APPENDIX B

## Second Reprint

App. B is a reprint of the second published Letter describing superlattices initially observed in accelerated-modulated Rayleigh-Bénard experiments and then confirmed in numerical solution of the Boussinesq equations. This Letter appeared in *Physical Review Letters*, volume **85** on pages 4281-4284 in 2000.

### **Superlattice patterns in vertically oscillated Rayleigh-Bénard convection**

Jeffrey L. Rogers and Michael F. Schatz

*Center for Nonlinear Science and School of Physics, Georgia Institute of Technology,*

*Atlanta, Georgia 30332-0430*

Oliver Brausch and Werner Pesch

*Physikalisches Institut der Universität Bayreuth, Bayreuth, Germany 95440*

We report the first observations of superlattices in thermal convection. The superlattices are selected by a four-mode resonance mechanism that is qualitatively different from the three-mode resonance responsible for complex-ordered patterns observed previously in other nonequilibrium systems. Numerical simulations quantitatively describe both the pattern structure and the stability boundaries of superlattices

observed in laboratory experiments. In the presence of the inversion symmetry, superlattices are found numerically to bifurcate supercritically directly from conduction or from a striped base state.

PACS numbers: 47.20.-k, 47.54.+r, 47.20.Ky

Symmetry plays a crucial role in selecting the patterns displayed in physical, chemical and biological systems as they are driven away from equilibrium [7]. Frequently, an initially homogeneous state loses stability with increasing driving to a regular pattern containing a narrow band of wavenumbers. System symmetries select the allowable nonlinear mode interactions which dictate the pattern structure. In isotropic systems that are inversion symmetric (invariant under a change in sign of the field variables), periodic parallel stripes (rolls) or squares typically form at onset while hexagons form in the absence of inversion symmetry due to three-mode interactions (*resonant triads*). Under some conditions, *complex-ordered* [17] patterns displaying exotic spatial structure described by relatively few Fourier modes emerge at onset as the result of interactions between multiple disparate wavenumbers. These exotic states include *superlattices*, which are spatially periodic, and *quasipatterns*, which have a definite rotational symmetry but are spatially aperiodic [20, 81, 21, 23, 22, 82, 83, 26]. In all these cases, the lack of inversion symmetry allows resonant triads to determine the pattern structure [17, 20, 81, 21, 23, 22, 82, 83, 26, 84].

We report the first experimental and numerical evidence of superlattices in Rayleigh-Bénard convection (RBC). Unlike previously observed complex-ordered patterns these superlattices may occur in the presence of inversion symmetry, which inhibits resonant triads. Instead, we find qualitatively different four-mode interactions (*resonant*

*tetrads*) are responsible for selecting the patterns' planforms. One type of superlattice, which we call a square superlattice (SQS) [Fig. 61(a)], is found to bifurcate supercritically from conduction at a codimension-two (*bicritical*) point where linear modes of two disparate wavenumbers simultaneously become marginally stable. Studies of RBC have helped reveal many basic principles in pattern formation since the experiments are precise and can often be directly compared with the theoretical description available through the Oberbeck-Boussinesq equations (OBE) [85]. Our results show that understanding of complex-ordered patterns in nonequilibrium systems may be advanced by experimental/theoretical investigations of RBC.

Convection patterns with multiple distinct length and time scales are found in a thin fluid layer subjected both to a vertical thermal gradient and vertical sinusoidal oscillations. Numerical predictions [35, 53] recently confirmed by experiments [66] indicate such flows arise for sufficiently large Rayleigh number  $R = \frac{\alpha g d^3 \Delta T}{\nu \kappa}$ , with thermal expansivity  $\alpha$ , gravitational acceleration  $g$ , fluid layer depth  $d$ , imposed temperature difference  $\Delta T$ , kinematic viscosity  $\nu$  and thermal diffusivity  $\kappa$ . The critical Rayleigh number  $R_c$  depends on three additional parameters: Prandtl number  $Pr = \frac{\nu}{\kappa}$ , oscillation frequency  $\omega = d^2 \omega' / \kappa$  and displacement amplitude  $\delta = \frac{\kappa^2}{g d^4} \delta'$  ( $\omega'$  and  $\delta'$  are the dimensional frequency and amplitude, respectively). For fixed  $Pr$  and  $\omega$ , modulated flows with a long-lengthscale and harmonic (H) temporal response ( $\omega$ ) arise for small  $\delta$ . Short-lengthscale flows displaying subharmonic (S) temporal response ( $\omega/2$ ) are found when  $\delta$  is sufficiently large. At a bicritical point  $(\delta_{2c}, R_{2c})$ , H and S modes arise simultaneously with distinct critical wavenumbers  $q_{2c}^H$  and  $q_{2c}^S$ .

We study convection in thin layers of compressed CO<sub>2</sub>. The configuration of our experimental setup was described previously [66]. Results detailed in this Letter are

obtained for  $Pr = 0.930$  and  $\omega = 98.0$  by quasistatically varying  $\delta$  and  $R$  for a layer at a mean temperature of  $34.00 \pm 0.01$  °C and pressure of  $32.700 \pm 0.001$  bar. The layer depth is  $d = 0.0650$  cm, yielding a characteristic vertical diffusion time  $\frac{d^2}{\kappa} \approx 2$  sec. For these conditions, the bicritical point occurs at  $\delta_{2c} = 3.768 \times 10^{-4}$ ,  $R_{2c} = 4554$  with wavenumbers  $q_{2c}^H = 1.742$  and  $q_{2c}^S = 5.173$  (scaled by  $d^{-1}$ ). We also solve the OBE using a code tested for standard RBC [85, 56], generalized to include time dependent acceleration [61]. Due to the applied pseudo-spectral method the spatial variations in the plane are naturally captured by 2D-Fourier modes. The simulations are typically performed on a  $256 \times 256$  grid with periodic boundary conditions and a time step  $dt = 0.04(2\pi/\omega)$ . We have further validated our numerical methods by reproducing known values of  $R_c$  and the associated critical wavenumbers for both H and S onset, as well as typically observed experimental patterns. For presentation purposes we define a reduced Rayleigh number  $\epsilon_2 = R/R_{2c} - 1$ .

SQS display short-lengthscale, star-like structures located on a long-lengthscale square lattice [Fig. 61(a)]. The backbone square sublattice, which usually displays few defects in both experiments and simulations, is spanned by the H modes  $\pm \mathbf{q}_1^H$  and  $\pm \mathbf{q}_2^H$  with  $|\mathbf{q}_i^H| \approx q_{2c}^H$  [Fig. 61(b)]. The star-like structures, which may have various orientations, are captured by the eight spectral peaks  $\pm(\mathbf{q}_1^S, \mathbf{q}_2^S)$  and  $\pm(\mathbf{q}_3^S, \mathbf{q}_4^S)$ , where  $|\mathbf{q}_i^S| \approx q_{2c}^S$ ; the peaks occur in pairs along lines parallel to sums and differences of  $\pm \mathbf{q}_1^H$  and  $\pm \mathbf{q}_2^H$ . The end points of the wave vectors  $\mathbf{q}_1^H, \mathbf{q}_2^H; \mathbf{q}_1^S, \mathbf{q}_2^S$  and  $-\mathbf{q}_1^H, \mathbf{q}_2^H; \mathbf{q}_3^S, \mathbf{q}_4^S$  span parallelograms separated by an angle of approximately  $90^\circ$  [dotted lines in Fig. 61(b)].

Experiments find SQS states are attracting for a wide range of parameters except in the vicinity of the bicritical point (Fig. 62). The range of stable SQS is found by

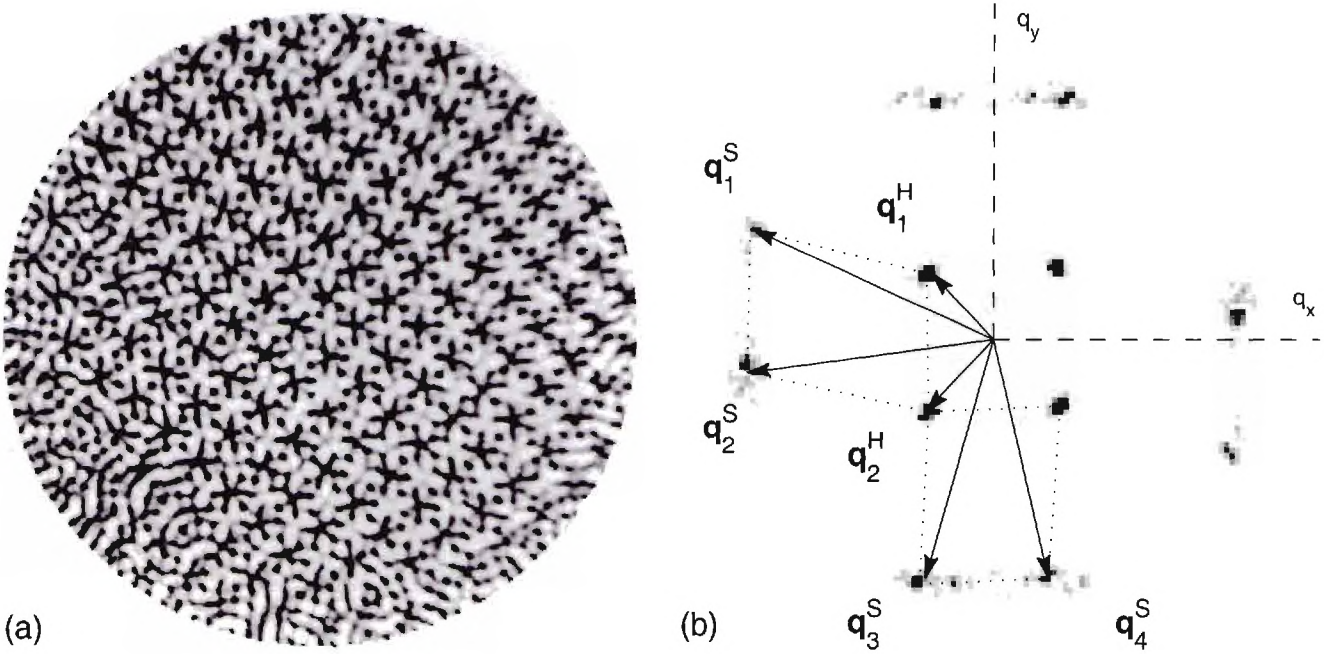


Figure 61: Experimental square superlattice (SQS) at  $\delta = 3.58 \times 10^{-4}$  and  $\epsilon_2 = 0.650$ . These states display complex periodic spatial structure (a) and power spectra (b) typically dominated by twelve peaks with  $|\mathbf{q}_i^H| \approx 0.95q_{2c}^H$  and  $|\mathbf{q}_i^S| \approx 0.86q_{2c}^S$  for these parameter values.

slowly increasing or decreasing a single parameter ( $\delta$  or  $\epsilon_2$ ). No hysteresis is observed in determining the SQS parameter boundary and the SQS patterns form independent of the initial state. SQS are observed for a range of  $\delta$  from  $\epsilon_2 \gtrsim 0.38$  up to the largest  $\epsilon_2$  experimentally accessible ( $\approx 1$ ). Over the SQS region  $|\mathbf{q}_i^H|$  remains relatively constant with values from  $0.91q_{2c}^H$  to  $0.94q_{2c}^H$  while  $|\mathbf{q}_i^S|$  decreases monotonically with increasing  $\epsilon_2$  from  $0.92q_{2c}^S$  at  $\epsilon_2 \approx 0.38$  to  $0.78q_{2c}^S$  at  $\epsilon_2 \approx 0.96$ . For  $0.2 \lesssim \epsilon_2 \lesssim 0.38$  over a narrow range of  $\delta$ , the uniform square H sublattice found in SQS is supplanted by a disordered sublattice containing domains of locally square, rhombic and hexagonal symmetries (see Fig. 4 in [66]). For  $\epsilon_2 < 0.38$ , the H sublattice is comprised increasingly of hexagons with decreasing  $\epsilon_2$ . For  $\epsilon_2 \gtrsim 0.2$ , the S component displays star-like structures while close to bicriticality ( $\delta \approx \delta_{2c}$  and  $\epsilon_2 \lesssim 0.2$ ) the S component is simply patches of rolls superimposed on a nearly uniform H hexagonal sublattice. For  $\delta$  slightly less than  $\delta_{2c}$  experiments find uniform, pure H hexagons at onset. We attribute the appearance of hexagons to non-Boussinesq effects which break the fluid layer inversion symmetry about the midplane (Boussinesq symmetry) and allow for three-mode interactions between the H modes [72].

Our numerical simulations confirm many of the experimental findings and, additionally, allow investigation of the behavior near bicriticality in the presence of inversion symmetry. For  $\epsilon_2 \approx 0.4$ , numerical SQS stability boundaries, which are computed using random initial conditions, are in good agreement with experiment (Fig. 62). In accord with experiments SQS always form by locking into resonant states with  $|\mathbf{q}_i^H| \approx q_{2c}^H$  and  $|\mathbf{q}_i^S| \approx q_{2c}^S$ . With decreasing  $\epsilon_2$  the SQS are found over a smoothly narrowing range of  $\delta$  about  $\delta_{2c}$  (Fig. 62 inset). The disordered H sublattices observed in experiments for  $0.2 \lesssim \epsilon_2 \lesssim 0.38$  are typically seen only as transients

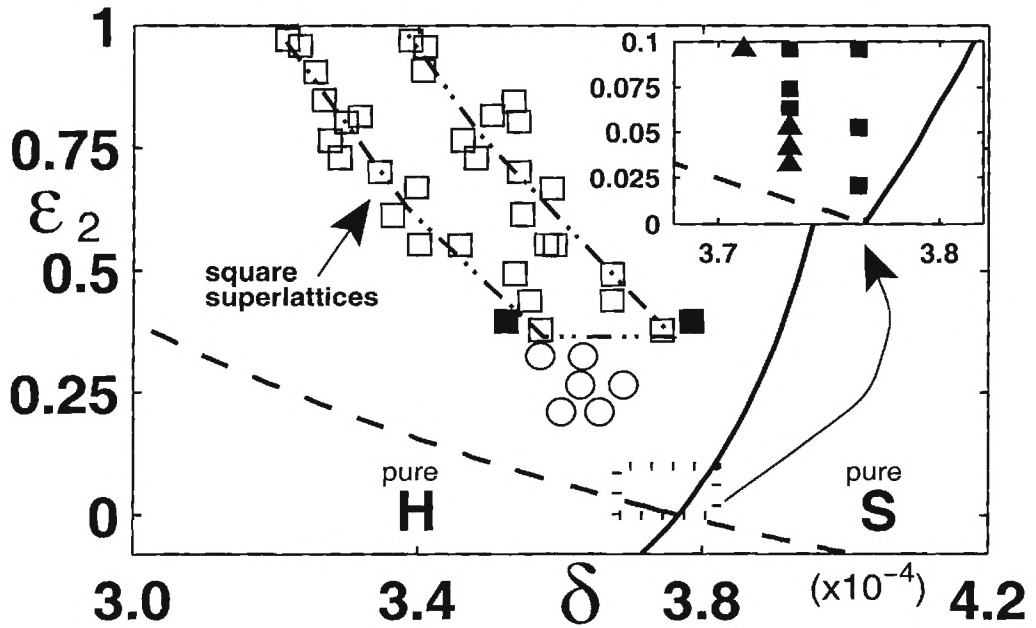


Figure 62: Phase-plane showing the SQS stability boundaries as well as the codimension-two point at the intersection of the H (solid) and S (dashed) linear stability curves. Experimentally observed SQS boundary ( $\square$ ) is reproduced in numerical solutions ( $\blacksquare$ ) at  $\epsilon_2 \approx 0.4$ . Experimental patterns in the  $\circ$  bounded region display square, rhombic and hexagonal symmetry in the H sublattice. Numerical results indicate SQS are the result of a supercritical primary bifurcation at the bicritical point ( $\blacksquare$  inset). Simulations also find roll superlattices ( $\blacktriangle$  inset), over a narrow parameter range, which bifurcate supercritically from H rolls.

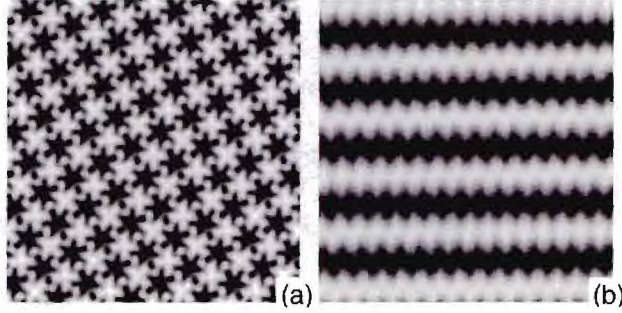


Figure 63: Superlattices observed in numerics near the bicritical point: (a) SQS at  $\delta = \delta_{2c}$  and  $\epsilon_2 = 0.053$ , (b) roll superlattice at  $\delta = 3.732 \times 10^{-4}$  and  $\epsilon_2 = 0.053$

in the simulations. Moving closer to the bicritical point the SQS patterns become more regular, i.e., the parallelograms in Figure 61(b) become regular rectangles as  $|\mathbf{q}_i^H| \rightarrow q_{2c}^H$  and  $|\mathbf{q}_i^S| \rightarrow q_{2c}^S$ . In this regime, obtaining SQS from random initial conditions becomes prohibitively difficult due to critical slowing down; thus, we used approximate SQS states with  $\leq 10\%$  amplitude noise as initial conditions and found stable SQS patterns for  $\epsilon_2$  as small as 0.005. (For  $\epsilon_2 < 0.005$  our grid in Fourier space has insufficient resolution to describe accurately the SQS mode structure.) At  $\delta_{2c}$  we find the H and S mode amplitudes vary like  $\sqrt{\epsilon_2}$  indicating the SQS bifurcate supercritically from conduction directly at the bicritical point.

Near the bicritical point, simulations find another superlattice state for  $\delta \lesssim \delta_{2c}$ . In this case, the conduction state becomes unstable to pure H rolls at onset. With increasing  $\epsilon_2$  a secondary instability leads to a state that we call *roll superlattices* [Fig. 63(b)]. They are (at least linearly) stable over a narrow parameter range before the transition to SQS at larger  $\epsilon_2$ . For instance at  $\delta = 3.732 \times 10^{-4}$  roll superlattices are observed for  $0.033 \leq \epsilon_2 \leq 0.079$  (Fig. 62 inset). There exists partial bistability with SQS; for example, SQS can arise for  $\epsilon_2 \geq 0.063$  at  $\delta = 3.732 \times 10^{-4}$ . Above the

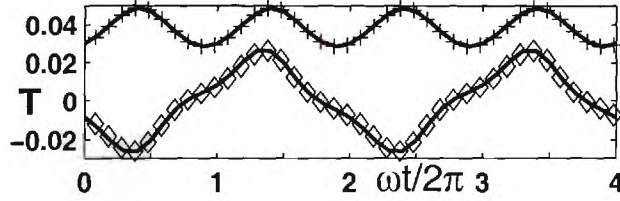


Figure 64: The temporal variation of linear eigenvectors multiplied with adjusted amplitude factors  $A = 0.0382$ ,  $B = 0.0108$  (see text) at  $\delta = 3.732 \times 10^{-4}$ ,  $\epsilon_2 = 0.053$  for the H (upper curve) and S (lower curve) modes, respectively. Comparison is made with the numerical amplitudes of the Fourier modes at  $\mathbf{q}_1^H$  (+) and  $\mathbf{q}_1^S$  ( $\diamond$ ), respectively, for the SQS midplane temperature field  $T(\mathbf{x}, t)$  in units of  $\Delta T$ .

onset of roll superlattices the S mode amplitudes follow the common square-root law characteristic for a supercritical bifurcation.

The wave-vector structure of experimental and numerical superlattices indicate four-mode interactions are critical to superlattice formation. The parallelograms in  $q$ -space [Fig. 61(b)] suggest the H and S modes in SQS patterns satisfy the resonance conditions

$$\pm(\mathbf{q}_1^H - \mathbf{q}_2^H) = \pm(\mathbf{q}_1^S - \mathbf{q}_2^S); \pm(\mathbf{q}_1^H + \mathbf{q}_2^H) = \pm(\mathbf{q}_3^S - \mathbf{q}_4^S). \quad (40)$$

Wavevectors for each mode class (H or S) need not be of equal magnitude to satisfy these relations; thus, Eq (40) describes cases found in both experiments [Fig. 61] and simulations where  $|\mathbf{q}_i^S|$  may be different for each  $i$  when  $\epsilon_2$  is sufficiently large. A four-mode resonance also governs the roll superlattices. In this case, only three distinct spectral peaks are involved; these peaks form a parallelogram by the self-interaction of the H mode. The resonance condition takes the form  $2\mathbf{q}_1^H = \mathbf{q}_1'^S - \mathbf{q}_2'^S$ .

The noted prominence of the twelve modes in line with Eq. (40) suggests the SQS pattern may be represented using the ansatz of a eigenmode expansion in the spirit of a weakly nonlinear analysis. The pattern field  $T(\mathbf{x}, t)$ , which is the shadowgraph

intensity or midplane temperature, may be defined as

$$T(\mathbf{x}, t) = \Re\{V^H(t) \sum_{j=1}^2 A_j^H \exp(i\mathbf{q}_j^H \cdot \mathbf{x})\} + \Re\{V^S(t) \sum_{j=1}^4 A_j^S \exp(i\mathbf{q}_j^S \cdot \mathbf{x})\}, \quad (41)$$

where  $\mathbf{x}$  is the horizontal coordinate parallel to the plane of the fluid layer. The time dependence of the H and S eigenmodes,  $V^H(t)$  and  $V^S(t)$ , is given by Floquet's theorem:  $V^{H,S} = \Re\{\exp(\mu^{H,S}t) \sum_{n=0}^{\infty} c_n^{H,S} \exp(in\omega t)\}$  (normalized to  $|c_0^{H,S}| = 1$ ) with Floquet exponents  $\mu^H = 0$  for H modes and  $\mu^S = i\omega/2$  for S modes. The mode  $V^H$  is well-described by retaining only the  $n = 0$  and  $n = 1$  terms; i.e.,  $V^H$  is essentially sinusoidal with a constant offset (Fig. 64). By contrast,  $V^S$  contains several harmonics of  $\omega/2$  satisfying the S time-translation symmetry  $V^S(t + 2\pi/\omega) = -V^S(t)$ . To represent the snapshot of a regular SQS [Fig. 63(a)], where the spectral peaks form rectangles, only two constant real amplitudes  $A$  and  $B$  with  $A = A_1^H = -A_2^H$ ,  $B = A_1^S = A_2^S = A_3^S = A_4^S$  are needed in Eq. (41). The amplitudes of the dominant Fourier modes in Eq. (41), which are directly available from the numerical temperature field, exhibit time dependence that is very well represented by  $AV^H(t)$  and  $BV^S(t)$  with adjusted amplitudes  $A, B$  (Fig. 64). The roll superlattice pattern [Fig. 63(b)] can be described analogously to Eq. (41) with one H amplitude  $A^H$  and two S amplitudes  $A_{1,2}^S$ , where  $A_1^S = A_2^S = iB$ .

The general structure of the cubic nonlinearities in the six coupled amplitude equations for SQS, which determine the six amplitudes  $A$  in Eq. (41), is suggested by four-wave resonance according to Eq. (40). Inversion symmetry rules out quadratic couplings. For the equation describing  $A_1^H$  at the cubic order, the common terms

$\sim A_1^H |A_j^H|^2$  ( $j = 1, 2$ ) and  $\sim A_1^H |A_j^S|^2$  ( $j = 1 \dots 4$ ) exist with different coupling constants. However, according to Eq. (40) additional resonant coupling terms  $\sim A_2^H A_1^S (A_2^S)^*$ ,  $(A_2^H)^* A_3^S (A_4^S)^*$  play a crucial role. It should be noted that two phases for the four S amplitudes remain arbitrary within the amplitude equations up to cubic order. To fix them, higher order resonances, which are automatically included in the full OBE, come into play. The analogous coupled amplitude equations for the roll superlattice pattern contain a resonant coupling  $\sim (A^H)^* A_1^S (A_2^S)^*$ .

Superlattices in modulated thermal convection differ from superficially similar patterns observed in Faraday surface-wave [21, 23, 22, 82] and optical [17, 83, 26] systems. First, although general theoretical insight into complex-ordered nonlinear patterns in the Faraday system has progressed impressively [86], we are not aware of quantitatively accurate comparisons with experiments. (The situation is similar in the optical case.) By contrast, superlattices observed in modulated RBC experiments can be quantitatively compared with solutions of the OBE. Second, while the temporal symmetry of invariance under discrete time translation by  $2\pi/\omega$  rules out resonant triads among S modes in all parametrically modulated systems, resonant triads in Faraday waves are allowed by the interaction of S and H modes. In modulated Boussinesq RBC the additional symmetry of midplane inversion acts on both H and S modes; thus, all quadratic interactions are suppressed, and resonant tetrads are responsible for the formation of superlattices. Lastly, superlattices in the Faraday and optical systems must satisfy both frequency and wavenumber resonance conditions while those in modulated RBC need only satisfy a wavenumber condition. This can be understood by recalling that both Faraday waves (in the limit of small viscosity and infinite depth) and modulated RBC can be modeled by the Mathieu equation, which

describes a vertically oscillated pendulum. Onset of surface waves in the Faraday case is analogous to the excitation of a hanging pendulum. (This also applies to the optics examples, where the waves are externally imposed.) However, onset in modulated RBC corresponds to the inverted pendulum [35], which has no natural frequencies about its (unstable) equilibrium.

This work suggests several directions for future investigations. We are currently investigating the effect of breaking inversion symmetry on pattern formation near the bicritical point by quantitatively comparing experiment and simulations that include non-Boussinesq effects. We expect other complex-ordered patterns may arise either by two frequency driving, as suggested by recent results in Faraday experiments [20, 81, 21, 23, 22, 82], or by using the sensitive dependence of  $q_{2c}^S$  on  $\omega$  to vary the ratio  $q_{2c}^H/q_{2c}^S$  over the experimentally accessible range of  $1.7 \lesssim q_{2c}^H/q_{2c}^S \lesssim 5.5$ . Finally, it is hoped this work will motivate mathematical investigations of resonant tetrad interactions involving equivariant perturbation theory [87] with the aim of rigorously characterizing new routes to complex-ordered patterns in nonequilibrium systems.

The authors would like to thank Profs. F. Busse, L. Kramer and M. Silber for useful discussions. This work is supported by the NASA Office of Life and Microgravity Sciences Grant NAG3-2006.

# Bibliography

- [1] S. Carmi and J. I. Tustaniwskyj. “Stability of modulated finite-gap cylindrical Couette flow: linear theory.” *J. Fluid Mech.*, vol. 108, pp. 19–42, 1981.
- [2] J. P. Gollub and J. Langer. “Pattern formation in nonequilibrium physics.” *Rev. Mod. Phys.*, vol. 71, pp. S396–S403, 1999.
- [3] L. D. Landau and E. Lifshitz. *Fluid mechanics*. London, England: Pergamon Press, 1959.
- [4] D. Ruelle and F. Takens. “On the nature of turbulence.” *Commun. Math. Phys.*, vol. 20, pp. 167–192, 1971.
- [5] G. Ahlers. “Low-Temperature Studies of the Rayleigh-Bénard Instability and Turbulence.” *Phys. Rev. Lett.*, vol. 33, pp. 1185–1188, 1974.
- [6] J. B. McLaughlin and P. C. Martin. “Transition to Turbulence of a Statically Stressed Fluid.” *Phys. Rev. Lett.*, vol. 33, pp. 1189–1192, 1974.
- [7] M. Cross and P. Hohenberg. “Pattern-formation Outside of Equilibrium.” *Rev. Mod. Phys.*, vol. 65, pp. 851–1112, 1993.
- [8] H. Bénard. “Les Tourbillons cellulaires dans une nappe liquide.” *Rev. Gen. Sci. Pure Appl.*, vol. 11, pp. 1261–1271 and 1309–1328, 1900.

- [9] H. Bénard. “Les Tourbillons cellulaires dans une nappe liquide transportant de la chaleur par convection en régime permanent.” *Ann. Chim. Phys.*, vol. 23, pp. 62–144, 1901.
- [10] L. Rayleigh. “On convective currents in a horizontal layer of fluid when the higher temperature is on the under side.” *Phil. Mag.*, vol. 32, pp. 529–546, 1916.
- [11] J. R. A. Pearson. “On convection cells induced by surface tension.” *J. Fluid Mech.*, vol. 4, pp. 489–500, 1958.
- [12] G. Taylor. “Stability of a viscous liquid contained between rotating cylinders.” *Phil. Trans. Roy. Soc. A*, vol. 223, pp. 289–343, 1923.
- [13] G. Ahlers. “Experiments with pattern-forming systems.” *Physica (Amsterdam)*, vol. 51, pp. 421–443, 1991.
- [14] J. P. Gollub and H. L. Swinney. “Onset of Turbulence in a Rotating Fluid.” *Phys. Rev. Lett.*, vol. 35, pp. 927–930, 1975.
- [15] I. B. Cohen and A. Whitman, eds. *Isaac Newton – The Principia – Mathematical Principles of Natural Philosophy*. Berkeley, California: University of California Press, 1999.
- [16] M. Faraday. “On a peculiar class of Acoustical Figures; and on certain Forms assumed by groups of particles upon vibrating elastic Surfaces.” *Phil. Trans. Roy. Soc. A*, vol. 121, pp. 299–340, 1831.
- [17] L. M. Pismen and B. Y. Rubenstein. “Quasicrystalline and Dynamic Planforms in Nonlinear Optics.” *Chaos Solitons Fractals*, vol. 10, pp. 761–776, 1999.

- [18] B. Malomed, A. Nepomnyashchiĭ and M. Tribelskiĭ. “Two-dimensional quasiperiodic structures in nonequilibrium systems.” *Zh. Eksp. Teor. Fiz.*, vol. 96, pp. 684–700, 1989.
- [19] B. Christiansen, P. Alstrøm and M. T. Levinsen. “Ordered Capillary-Wave States: Quasicrystals, Hexagons, and Radial Waves.” *Phys. Rev. Lett.*, vol. 68, pp. 2157–2160, 1992.
- [20] W. Edwards and S. Fauve. “Parametrically excited quasicrystalline surface waves.” *Phys. Rev. E*, vol. 47, pp. R788–R791, 1993.
- [21] A. Kudrolli, B. Pier and J. Gollub. “Superlattice patterns in surface waves.” *Physica (Amsterdam)*, vol. 123D, pp. 99–111, 1998.
- [22] H. Arbell and J. Fineberg. “Spatial and Temporal Dynamics of Two Interacting Modes in Parametrically Driven Surface Waves.” *Phys. Rev. Lett.*, vol. 81, pp. 4384–4387, 1998.
- [23] H. Arbell and J. Fineberg. “Two-Mode Rhomboidal States in Driven Surface Waves.” *Phys. Rev. Lett.*, vol. 84, pp. 654–657, 2000.
- [24] H.-J. Pi, S. yeon Park, J. Lee and K. J. Lee. “Superlattice, Rhombus, Square, and Hexagonal Standing Waves in Magnetically Driven Ferrofluid Surface.” *Phys. Rev. Lett.*, vol. 84, pp. 5316–5319, 2000.
- [25] S. Residori, P. Ramazza, E. Pampaloni, S. Boccaletti and F. Arecchi. “Domain Coexistence in Two-Dimensional Optical Patterns.” *Phys. Rev. Lett.*, vol. 76, pp. 1063–1066, 1996.

- [26] E. Pampaloni, S. Residori, S. Soria and F. Arecchi. “Phase Locking in Nonlinear Optical Patterns.” *Phys. Rev. Lett.*, vol. 78, pp. 1042–1045, 1997.
- [27] R. Herrero, E. G. Westhoff, A. Aumann, T. Ackemann, Y. A. Logvin and W. Lange. “Twelfefold Quasiperiodic Patterns in a Nonlinear Optical System with Continuous Rotational Symmetry.” *Phys. Rev. Lett.*, vol. 82, pp. 4627–4630, 1999.
- [28] O. Brausch. *Rayleigh Bénard Konvektion f"ur verschiedene isotrope und anisotrope Systeme*. Ph.D. thesis, Physikalisches Institut der Universität Bayreuth, 2001.
- [29] Story as told by Russell Donnelly during a conversation at the American Physical Society - Fluids Division annual conference in Washington, D.C. - Nov. 2000.
- [30] H. Suhl. “Restoration of Stability in Ferromagnetic Resonance.” *Phys. Rev. Lett.*, vol. 6, pp. 174–176, 1961.
- [31] H. Suhl. “Effect of Periodic Adiabatic Time Variations on Interacting Systems.” *Phys. Rev.*, vol. 123, pp. 1262–1264, 1961.
- [32] R. J. Donnelly, F. Reif and H. Suhl. “Enhancement of Hydrodynamic Stability by Modulation.” *Phys. Rev. Lett.*, vol. 9, pp. 363–365, 1962.
- [33] R. J. Donnelly. “Experiments on the stability of viscous flow between rotating cylinders III. Enhancement of stability by modulation.” *Proc. R. Soc. Lon. Series A*, vol. 281, pp. 130–139, 1964.

- [34] G. Venezian. “Effect of modulation on the onset of thermal convection.” *J. Fluid Mech.*, vol. 35, pp. 243–254, 1969.
- [35] P. M. Gresho and R. L. Sani. “The effects of gravity modulation on a heated fluid layer.” *J. Fluid Mech.*, vol. 40, pp. 783–806, 1970.
- [36] M. N. Roppo, S. H. Davis and S. Rosenblat. “Bénard convection with time-preiodic heating.” *Phys. Fluids*, vol. 27, pp. 796–803, 1984.
- [37] P. Hohenberg and J. Swift. “Hexagons and rolls in periodically modulated Rayleigh-Bénard convection.” *Phys. Rev. A*, vol. 35, pp. 3855–3873, 1987.
- [38] G. Ahlers, P. Hohenberg and M. Lücke. “Thermal convection under external modulation of the driving force. II. Experiments.” *Phys. Rev. A*, vol. 32, pp. 3519–3534, 1985.
- [39] C. W. Meyer, D. S. Cannell and G. Ahlers. “Hexagonal and roll flow patterns in temporally modulated Rayleigh-Bénard convection.” *Phys. Rev. A*, vol. 45, pp. 8583–8604, 1992.
- [40] K. Thompson, K. Bajaj and G. Ahlers. “Travelling concentric-roll pattterns in Rayleigh-Bénard convection with modulated rotation.” *Bull. Am. Phys. Soc. DFD00:BK006*, 2000.
- [41] A. Smits, B. Auvity and M. Sinha. “Taylor-Couette flow with a shaped inner cylinder.” *Bull. Am. Phys. Soc. DFD00:BD.002*, 2000.
- [42] G. M. Homsy. “Global stability of time-dependent flows. Part 2. Modulated fluids layer.” *J. Fluid Mech.*, vol. 62, pp. 387–403, 1974.

- [43] S. H. Davis. “The Stability of Time-Periodic Flows.” *Ann. Rev. Fluid Mech.*, vol. 8, pp. 57–74, 1976.
- [44] T. J. Walsh and R. J. Donnelly. “Taylor-Couette Flow with Periodically Corotated and Counterrotated Cylinders.” *Phys. Rev. Lett.*, vol. 60, pp. 700–703, 1988.
- [45] X. Wu and J. B. Swift. “Onset of secondary flow in the modulated Taylor-Couette system.” *Phys. Rev. A*, vol. 40, pp. 7197–7201, 1989.
- [46] P. Hall. “The stability of unsteady cylinder flows.” *J. Fluid Mech.*, vol. 67, pp. 29–63, 1975.
- [47] S. Rosenblat and D. M. Herbert. “Low-frequency modulation of thermal instability.” *J. Fluid Mech.*, vol. 43, pp. 385–398, 1970.
- [48] R. G. Finucane and R. E. Kelly. “Onset of instability in a fluid layer heated sinusoidally from below.” *Int. J. Heat Mass Transfer*, vol. 19, pp. 71–85, 1976.
- [49] J. J. Niemela and R. J. Donnelly. “External Modulation of Rayleigh-Bénard Convection.” *Phys. Rev. Lett.*, vol. 59, pp. 2431–2434, 1987.
- [50] G. Ahlers, P. Hohenberg and M. Lücke. “Thermal convection under external modulation of the driving force. I. The Lorenz model.” *Phys. Rev. A*, vol. 32, pp. 3493–3518, 1985.
- [51] S. Biringen and L. J. Peltier. “Numerical simulation of a 3-D Bénard convection with gravitational modulation.” *Phys. Fluids A*, vol. 2, pp. 754–764, 1990.

- [52] R. Clever, G. Schubert and F. Busse. “Two-dimensional oscillatory convection in a gravitationally modulated fluid layer.” *J. Fluid Mech.*, vol. 253, pp. 663–680, 1993.
- [53] R. Clever, G. Schubert and F. Busse. “Three-dimensional oscillatory convection in a gravitationally modulated fluid layer.” *Phys. Fluids A*, vol. 5, pp. 2430–2437, 1993.
- [54] J. de Bruyn, E. Bodenschatz, S. Morris, S. Trainoff, Y. Hu, D. Cannell and G. Ahlers. “Apparatus for the study of Rayleigh-Bénard convection in gases.” *Review of Scientific Instruments*, vol. 67, pp. 2043–2067, 1996.
- [55] V. Croquette. “Convective pattern dynamics at low Prandtl number: Part I.” *Cont. Phys.*, vol. 30, pp. 113–133, 1989.
- [56] W. Pesch. “Complex spatiotemporal convection patterns.” *Chaos*, vol. 6, pp. 348–357, 1996.
- [57] S. Rasenat, G. Hartung, B. Winkler and I. Rehberg. “The shadowgraph method in convection experiments.” *Exps. Fluids*, vol. 7, pp. 412–420, 1989.
- [58] R. C. Weast. *CRC Handbook of Chemistry and Physics*. CRC Press, Inc., Boca Raton, Florida, 1985.
- [59] S. Chandrasekhar. *Hydrodynamic and Hydromagnetic Stability*. New York: Dover Publications, 1981, first ed.
- [60] R. Clever and F. Busse. “Transition to time-dependent convection.” *J. Fluid Mech.*, vol. 65, pp. 625–645, 1974.

- [61] Only minor modifications are required since the new oscillatory part of the buoyancy force (a linear term) is integrated explicitly in time by employing the approach used for quadratic nonlinearities described in [56].
- [62] E. Bodenschatz, J. R. de Bruyn, G. Ahlers and D. S. Cannell. “Transitions between Patterns in Thermal Convection.” *Phys. Rev. Lett.*, vol. 67, pp. 3078–3081, 1991.
- [63] S. Ciliberto, P. Couillet, J. Lega, E. Pampaloni and C. Perez-Garcia. “Defects in Roll-Hexagon Competition.” *Phys. Rev. Lett.*, vol. 65, pp. 2370–2373, 1990.
- [64] S. Ciliberto, E. Pampaloni and C. Pérez-Garcia. “Competition between Different Symmetries in Convective Patterns.” *Phys. Rev. Lett.*, vol. 61, pp. 1198–1201, 1988.
- [65] S. W. Morris, E. Bodenschatz, D. S. Cannell and G. Ahlers. “The spatio-temporal structure of spiral-defect chaos.” *Physica (Amsterdam)*, vol. 97, pp. 164–179, 1996.
- [66] J. Rogers, M. Schatz, J. Bougie and J. Swift. “Rayleigh-Bénard Convection in a Vertically Oscillated Fluid Layer.” *Phys. Rev. Lett.*, vol. 84, pp. 87–90, 2000.
- [67] C. Bowman and A. Newell. “Natural patterns and wavelets.” *Rev. Mod. Phys.*, vol. 70, pp. 289–301, 1998.
- [68] J. Rogers, M. Schatz, O. Brausch and W. Pesch. “Superlattice patterns in vertically oscillated Rayleigh-Bénard convection.” *Phys. Rev. Lett.*, vol. 85, pp. 4281–4284, 2000.

- [69] S. W. Morris, E. Bodenschatz, D. S. Cannell and G. Ahlers. “Spiral defect chaos in large aspect ratio Rayleigh-Bénard convection.” *Phys. Rev. Lett.*, vol. 71, pp. 2026–2029, 1993.
- [70] B. B. Plapp, D. A. Egolf and E. Bodenschatz. “Dynamics and Selection of Giant Spirals in Rayleigh-Bénard Convection.” *Phys. Rev. Lett.*, vol. 81, pp. 5334–5337, 1998.
- [71] M. Cross. “Ingredients of a theory of convective textures close to onset.” *Phys. Rev. A*, vol. 25, pp. 1065–1076, 1982.
- [72] F. Busse. “The stability of finite amplitude cellular convection and its relation to an extremum principle.” *J. Fluid Mech.*, vol. 30, pp. 625–649, 1967.
- [73] P. Couillet, T. Frisch and G. Sonnino. “Dispersion-induced patterns.” *Phys. Rev. E*, vol. 49, pp. 2087–2090, 1994.
- [74] M. Boucif, J. Wesfreid and E. Guyon. “Experimental study of wavelength selection in the elastic buckling instability of thin plates.” *Euro. J. Mech. A, Solids.*, vol. 10, pp. 641–661, 1991.
- [75] C. Sz waj, S. Bielawski, D. Derozier and T. Erneux. “Faraday instability in a multimode laser.” *Phys. Rev. Lett.*, vol. 80, pp. 3968–3971, 1998.
- [76] W. van Saarloos and J. Weeks. “Faraday instability of crystallization waves at the  $^4\text{He}$  solid-liquid.” *Phys. Rev. Lett.*, vol. 74, pp. 290–293, 1995.
- [77] G. Z. Gersuni and D. V. Lyubimov. *Thermal vibrational convection*. John Wiley & Sons, Chichester; New York, 1998.

- [78] U. E. Volmar and H. W. Müller. “Quasiperiodic patterns in Rayleigh-Bénard convection under gravity modulation.” *Phys. Rev. E*, vol. 56, pp. 5423–5430, 1997.
- [79] B. A. Malomed, A. A. Nepomnyashchy and M. I. Tribelsky. “Domain boundaries in convection patterns.” *Phys. Rev. A*, vol. 42, pp. 7244–7263, 1990.
- [80] Y. Hu, R. Ecke and G. Ahlers. “Convection under rotation for Prandtl numbers near 1: linear stability, wave-number selection, and pattern dynamics.” *Phys. Rev. E*, vol. 55, pp. 6928–6949, 1997.
- [81] W. Edwards and S. Fauve. “Patterns and quasi-patterns in the Faraday experiment.” *J. Fluid Mech.*, vol. 278, pp. 123–148, 1994.
- [82] C. Wagner, H. Müller and K. Knorr. “Faraday Waves on a Viscoelastic Liquid.” *Phys. Rev. Lett.*, vol. 83, pp. 308–311, 1999.
- [83] J. Geddes, R. Indik, J. Moloney and W. Firth. “Hexagons and squares in a passive nonlinear optical system.” *Phys. Rev. A*, vol. 50, pp. 3471–3485, 1994.
- [84] M. Silber and A. C. Skeldon. “Parametrically excited surface waves: Two-frequency. normal form symmetries, and pattern selection.” *Phys. Rev. E*, vol. 59, pp. 5446–5456, 1999.
- [85] E. Bodenschatz, W. Pesch and G. Ahlers. “Recent developments in Rayleigh-Bénard convection.” *Annu. Rev. Fluid Mech.*, vol. 32, pp. 709–778, 2000.

- [86] W. Zhang and J. V. nals. “Pattern formation in weakly damped parametric surface waves driven by two frequency components.” *J. Fluid Mech.*, vol. 341, pp. 225–244, 1997.
- [87] S. L. Judd and M. Silber. “Simple and superlattice Turing patterns in reaction-diffusion systems: bifurcation, bistability, and parameter collapse.” *Physica (Amsterdam)*, vol. 136D, pp. 45–65, 2000.

# Vita

Jeffrey Lee Rogers was born in Chicago Illinois on October 14, 1966. In 1969 his parents, Jack Lewis Rogers and Sharon Yvette Furlong, moved to South Florida where Jeffrey was raised. Jeffrey graduated from Boca Raton High School in 1985 and entered Florida Atlantic University in 1989. He received a B.S. degree in Physics with an emphasis in Dynamical Systems in May 1992. Continuing at Florida Atlantic University on a Motorola Computational Fellowship he focused on Applied Mathematics and Computational Science, receiving a M.S. degree in May of 1994. In August of 1994 he began graduate studies in the Physics Department at Emory University in Atlanta, Georgia, earning a M.S. degree in Physics for research on Complex Systems in May of 1996. In the Fall of 1996 he enrolled in the School of Physics at Georgia Institute of Technology and received the Robert G. Schakleford Fellowship. While at the School of Physics Jeffrey continued his studies of dynamical systems through experimental work on pattern formation in fluid systems as well as numerical and theoretical research on the behavior of large arrays of coupled oscillators. On October 21, 2000 Jeffrey and Jessica Ileen Silver were married on Santa Rosa Beach in Florida. Jeffrey received a Ph.D. in Physics from Georgia Institute of Technology in May of 2001.

This dissertation was prepared in  $\text{\LaTeX}$  by the author.